UNIVERSITY OF CALIFORNIA,
IRVINE

Electrostatic Focusing of Electrospray Beams

DISSERTATION

submitted in partial satisfaction of the requirements
for the degree of

DOCTOR OF PHILOSOPHY

in Mechanical and Aerospace Engineering

by

Elham Vakil Asadollahei

Dissertation Committee:
Professor Manuel Gamero-Castaño, Chair
Professor Lorenzo Valdevit
Professor Timothy J. Rupert

2017

DEDICATION

To MY FAMILY

TABLE OF CONTENTS

LIST OF FIGURES

LIST OF TABLES

ACKNOWLEDGMENTS

I would like to express my sincere gratitude to my research supervisor, Professor Manuel Gamero-Castao. His support has been undeniably encouraging throughout my PhD and his close assistance in the lab have provided me a rare opportunity to learn many experimental skills. I am also grateful to my thesis committee, Professor Lorenzo Valdevit and Professor Timothy Rupert for their time and helpful inputs in my proposal defense and feedback on my thesis.

I am grateful to my parent and siblings for their love and unfailing moral and emotional support in my life. Many long-time chats and phone calls have been their support channel during my graduate study. They turned many disappointments to hope and motivation, and many sad moments to happy talks. Many thanks to Darshan Chinvar, for his unconditional love and support, and unlimited encouragement during the final stages of my PhD.

My gratitude also goes out to UCI staff at INRF and physical science machine shop for their help and support during this research. I also want to express my appreciation to DARPA which partially funded my work through a Young Faculty Award Grant N66001-10-1-4039.

And finally, last but by no means least, I must thank my friends and colleagues at UC Irvine, specially, Dr. Fernan Saiz, Dr. Rafael Borrajo-Pelaez, and Dr. Enric Grustan for their friendship and support. I am thankful to all other friends who have brought happiness to my every day and encouragement of tomorrows.

CURRICULUM VITAE

Elham Vakil Asadollahei

EDUCATION

Doctor of Philosophy in Mechanical and Aerospace Engineering
University of California, Irvine, 2017

Master of Science in Mechanical and Aerospace Engineering
University of California Irvine, Irvine, 2012

Master of Science in Mechanical Engineering
Amirkabir University of Technology, Tehran, Iran, 2004

Bachelor of Science in Mechanical Engineering
Sharif university of Technology, Tehran, Iran, 2001

FIELD OF STUDY

Electrospray Beam Optics

PUBLICATIONS

Elham Vakil Asadollahei, Manuel Gamero-Castaño, "Design of an Electrostatic Lens for Focused Electrospray". (under preparation)

Elham Vakil Asadollahei, Manuel Gamero-Castaño, " Semiconductor Sputtering by Focused Electrospray Nanodroplet Bombardment". (under preparation)

Elham Vakil Asadollahei, Manuel Gamero-Castaño, "Plasma Activated Bonding for an Enhanced Alignment Electrostatic Lens", IMAPS2016, October 2016.

Elham Vakil Asadollahei, "A Miniature Folded MEMS-IMU Development toward Vestibular Prosthesis" , ProQuest Dissetations and Theses, December 2011.

Vakil Asadollahei E., Kabganian M., "A New Stability Criterion for Attitude Dynamics of Flexible Spacecrafts", The 14th International Annual Conference of Mechanical Engineering, 16-18 May, 2006, Isfahan University of Technology, Isfahan, Iran.

Kabganian M., Vakil Asadollahei E.," Robustness Analysis of Open-Loop, Closed-Loop Control of Flexible Spacecrafts", Second International Aerospace Conference, Feb 2004, Isfahan, Iran.

ABSTRACT OF THE DISSERTATION

Electrostatic Focusing of Electrospray Beams

By

Elham Vakil Asadollahei

Doctor of Philosophy in Mechanical and Aerospace Engineering

University of California, Irvine, 2017

Professor Manuel Gamero-Castaño, Chair

The Electrospray ionization which is also known as electro-hydrodynamic ionization produces a beam of charged nanodroplets. These beams of nanodroplets can be used in material deposition, sputtering, and milling processes, all of which are currently done by beams of atomic and cluster ions. In electrospray atomization, a uniform beam of submicron-sized charged droplets is sprayed in vacuum in a strong electric field. The charged droplets are accelerated by the electric field induced by the electrodes. The space charge of the beam causes the droplets to repel each other and the beam to open up. In this dissertation, the development of an electrostatic column for electrospray beam focusing is presented. Coaxial electrodes were designed to extract and focus the beam. The beam is skimmed to agree with the paraxial assumption used in the projectile tracing. Fundamentals of the charged particle tracing under an electric field is discussed in detail and numerical simulations provide the projectile trajectory and image location where the beam is focused and energy density is maximized. These focused beams are used to sputter a semiconductor target. The performance of the focusing apparatus can be characterized based on the size and features of the impacted area. The error sources in lens system result in an increased image size appearing in the form of slightly sputtered area. These aberration figures are analyzed

for different field strength to determine the size of imperfections in the apparatus and to be possibly corrected in next stages of development. With the exception of spherical and chromatic aberrations, other sources of errors can be eliminated or at least minimized if the misalignments between elements including electrospray source and electrodes are minimized. An innovative process is presented for fabricating the focusing lens using microfabrication techniques. This approach guaranties high precision and minimum misalignment between elements. Plasma activated bonding is used to permanently attach the silicon electrodes and glass standoffs. In addition to precision fabrication of apertures, the advantage of this approach over conventional machining is eliminating post fabrication assembly. Despite higher cost and difficulty of process, the microfabricated lens assembly successfully provides the voltage and accuracy requirements for a high resolution focusing lens.

Chapter 1

Introduction

1.1 Overview

Atomic, molecular, and cluster ions are essential part of physical processes in the semiconductor industry. The physical processes including etching, thin film deposition, doping, and sputtering rely on the energetic bombardment of the surface of the target by a beam of ions or the ions existing in a plasma environment. Surface analysis through imaging is another application of electron and ion beam both in Scanning Electron Microscopy (SEM) and Focused Ion Beam (FIB). [1] FIB is an advanced tool in micro/nano fabrication, surface modification and surface analysis. It is based on energetic impact of accelerated ions emitted from a liquid metal ion source (LMIS) or gas cluster ion beam(GCIB). Despite the similarities in the SEM and FIB columns, the heavy ions (10^6 times more than electrons) in FIB has different effect on the target surface. During impact, the momentum of the atomic or gas cluster ion beam is transferred to the surface atoms in the impact area. Even though the ions penetrate up to 200 times less in the target surface than electrons, this energy exchange is enough to break

the atomic bonds and cause atomic ionization on the surface. These atoms are ejected out of the surface and cause a high yield physical sputtering. During the deposition process, the accelerated ions collide with the atoms of depositing materials above the sample and increase their energy to be able to produce atomic bonds with the substrate after impact. Imaging and secondary ion mass spectrometry is possible by collecting the secondary electrons or secondary ions ejected from the surface. Despite possible surface damage, the FIB secondary electron imaging technique is used for high contrast grain morphology imaging. Small beam currents, below 100pA, may be used in FIB imaging to minimize damage during imaging. In addition to these processes, maskless etching is another enabling application of FIB in nanofabrication technology. Precision cuts and cross sections are etched in samples of any material without lithography and additional sample preparation. In case of monomer ion beam the etching rate is controlled by the accelerating field since the liquid metal ion source in a FIB is normally Gallium. However, in applications such as sample preparation for transmission electron microscopy (TEM) [2] where the ion implantation and surface damage can change the image quality of a thin layer of material (about 100 nm-thick), an Argon source with lower current is a better alternative. The sputtering yield and destructive effect of the ion beam on the surface have been improved in the gas cluster ion beam(GCIB) bombardment where the larger projectile provides a higher energy density into the impact area. [3] Each cluster contains up to 20000 atoms. Since the energy of each cluster is divided among up to few thousand atoms or molecules, the penetration depth and thus the destructive effect on the surface decrease. In addition to a very low charge to mass ratio, GCIB has other advantages including, higher sputtering yield due to multiple collision in different incident angles, and surface smoothing in atomic level. [4] Shallow implantation of low energy individual atoms in GCIB also showed the enhancement of surface doping over monomer ion beam. [5–7] However the quality of images may not increase in GCIB because of higher sputtering rate which limits the resolution in addition to optical limits, it is more effective

in imaging very small features where molecular rearrangement and re-deposition of ions on the surface might limit the resolution. [8] All of the improvements associated with cluster ion beam are bound to the limitation on the size and molecular composition of the cluster. Size of cluster ions does not exceed more than a few nanometer. On the other hand a larger cluster with large number of the atoms demands a higher accelerating voltage to provide the minimum 10 eV energy per individual atom to create any of the discussed effects. The energy exchange during bombardment heats up the target and facilitates the chemical reaction between the cluster ion atoms and substrate, so an inert gas is preferably used. These restrictions have handicapped the research in projectile size before the Electrospray sputtering was introduced. [9] The Electrospray ionization , also known as electro-hydrodynamic ionization, produces a beam of charged nanodroplets. A controlled flow of liquid is fed to a nozzle, turns into a jet of fluid and breaks into submicron-sized droplets. The breaking point acts as a point source for the beam of nanodroplets. This, combined with the high molecualr flux of sprayed nanodroplets with low q/m and narrow distribution of droplet size, makes the electrospray source an ideal candidate for ion beam in physical sputtering and milling processes. The electrospray can be produced with a variety of liquids, which offers the freedom of choosing chemical composition and molecular mass, as opposed to ion beams with limited number of gas sources. An electrospray setup requires a reasonable voltage less than 20 kV to produce the droplet projectiles capable of sputtering with similar or higher sputtering rate than an ion beam. In addition, the larger electrospray nanodroplet does not penetrate in the substrate during electrospray bombardment, so that surface damage is minimized. This can be beneficial for both sputtering and maskless etching. The goal of this thesis is to investigate the resolution improvement resulted by focusing the electrospray beam. After the introduction chapter, the theory of particle tracing in an electrostatic field is presented in chapter II. A numerical study shows the trajectory of the beamlet from a point source passing through the electrostatic lens and deflectors field to the Gaussian image

plane. The experimental approaches are discussed in Chapter III. Two methods were practiced for fabricating and assembling the experiment apparatus; a microfabrication approach, suggested for minimizing misalignments, and a conventional machining approach. Finally, in chapter IV an experimental study of the bombardment of a silicon substrate by focused electrospray beams is used to demonstrate the performance of our electrostatic lens design.

1.2 Electrospray Theory and Applications

Electrospray atomization is a process that generates submicron-sized charged droplets from an electrolyte solution. Once a simple method for painting cars, electrospray is now used in a wide range of applications such as microthrusters [10–14], electrospray ionization mass spectrometry(ESI-MS) [15], sputtering [16, 17], deposition and so on. A few decades after Dole proposed the electrospray method for mass spectrometry, Fenn successfully used this ionization technique to produce the ion droplets that include only one protein macromolecule with the goal of measuring its molecular mass. [15] Now it is also used to collect other structural information of the biomolecules. [18] A combination of pressure difference and capillary force extracts the ionic solution from the reservoir and guides the flow through the few-hundred-micrometer capillary tube (needle), while a voltage difference between the tube (emitter electrode) and a second electrode (extractor) provides the large electric field (in the order of 10^6 V/m) on the capillary tip needed to setup the electrospray. [19] This field is estimated based on the applied potential on the capillary (V_c), the capillary radius (r_c), and the distance of the extractor from capillary tip.

$$E_c = \frac{2\,V_c}{r_c\; ln(\frac{4d}{r_c})} \tag{1.1}$$

This electric field penetrates under the liquid meniscus at the capillary tip and polarizes the liquid. The positive ions add up under the meniscus while the negative ions move away from the surface. The interaction force between the electric field and positive ions, as well as the surface tension of the liquid at the tip of needle causes the tip to elongate and forms a stable conical shape known as Taylor cone. [20–22] Despite the dynamic nature of the inner region of the cone, the outer region is considered hydrostatic which appears as an stationary feature. The electrostatic repulsion of charges on the cone surface is balanced with the surface tension which minimizes the surface area. The static equilibrium between these two pressures dictates the condition where the electrostatic force is orthogonal to the surface described by Equation (1.2) in spherical coordinates and the cone angle of $\theta = 49.3°$. [23, 24]

$$\begin{aligned} \varphi(r,\theta) &= \varphi_0\, r^{0.5}\, P_{1/2}\,(Cos\theta) \\ {\varphi_0}^{-2} &= 0.552\,(\tfrac{\varepsilon_0}{\gamma})^{1/2} \end{aligned} \tag{1.2}$$

where $P_{(1/2)}$ is a Legendre function of order 1/2, and ϵ_0 and γ are the permittivity of the medium around the cone, and surface tension, respectively. This angle decreases with increasing the spray flow.

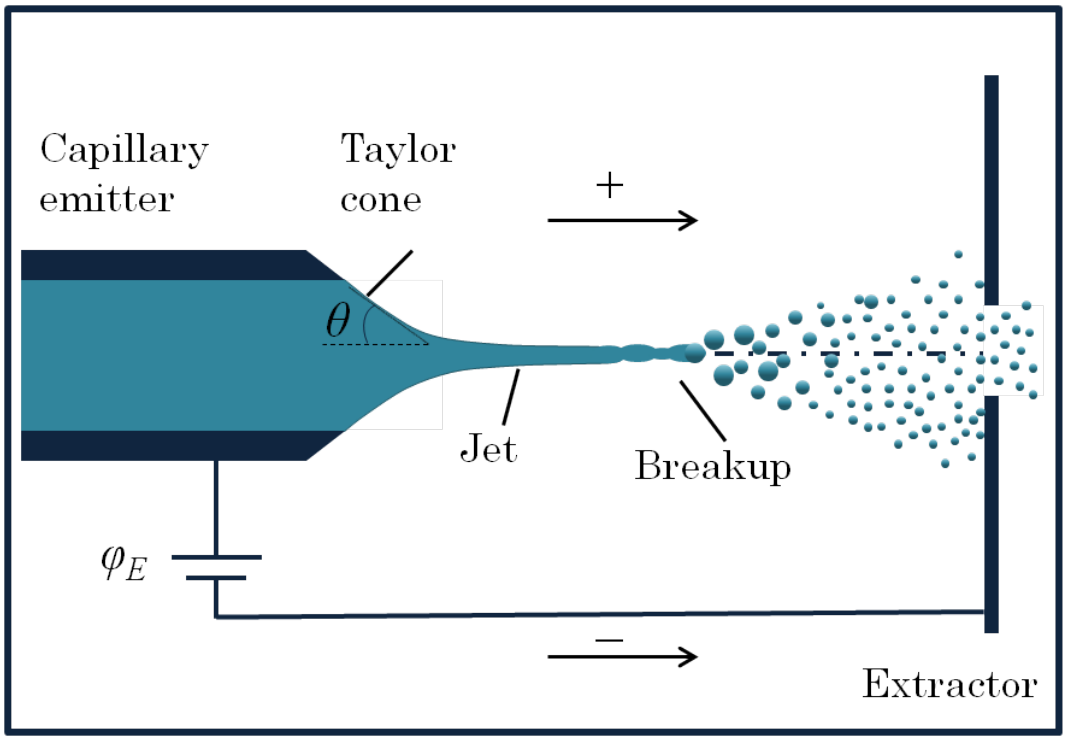

Figure 1.1: Electrospray atomization schematic.

A fine jet continuously emerges from the cone's apex. This jet eventually becomes unstable breaking up into charged droplets. In the transition between cone and jet in break-up region, a significant part of flow energy dissipates, due to the ohmic and viscous dissipation and surface energy generation. [25] The time of flight and retarding potential techniques are used to characterize these sparays and support their modelling. [26] Under atmospheric pressure, the droplet continues to shrink with solvent evaporation till the ionization starts. Two models have been proposed to describe the electrospray ionization process from these shrinking droplets [27]; The **Ion Evaporation Model** suggests solvated ions are ejected out of the droplet when the droplet diameter reaches around 20 nm and surface field strength is high enough to compensate for the solvation energy of the ions in solution. The **Charge Residue Model** describes electrospray ionization based on the emission of the smaller droplets from the local Taylor cone on the droplet. When the droplet shrinks enough that

the charge density reaches the Rayleigh limit at the highest curvature surfaces, the droplet elongation phenomenon under charge field forms another Taylor cone forms on the droplet surface. As a result a highly charged droplet is emitted from the Taylor cone apex. Each droplet eventually produces multiple smaller charges droplets after de-clustering. Rayleigh limit determines the relation between the critical radius of the drop R and the drops charge q as following: [28, 29]

$$q = 8\pi \left(\epsilon_0 \, \gamma \, r^3\right)^{1/2} \tag{1.3}$$

where ϵ_0 and γ are the permittivity of vacuum and the liquid's surface tension respectively. Fenn showed this process can continue until drops contain only one molecule of the protein with on or multiple charges in gas phase. The Rayleigh limit defines the maximum charge for and isolated, electrically conductive drop in vacuum; however, in the presence of the space charges, the drop may break at a lower charge of $70 - 80\%$ of the Rayleigh limit. [30] Gamero-Castaño estimated the charge level of 68% of Rayleigh limit for EMI-Im. [31]
The low charge to mass ratio is the fundamental characteristics of the electrospray charged droplet which places the high molecular weight biomolecules in the detectable spectrum in mass spectrometry. In addition to low charge to mass ratio, the high conductivity of the electrospray give an advantage over other ionization methods such as ion beam. Each parent drop contains several neutral molecules and carries multiple elementary charges which implies almost infinite conductivity of the flow. After evaporation and de-clustering, each drop may have one or more than one elementary charges and the spray remains highly conductive.

1.3 Background

Energetic bombardment of materials with a focused ion beam is used in advanced nano-scale microfabrication techniques such as sputtering, thin film deposition, doping, and etching. [3, 5, 32] The cluster ion beam processes consist in bombardment of the surface with a molecular or atomic cluster ion beam. During the collision the energy exchange between the cluster projectile and the surface causes the ejection of atoms from the surface (sputtering) [1, 33, 34] or causes topographic changes on the surface (e.g. surface amorphization). [35,36] Cluster size is an important property that affects the result of this interaction. Larger clusters are used in surface smoothing process and smaller clusters are used in high yield sputtering process. [37] When high energy clusters are used for high rate milling, the low energy beam is a choice for surface smoothing and removing organic contamination. In case of gas cluster ion beam (GCIB), each cluster consists of up to 100,000 atoms, with sizes reaching up to a few nanometers. [34] Along with projectile size [37], the projectile energy [38] and incident angle [39] are other important parameters affecting sputtering yields. Research on larger gas cluster ion beams shows that these ion clusters such as Ar_{2000} not only increases the size of the crater after each incident and thus the sputtering rate, it also helps to eliminate the surface roughness because of decreased penetration depth due to lower energy of individual atoms. Moreover, noble gas clusters such as Ar are commonly used to minimize the chemical interactions with substrate which limits the chemical composition and molecular mass of projectiles. The charge to mass ratio (specific charge) of the larger clusters remains low because of limitation of ion charges on each cluster and requires higher potential to focus and accelerate the cluster beam. In addition to this, the lack of a projectile source between nanometer-sized cluster [37] and micron-sized particles [40] have made it impossible to study experimentally the size dependence of sputtering yield. Electrospray atomization has introduced a suitable source for sub-micron-sized projectiles. After early works on the

electrospray mass spectrometery, an extensive body of work by Fernandez de la Mora and Gamero-Castaño describe the physics of the electrospray droplets in cone-jet mode. [41–45] The unique properties of the electrospray charged droplets such as narrow distribution of size and uniform energy level of submicron-sized droplets, high molecular flux of the beam, and access to ionic liquids with different molecular mass extended the application of electrospray droplets for activities where an energetic impact of hypervelocity charged particles is needed. Using Electrospray in hypervelocity impact applications is more efficient than large gas cluster ion beam because of low accelerating voltage; accelerating voltages below 20 kV are able to provide impact energies in the order of MeV to the multiply charged nanodroplets. The use of electrospray clusters of $0.1 - 0.5$ μm was reported for surface cleaning [46] and secondary ion mass spectrometry. [47] Electrospray droplet impact (EDI) was also suggested for molecular level etching of native SiO_2 and InP. Sakei, et al. experimentally showed the energized electrospray beam up to 106 under accelerating voltage 10 kV is capable of molecular etching of thin layers of SiO_2 and InP, and physical sputtering and surface damage minimized. [48, 49] Due to higher current in vacuum the EDI technique is more effective in SIMS, recently shown by Takaishi, et al. [50] on several samples including thermometer molecule, peptide, polystyrene, $Alq3$, NPD, C_{60}, indium, and SiO_2. Mori, et al. also used the electrospray droplet impact (EDI) for surface analysis of a hard material. [51] Sputtering is another application of the electropray projectile which is also of interest in this thesis. Gamero and Mahadevan [31] investigated the physical sputtering of Si, SiC and B_4C by beamlet of nanodroplets sprayed from ionic liquid 1-ethyl-3- methylimidazolium bis (trifluoromethylsulfonyl)imide (EMI-Im) at normal incidents. The maximum sputtering yields reported 2.32, 1.48, and 2.29 atoms per molecule for Si, SiC, and B_4C respectively, these are much higher than sputtering rate of same material with Ar. The accelerating voltage of 15.1, 18,and 19.1 kV were used respectively to provide 253 nA current and carve 2 μm of material. At lower voltage 7 kV, the surface was reported to have no significant sput-

tering. Previously they had reported irradiating the single crystalline Si by an electrospray beamlet with an average molecular energy of 20.1 eV and 26.3 eV for 15 min resulted a sputtered crater of 3 μm and 3.5 μm deep and sputtering rate of 127 nm/min. [9] A molecular study on the sputtering of Si concluded that both collision cascade and thermal sputtering describe the sputtering physics during electrospray bombardment. [52] Other single-crystal semiconductors such as $InAs, InP, Ge, GaAs, GaSb$, and GaN have also been sputtered under EMI-Im electrospray bombardment. [16] A beam with higher molecular energy up to 105 eV was used and showed a sputtering yield in the range between 1.9 for a hard material such as SiC and 4.5 for Ge. A maximum sputtering rate of 2381 nm/min for $GaSb$ was reported. A comparison between the sputtering rate of Si with ionic liquids with different molecular mass (between 45 and 773.3 amu) shows that at the same impact velocity, the electrospray droplets with larger molecular mass lead to larger the roughness and sputtering rate. [17] A complementing molecular dynamics study and electrospray hypervelocity sputtering experiment for two ionic liquids EAN and EMI-Im at 17 km/s on substrates material of Si, SiC, Ge and $GaAs$ suggests the direct relation between increase in sputtering yield and molecular mass of projectile. [53] During the impact of electrospray beam of nanodroplets on crystalline material a thin layer of material is amorphized. This is due to melting the area near the impact and then ultra fact cooling. [54] The thickness of amorphized layer under the surface is comparable to the size of projectile because of large dissipation energy during nanodroplets impacts. An electron backscattered imaging is useful for experimentally mapping the amorphized area under the bombardment. Some single-crystal materials such as SiC need a higher impact velocity to form an amorphous layer. Although less prominent, another important parameter is the size of the drops. The threshold of droplets velocity that an amorphous layer begins to develop on Si surface was calculated by a molecular dynamic model at 3 km/s, the thickness of amorphous layer continues to increase with increasing the velocity of impacting drops until reaching an upper threshold of velocity above which the

thickness of amorphous layer does not increase. [55] To the extent of above sputtering and etching experiments, electrospray atomization offers macroclusters capable of carving and deposition on all type of substrates within a reasonable range of accelerating voltage. In addition to fundamental studies, electrospray beams should be focused to provide an acceptable resolution for higher rate etching and sputtering. A typical FIB instrument consist of beam forming optics such as focusing lenses, magnetic filters and deflectors after ionization and accelerating the beam. The technology of focused ion beam of a liquid metal ion source began in 1974 when Seliger and Fleming [56] published their FIB design for microfabrication purpose, specifically for ion implantation. With object aperture of 150 μm, the beam spot reduced to 3.5 μm. This column consisted of a symmetric enizel lens with 12 ft focusing arm, a double-deflector system and a target holder. Other parameters of focusing lens were as follows: lens diameter $D = 1.35\ in$, focal distance $f = 1.95D$ and spherical aberration coefficient $C_s = 35f$. Later Seliger and collaborators at HRL presented a scanning ion probe system with the beam spot size of 100 nm and current density of 1.5 A/cm using liquid Ga source. [57] Almost a decade after original proposal of focused ion beam apparatus, Orloff suggested a Köhler illumination design for FIB to go around the 0.2 $mrad$ scatter in 100 keV beam trajectory and achieve 10 nm beam diameter and 2 nm edge sharpness at the spot. The column consist of two condenser electrostatic lenses, two octupoles deflector to bring the beam to the center of $E \times B$ separator, two objective electrostatic lenses and two scanning octupoles. [58,59] A chronicle advancement of the focused ion beam and its applications such as ion implantation and surface doping, maskless etching and lithography and deposition, 3D nano structure formation and repair are discussed in review papers. [1, 60, 61] Since the technology of the gas clusters formation and ionization in 1988, the focused ion beam apparatus can use sources of different gas material than Ga for low energy bombardment of the target and applications such as surface smoothing. [62] Currently, the advanced FIB columns are more or less similar to the original design and some research is focused on micro FIB

column for low cost or improved resolution using microfabrication approaches. [63,64] Additionally, the aberration correction and modified design of the electrostatic lens have been the subject of further investigations in order to achieve the resolution requirements. [65–67] The beam spot size and brightness on the target are affected by aberration sources, among which spherical aberration, chromatic aberration and astigmatism have been discussed extensively in charged particle optics literature. [68–74] This dislocation of the beam spot and/or blurriness (both examples of geometrical aberrations) is due to error in locating the target as a result of ignoring higher order terms in the electric field in ion beam trajectory calculations. Although very well known, some of these aberration sources are inevitable. Spherical aberration is a result of stronger field affecting on the ions emitting at higher angle, it cannot be eliminated, but it can be minimized by higher accelerating voltage that does not allow the ion drifts much when traveling across the lens or it is compensated with other elements which dictate the spherical aberration coefficients with opposite sign. Astigmatism due to alignment errors depends highly on the manufacturing precision. With a precision fabrication, it is more likely to minimize this source of error and have an image close to that of paraxial trajectories. The chromatic aberration coefficient also can be accounted for in locating the target based on the characterized energy distribution of the beam.

Chapter 2

Charged Particle Dynamics

Charged particle dynamics studies the motion of charged particles (e.g. electrons, ions or charged droplets) in an electric or magnetic field. The deflection of the charged particles' trajectory due to interaction forces between the beam and the electric/magnetic field is similar to the refraction of light when entering different mediums. This physical phenomenon is used effectively in all optics column for focusing the diverging beam at the image plane, where a minimum beam diameter and highest charge density is desired for higher resolution. The resolution of the focusing systems is affected by the error sources that lead to different type of aberrations. In the case of high density beam the space charge changes the electrostatic field defined by the lens, deflectors, and other electrodes.

The refractive indexes in particle optics are defined by the potential of two adjacent regions. The particle's momentum changes along the direction perpendicular to the equipotential lines in the field, while the tangential momentum remains constant. This explains the particle trajectory bending when it travels through the electric field.

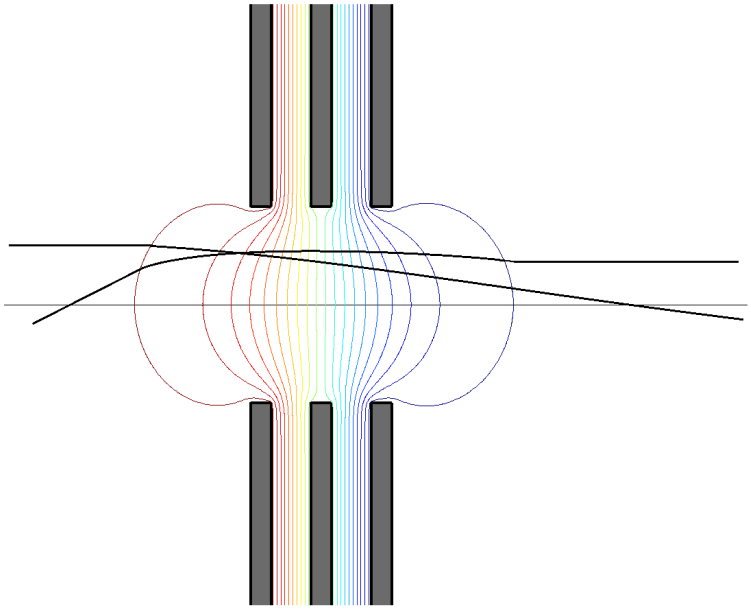

Figure 2.1: Trajectory deflection in electrostatic lens.

Conservation of total energy in transition from V_1 to V_2 and momentum component along the equipotential boundary lead to the relation between beam deflection and voltage $\frac{\sin\alpha_1}{\sin\alpha_2} = \sqrt{\frac{V_2}{V_1}}$ similar to Snell's law. Two focal points are defined on the object side and image side of the lens at the intersection of asymptotic trajectories of paraxial rays with the axis. The concepts of magnification and Gaussian image is defined similarly in optic lenses. A general ray $r(z)$ emitting from an axial point source at $-S$ is deflected and crosses the axis at image point I. The location of the Gaussian image is calculated as a function of linear characteristics of the lens.

The image location is determined by a superposition of two trajectories; two linearly independent rays $r_1(z)$ and $r_2(z)$ form the general ray $r(z)$ by $r(z) = \alpha r_1(z) + \beta r_2(z)$ (see Figure 2.2).

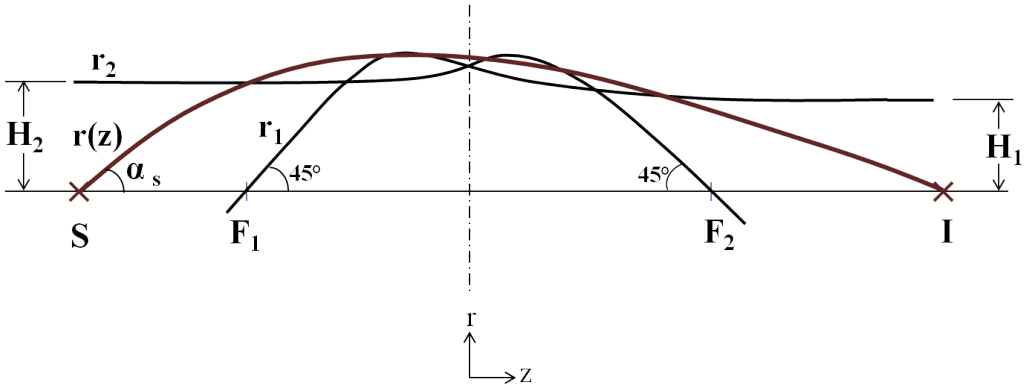

Figure 2.2: Two linearly independent path r_1 and r_2 define any general trajectory and determine the image location.

This decomposition is helpful in locating the Gaussian image. On the object side the general ray, emitted from S, is written in the linear form $r = \tan\alpha_s(Z_S)$. The coefficients α and β are derived from comparing this equation with the above form for general ray $r(z) = \alpha(Z - F_1) + \beta r_2(z)$. Here r_1 is defined by focal length $r_1 = \tan 45°(Z - F_1)$, F_1 is negative. On the other hand, at the image side the general ray forming the image is $r(z) = \alpha\ H_1 + \beta(-\tan 45°(I - F_2))$. The image location is defined by setting $r = 0$ in this equation and rearranging Equation (2.1) as follows:

$$I = F_2 + \frac{H_1 H_2}{F_1 - S} \tag{2.1}$$

2.1 Beam Focusing System

The motion of an isolated charged particle in the electric field induced by electrodes is studied here. For the sake of trajectory study every particle is considered a classical point projectile under Lorentz force. Note that the magnetic portion of the Lorentz force will be excluded

here, because the magnetic force is negligible for the heavy electrospray droplets which have much lower velocities than electrons or ions. In general, the electrostatic field can be static or time dependent. In our experiment setup we let the electric field stabilizes and will consider electrostatic field in particle tracing equations. The electrostatic field is defined by Gauss's law:

$$\nabla E = \rho/\varepsilon_0 \tag{2.2}$$

where ρ and ε_0 are the charge density and the vacuum permittivity. The effect of the space charges are neglected at this point and in this research. It can be considered as a source of aberration in focusing systems.

In this chapter two main elements of focusing and deflecting the beam, electrostatic lens and octupoles, will be discussed. The governing equations of the particle trajecory in axisymmetric electrostatic field is derived and used in numerical modeling.

2.2 Electrostatic Lens

An axisymmetric electrostatic field induced by a three-electrode lens deflects the travelig particles toward the axis line. The spherical field in the Einzel lens deflects the spray beam traveling through the lens; once voltage is applied on the lens electrodes, the diverging electrospray beam from a point source on the axis is focused on an image point. Laplaces equation in cylindrical coordinates for an axisymmetric potential field is: [75]

$$\frac{\partial^2 V}{\partial z^2} + \frac{1}{r}\frac{\partial}{\partial r}(r\frac{\partial V}{\partial r}) = 0 \tag{2.3}$$

Where $V(r, z)$ is the potential. Analytical solution of Laplace equation for a simple case of two electrodes is based on a linear change in axial voltage between two values of potential on electrodes. A series of Bessel functions defines the radial change in voltage referenced to axis. For more complicated cases, finding an analytical solution for the potential is very difficult or may not be possible. Numerical approach for calculating the electric field, and thus particle trajectory is widely used. Although the numerical solution of the electrostatic field may need extensive computations, under assumption of paraxial beam, it turns to a simpler numerical problem.

The solution of Laplace equation under axial symmetry assumption can be written in the form of an even power series of r.

$$V(r) = \sum_{0}^{\infty} A_n(z)\ r^{2n} \tag{2.4}$$

The recurrence formula for $A_n(z)$ is derived by substituting the above series in Equation (2.3).

$$A_{n+1} = -\frac{A_n''(z)}{4\ (n+1)^2} \tag{2.5}$$

Now the solution series (2.4) can be written as:

$$V(r, z) = A_0(z) - \frac{A"_0(z)\ r^2}{2^2} + \frac{A_0^{(4)}\ r^4}{2^2.4^2} + ... \tag{2.6}$$

where $A_0(z)$ represents the axial potential, $V(z)$, and leads to immediate relations for axial and radial components of the electric field as a function of the axial potential.

$$E_z = -\frac{\partial V}{\partial z} = -V' \tag{2.7}$$

$$E_r = -\frac{\partial V}{\partial r} = -\frac{r}{2}V" \tag{2.8}$$

The total energy of the particle remains constant and equal to the initial retarding potential along the beam path. Equation(2.9) represents the case in which the axial velocity is so much greater than the radial velocity in an axisymmetric field.

$$\frac{1}{2}m(\frac{dz}{dt})^2 + qV = \phi_0 \tag{2.9}$$

Where q, m, V, z, ϕ_0 are the particle charge and mass, potential, axial coordinate and retarding potential respectively. The radial motion of the projectile is governed by Newton's law:

$$m\frac{d^2r}{dt^2} = qE_r = \frac{qr}{2}V" \tag{2.10}$$

Equation (2.10) reduces to a second order differential equation for r(z) when combined with Equation (2.9).

$$\frac{d^2r}{dz^2} + \frac{1}{2}\frac{V'}{V}\frac{dr}{dz} = -\frac{r}{4}\frac{V"}{V} \tag{2.11}$$

Note that the charge to mass ratio of the particle does not appear in this equation. The trajectory of the beam is determined by integrating above equation using as initial

condition the initial point and velocity of the droplets. This equation requires obtaining the first and second derivative of the axial potential. Since the potential field is normally calculated numerically, the second derivative adds up to the error when integrating along the trajectory. In order to avoid this, another reduction approach is suggested by introducing a reduced radius, R, defined by $R = r\ V^{(1/4)}$. When $r(R, V)$ from this definition is substituted in Equation (2.11), a reduced equation of motion, known as the Pitch equation is obtained:

$$\frac{d^2R}{dz^2} = -\frac{3}{16}R\,(\frac{V'}{V})^2 \tag{2.12}$$

2.3 Numerical Simulation of Electric Field

In our study, COMSOL multiphysics software is used for modeling the electric field. An external MATLAB function executes the finite element model in electrostatic module. The geometry and the physical parameters can be set externally in the MATLAB function. This capability allows us to simulate the possible imperfection in the experiment setup without changing the original COMSOL model in COMSOL GUI. The electric field and potential derived from the COMSOL model are then processed with a Gaussian process regression to reach a smooth field as opposed to the original field which is limited by the mesh resolution. The equation of motion is integrated using Runge Kutta method in MATLAB.

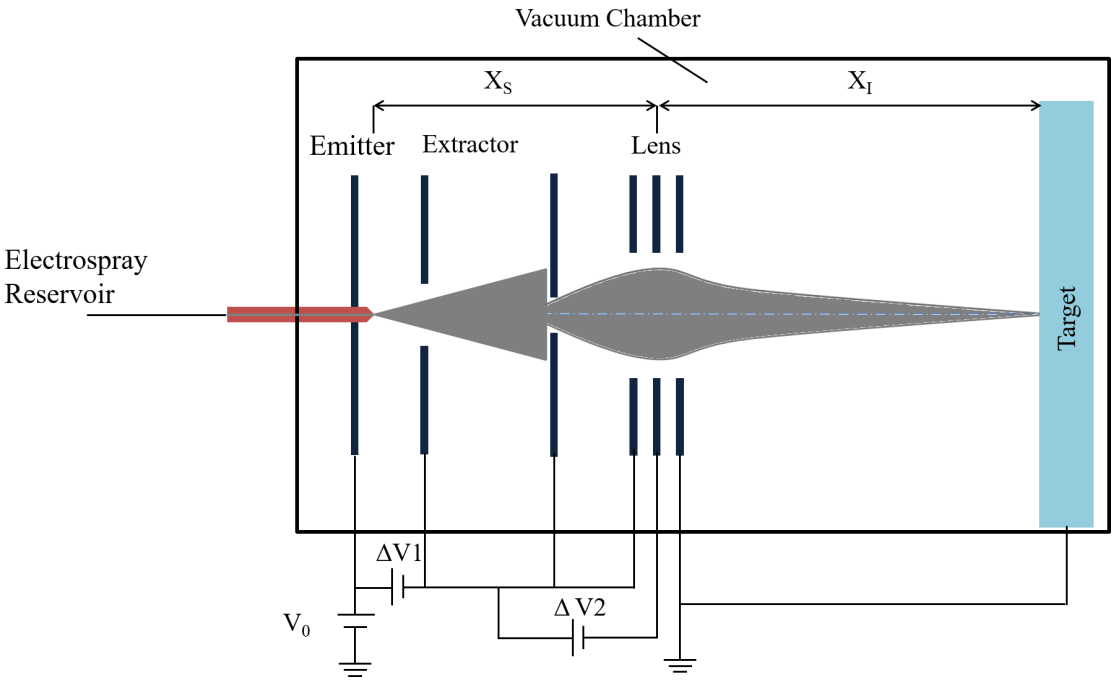

Figure 2.3: Schematic of the focused electrospray beam column.

Figure 2.3 shows a sketch of the potential differences applied to the column. The potential V_{EM} is applied to the ionic liquid source. A voltage difference δV_1 between emitter and extractor is applied to atomize the fluid. The electric field is zero between the extractor electrode and the electrostatic lens. The third electrode of the lens and the target are grounded. The potential of the middle electrode is adjusted as a fraction of the extractor voltage to create the desired image on the target. An example of the simulated electric potential and electric field in the lens are shown in Figure 2.4, using the following conditions: $V_2 = 0.5V_{EXT}$.

Once the electric potential and field are derived, the electrostatic lens is characterized by calculating the focal points and image points for the specified geometry. The axial electric potential and field are derived from above simulation and calculated for middle electrode voltage of between $0.2 \sim 1.2\ V_{EXT}$. See Figure 2.5.

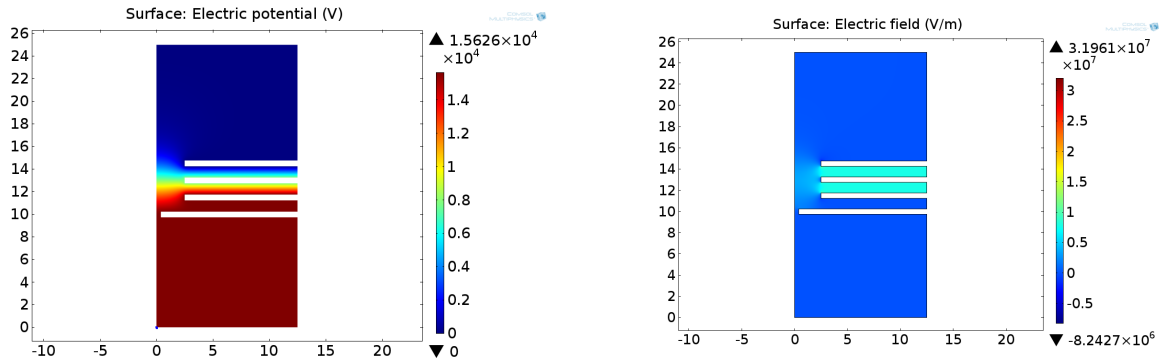

(a) (b)

Figure 2.4: Electric potential and field on the axisymmetric lens model $V_2 = 0.5V_{EXT}$.

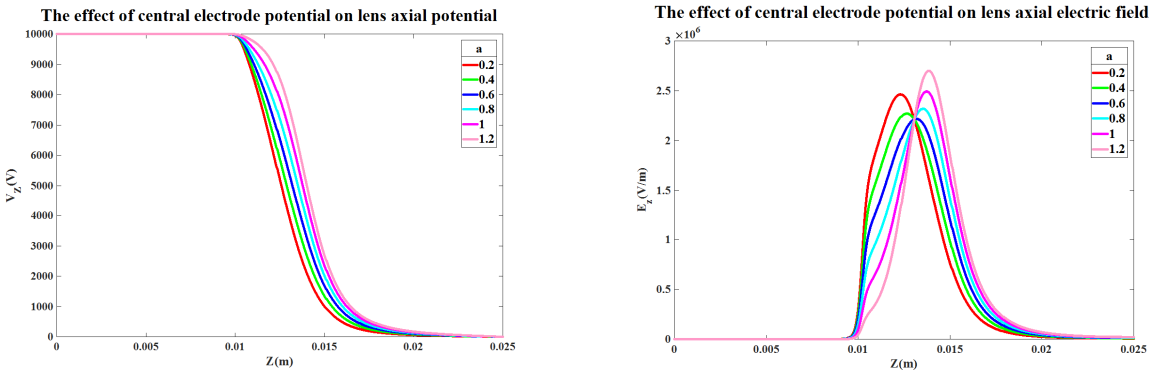

(a) (b)

Figure 2.5: Axial electric potential and field for $V = aV_{Ext}$, $a = 0.2 \sim 1.2$.

2.4 Charged Particle Tracing

A voltage loss of $200V$ during the emission process is taken into account to simulate the particle trajectories. Forward and backward trajectories in the paraxial approximation are integrated using three different approaches. The accuracy of the reduced Pitch equation, Equation (2.12), is verified compared to the time integration method, Equation (2.11). For the initial radial position of 0.392 mm for the beam (skimmer aperture radius), both methods

show a good agreement with maximum difference up to 0.2 μm according to Figure 2.4. Matlab ODE 45 integration was used for all three differential equation with integration tolerance for all variables set to 10^{-9}.

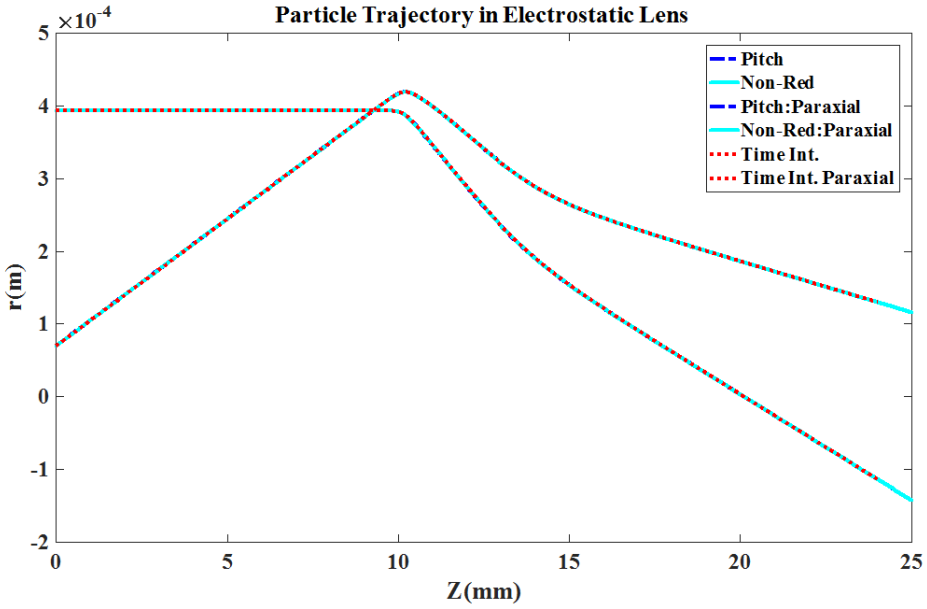

Figure 2.6: Trajectory of the paraxial beam in Einzel electrostatic lens by Pitch equation, (2.12) (- - -); nonreduced equation, (2.11) (—); and second order time dependent differential equation, (2.10) (·····).

The first and second focal points are calculated by integrating the equation of motion using different values of V_2 for paraxial beams. Knowing the image location for a fixed position of the point source on the axis is important in order to be able to locate the target as close as possible to the image point and take advantage of the focused beam energy. In practice the voltage on the central electrode is adjusted to focus the beam on the fixed target, (see Figure 2.8). According to this analysis, the image of the fixed source is formed at the farthest point from center of the lens when $V_2 = V_{Ext}$. Simulation error is expected to some extent since all the parameters in Equation (2.1) are determined numerically.

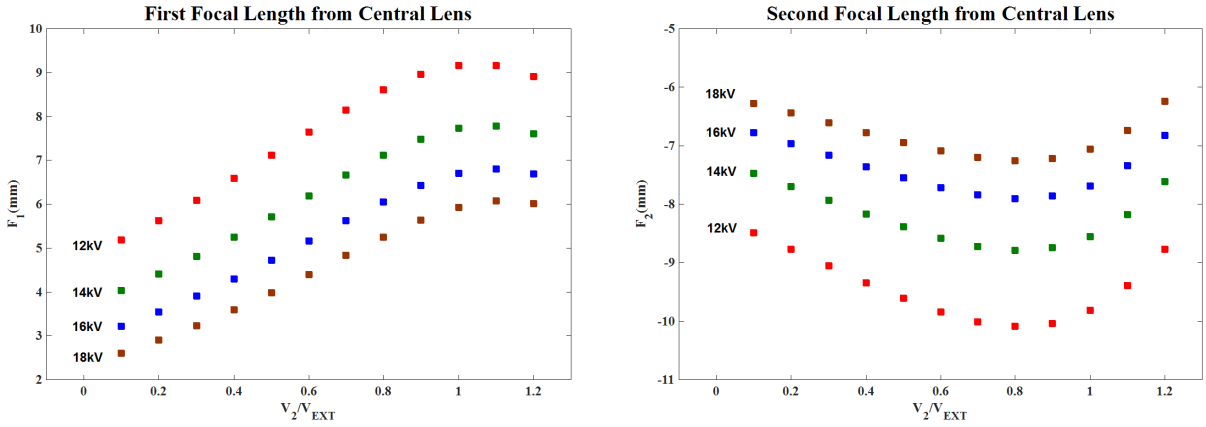

(a) (b)

Figure 2.7: First and Second Focal points of the Einzel lens from center for a range of Extractor and middle electrodes potential, by Pitch equation, Equation (2.12).

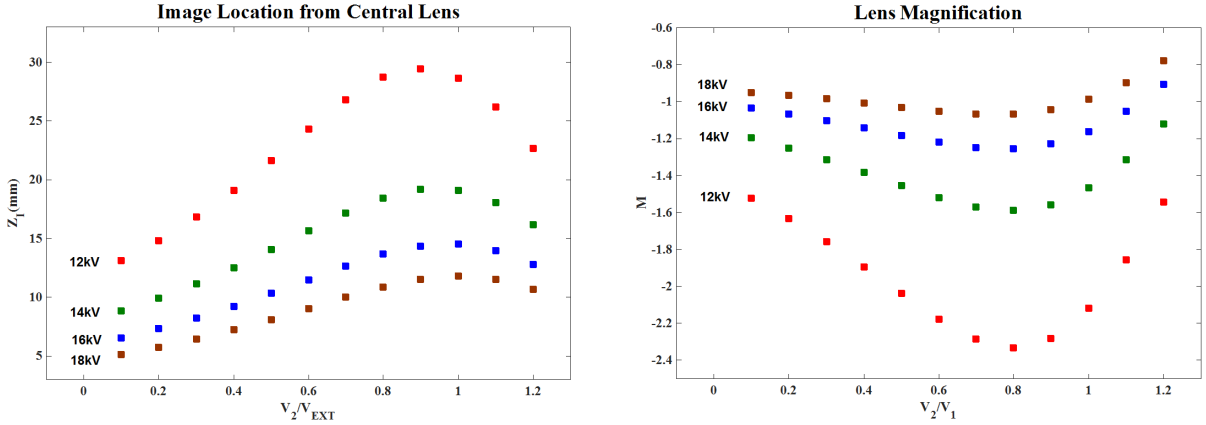

(a) (b)

Figure 2.8: Image location for a fixed point source on the axis $-14.5\ mm$ upstream from the center of the lens and lens magnification.

2.5 Aberrations

In the paraxial approximation the third and higher order terms of the potential were ignored in particle tracing, and particle trajectory was solved for homogeneous energy distribution. This linear approximation estimates the Guassian image distance from the lens but it fails to describe the difference between the actual and expected magnified image. Several factors are known to cause aberrations. We will discuss aberrations in electrostatic lens, including *Geometrical Aberrations* including, *Spherical Aberration, Astigmatism, Coma, Distortion, Curvature of Field*, and *Chromatic Aberration*. The numerical results will be compared to experimental data and used to characterize the focusing setup presented in chapter 3. Spherical Aberration depends on the slopes of the droplets' trajectories. Astigmatism is an off-axis aberration which is the result of misalignment and aperture imperfections. Chromatic Aberration is caused by non-homogeneous energy spread across the particle beam. [69] In the method of characteristics function, the third order trajectory is treated as the perturbation of the paraxial trajectory. The characteristics function or point eikonal refers to the Hamiltonian function which defines the charged particle trajectory. Its variational function also represents the refraction index of the charged particle and minimizes the particle's traveling path in electrostatic field (Fermat's Principle): [76]

$$kdz = nds \tag{2.13}$$

$$\delta \int_a^b K dz = \delta S_{AB} = 0 \tag{2.14}$$

Here, n is the index of refraction, ds is the path element and z is the independent coor-

dinate. S is characteristics equation. The variational function K is the particle momentum in electrostatic field.

$$K = p = m_0\, v = (-2\, m_0\, q\ [\phi - \phi_0])^{\frac{1}{2}} = \left(-2\, q\, m_0 \left[V(z) - V_0 - V"(z)\frac{(x^2+y^2)}{4} + V^{IV}(z)\frac{(x^2+y^2)^2}{64} \right] \right)^{1/2} \quad (2.15)$$

Using a Taylor series to expand the above relationship, K is written as a sum of three terms. The first term depends only on the axial potential and initial position of the charged particle and will not appear in Euler equations for trajectory. In our trajectory integration only the second term was taken into account for paraxial beam. The last term shows dependency of final image on higher order terms of axial potential, initial position and direction of particle which was ignored before.

$$K = K_0 + K_2 + K_4 \quad (2.16)$$

$$K_0 = \{(-2\, m_0\, q\ [V(z) - V_0]\}^{\frac{1}{2}} \quad (2.17)$$

$$K_2 = K_0\ \left\{ \frac{(x'^2 + y'^2)}{2} - \frac{(x^2+y^2)}{8\,[V(z) - V_0]} V"(z) \right\} \quad (2.18)$$

$$K_4 = K_0 \left\langle \frac{\left(x^2+y^2\right)^2}{128\ [V(z)-V_0]} \left\{ V^{(IV)(z)} - \frac{[V"(z)]^2}{[V(z)-V_0]} \right\} - \frac{\left(x'^2+y'^2\right)\ \left(x^2+y^2\right)}{16\ [V(z)-V_0]} V"(z) - \frac{\left(x'^2+y'^2\right)^2}{8} \right\rangle \tag{2.19}$$

Szilagyi [68] discusses the characteristics function method in detail in his book and describes the geometric aberration terms as a result of K_4 perturbation along unperturbed trajectory and the variation of the characteristics function.

2.6 Spherical Aberration

The charged droplets with higher emitting angle are subject to a stronger electrostatic force and more deflection. Therefore, rays from a point source with different emission angles do not converge at one point and do not form a point image at the Gaussian image plane. Instead they intersect the axis before the image point and form a disk image on the image plane. The radius of the disk (δr_{si}) is the difference between the radial displacement of the outermost ray from Gaussian image by paraxial rays.

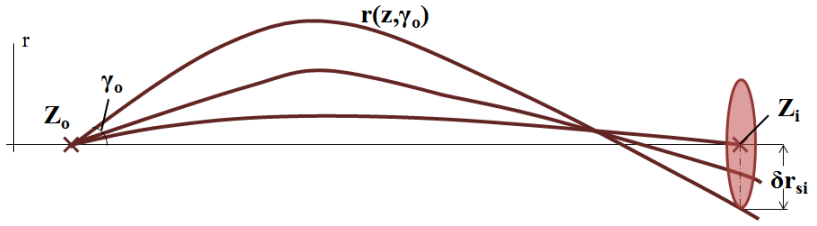

Figure 2.9: Schematic of spherical aberrated rays

The spherical aberration figure (δr_{si}) is found to be proportional to $tan^3\gamma_0$ where γ_0 is

the acceptance half angle of the beam or outermost ray angle.

$$\delta r_{si} = A_1 \, tan^3\gamma_0 = C_{so} \, M \, tan^3\gamma_0 \tag{2.20}$$

C_{so} is called the spherical aberration coefficient, which is calculated by the characteristics method as follows:

$$\begin{aligned} C_{so} = \frac{1}{16} \int_{z_o}^{z_i} \left[\frac{V(z) - V_0}{V(z_0) - V_0} \right]^{1/2} \frac{h^4 \, dz}{[V(z) - V_0]^2} \left\{ \frac{5}{4} \, V"^2(z) + ... \right. \\ \left. ... \frac{5}{24 \; [V(z) - V_0]^2} \, V'^4(z) + \frac{14}{3 \; [V(z) - V_0]} \, \frac{h'}{h} \, V'^3(z) - \frac{3}{2} \, \frac{h'^2}{h^2} \, V'^2(z) \right\} \end{aligned} \tag{2.21}$$

h and g are two independent paraxial trajectories with the following initial condition:

$$\begin{aligned} g(Z_o) = 1 \quad h(Z_o) = 0 \\ g'(Z_o) = 0 \quad h'(Z_o) = 1 \end{aligned} \tag{2.22}$$

A linear superposition of these two principle trajectories form the general solution of the lens tracing equations, Equation (2.12), as follows:

$$\begin{aligned} X(z) = \; X(z_0) \, g(z) \; + \; X'(z_0) \, h(z) \\ Y(z) = \; Y(z_0) \, g(z) \; + \; Y'(z_0) \, h(z) \end{aligned} \tag{2.23}$$

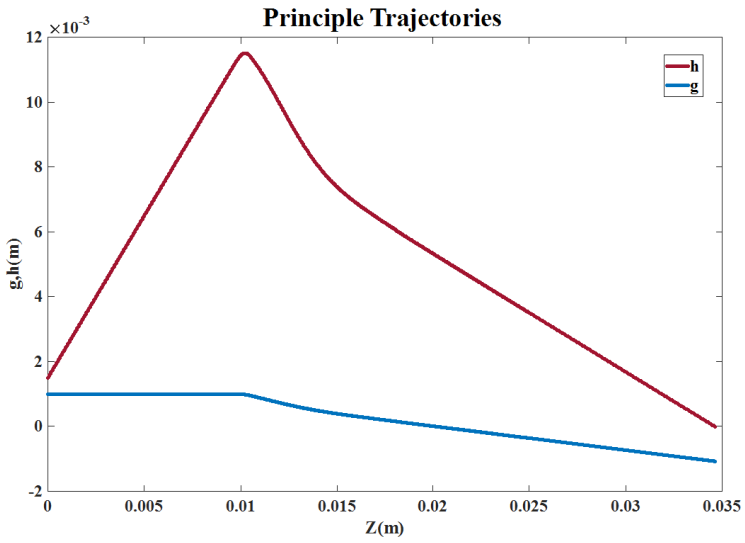

Figure 2.10: Principle paraxial trajectories, h and g, form the general solution of the lens trajectory Equation (2.12).

Since the spherical aberration depends on the trajectory slope and not misalignment in the source position, it cannot be completely compensated by other means. If the half acceptance angle of the beam is limited, the trajectory becomes closer to the paraxial approximation and the spherical aberration figure is minimized. The spherical aberration figure for our electrospray beam with 2 deg is calculated with the above formula in Figure 2.6. Regardless of the emitter potential value, the spherical aberration figure decreases for higher potentials applied on the middle electrode and it is is minimized at $V_2 = 1.1\ V_{EXT}$. In this case, a disk of 34 μm is expected for the emitter potential of 12 kV.

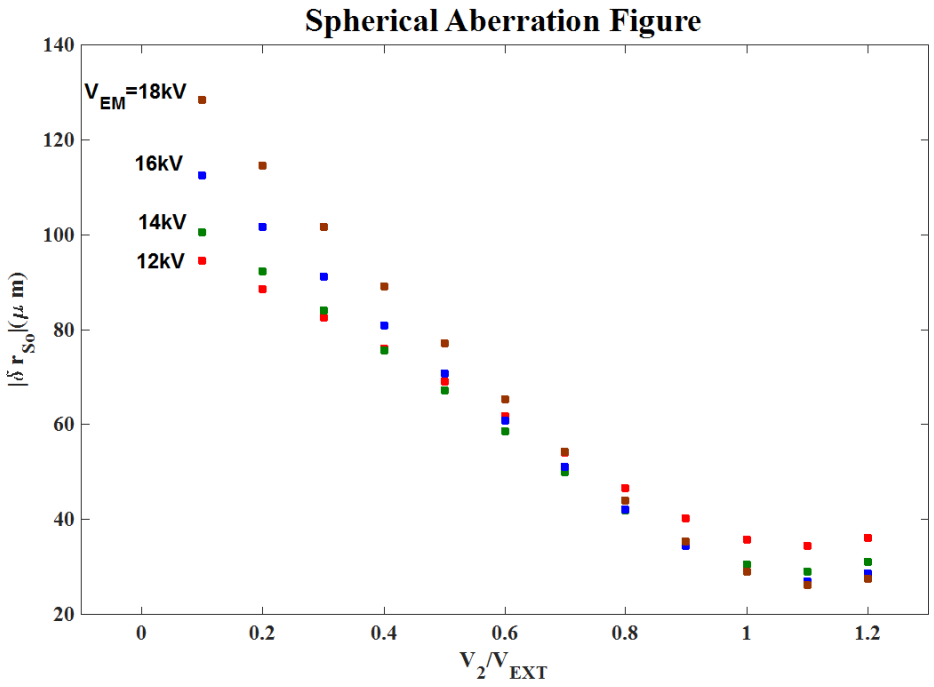

Figure 2.11: Absolute value of Spherical aberration figure calculated for a range of emitter and central electrode potentials.

The disc of minimum confusion is defined somewhere before the Gaussian image plane where the cross section of the beam is minimized. The location of the minimum confusion disk is specially of interest for placing the probes and targets where the beam is most focused rather than Gaussian image with aberration. The radius of the disk of minimum confusion is one quarter of the spherical aberration figure ($\delta r_{si}/4$). It is located at $\frac{3}{4}L$ from Gaussian image plane (The outermost ray intersects the axis in distance L from the Gaussian image plane).

2.7 Astigmatism

When the beam converges at different rates in different planes, the cone beam turns to elliptical beam and particles reach the Gaussian plane along a line in radial direction. This aberration is known as astigmatism and the aberration figure is the line. Although the astigmatism is eliminated if the electrospray source is located on the axis, a paraxial beam may still be subject to astigmatism. This is the case which electrostatic field is not accurately axisymmetric because of misalignments and manufacturing imperfections. The elliptical beam turns into two straight lines on two curved images surfaces known as the tangential and sagittal images surfaces. Somewhere between these two image surfaces, the beam cross section becomes circular. Schematic below shows how an astigmatic beam from off-axis source degenerates into straight lines on tangential and sagittal surfaces. Instead of actual particle trajectories, asymptotic rays are considered for simplicity.

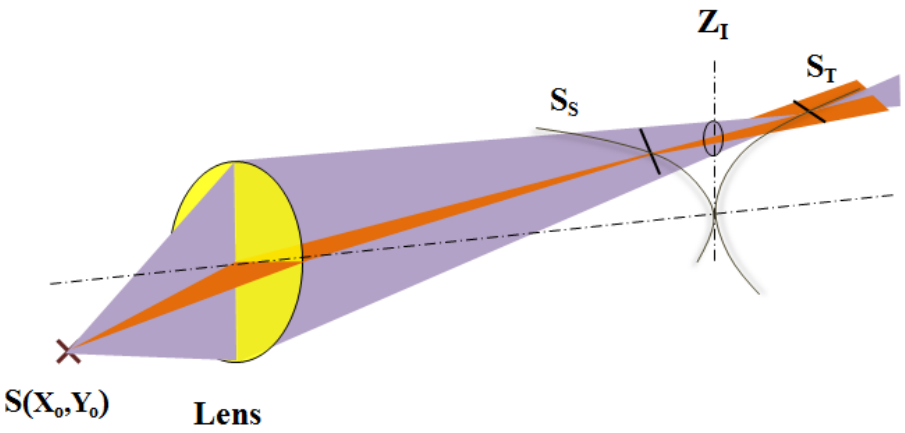

Figure 2.12: Schematic of astigmatic rays

In case of paraxial beam, those two lines and the circle coincide. The deviation from Gaussian image depends on the initial coordinates of the particle (X_0, Y_0) and the emission

angle γ_0.

$$\begin{aligned}
\delta X(Z_i) &= 2A\ (X_0^2\ X_0' + X_0\ Y_0\ Y_0') \\
\delta Y(Z_i) &= 2A\ (X_0\ Y_0\ X_0' + Y_0^2\ Y_0') \\
\delta Y(Z_i) &= \tfrac{Y_0}{X_0}\ \delta X(Z_i)
\end{aligned} \tag{2.24}$$

The coefficient of astigmatism shown by Szilagyi [68] has higher order derivatives of axial potential. After executing an integration by part on the higher terms, only up to second order terms remain.

$$\begin{aligned}
A = &\frac{M}{32}\int_{z_o}^{z_i}\left[\frac{V(z)-V_0}{V(z_0)-V_0}\right]^{1/2}\Bigg\{\frac{3\,V"^2}{2\ [V(z)-V_0]^2}\ g^2\ h^2 + \frac{8\,V"(z)}{[V(z)-V_0]}\ g\ g'\ h\ h' + \\
&16\ g'^2\ h'^2 - \frac{2\,V'(z)\,V"(z)}{[V(z)-V_0]^2}\ (g\ g'\ h^2 + g^2\ h\ h') - \\
&\frac{2\,V"(z)}{[V(z)-V_0]}(g'^2\ h^2 + g\ g"\ h^2 + 8\ g\ g'\ h\ h' + g^2\ h'^2 + g^2\ h'\ h") - \\
&\frac{3\,V'^2(z)\,V"(z)}{[V(z)-V_0]^3}\ g^2\ h^2\Bigg\}dz
\end{aligned} \tag{2.25}$$

The aberration figure size is compared for a range of emitter and central electrode potentials below assuming the source is deviated from center as much as 20 μm. This is the radius of the capillary tube. This assumption is only for the deflection of the electrospray cone-jet from the axis. The misalignment in source or each of the electrodes will add to this value and result in higher astigmatism figure.

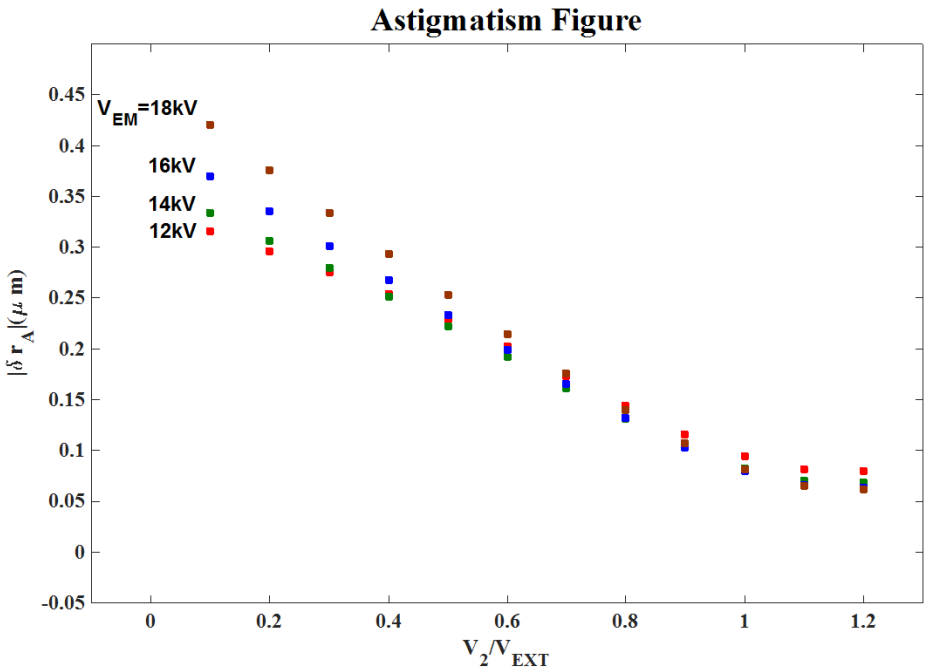

Figure 2.13: Absolute value of Astigmatism calculated for a range of emitter and central electrode potentials.

2.8 Chromatic Aberration

The electrostatic field affects the trajectory of low-energy particles more than high-energy particles across the beam. This phenomenon defines another type of aberration which causes a blurry image. Particles with different velocities, corresponding with high or low energy levels, reach the axis in different points and form the image after or before the Gaussian image formed by average-energy particles. Since it is impossible to produce a monochromic beam, the chromatic aberration is always expected to affect the sharpness of the image. For a beam with homogenous energy distribution, its effect is suppressed. The chromatic aberration is formulated by applying the method of characteristics function on variational function K_2 and trajectory perturbation due to potential variation. The trajectory deviation

includes axial C_1 and magnification C_2 chromatic aberration terms:

$$\begin{aligned} \delta X(Z_i) &= -M(C_1\ X_0' + C_2\ X_0) \\ \delta Y(Z_i) &= -M(C_1\ Y_0' + C_2\ Y_0) \end{aligned} \tag{2.26}$$

where the axial and magnification chromatic coefficient C_1 and C_2 are:

$$C_1 = \int_{z_o}^{z_i} \left[\frac{V(z) - V_0}{V(z_0) - V_0}\right]^{1/2} \left\{\frac{3\ V'^2(z)}{\left[V(z) - V_0\right]^2}\ h^2\right\}\ dz \tag{2.27}$$

$$C_2 = \int_{z_o}^{z_i} \left[\frac{V(z) - V_0}{V(z_0) - V_0}\right]^{1/2} \left\{\frac{V"(z)}{\left[V(z) - V_0\right]^2}\ gh + \frac{g'h'}{2}\right\}\ dz \tag{2.28}$$

The chromatic aberration figure for axial source depends on the half acceptance angle and the energy spread ΔV_0:

$$\delta r_{ci1} = M\ C_1\ tan\gamma_0\ \frac{\Delta V_0}{2\left[V(z_0) - V_0\right]} \tag{2.29}$$

If the magnification term exist, the chromatic aberration figure δr_{ci2} is:

$$\delta r_{ci2} = M\ C_2\ \left(X_0^2 + Y_0^2\right)^{1/2} \frac{\Delta V_0}{2\left[V(z_0) - V_0\right]} \tag{2.30}$$

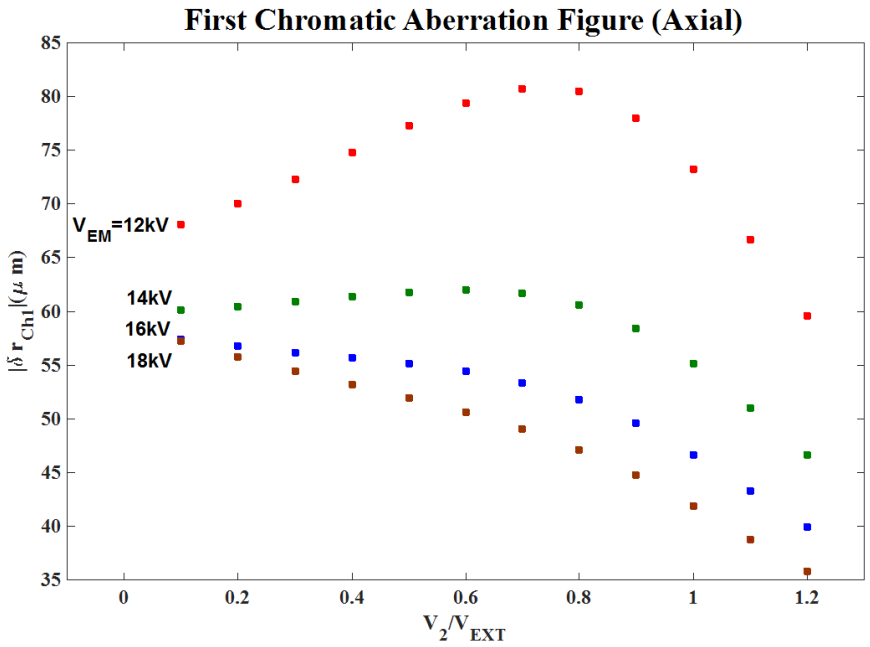

Figure 2.14: Absolute value of axial Chromatic aberration figure calculated for a range of emitter and central electrode potentials.

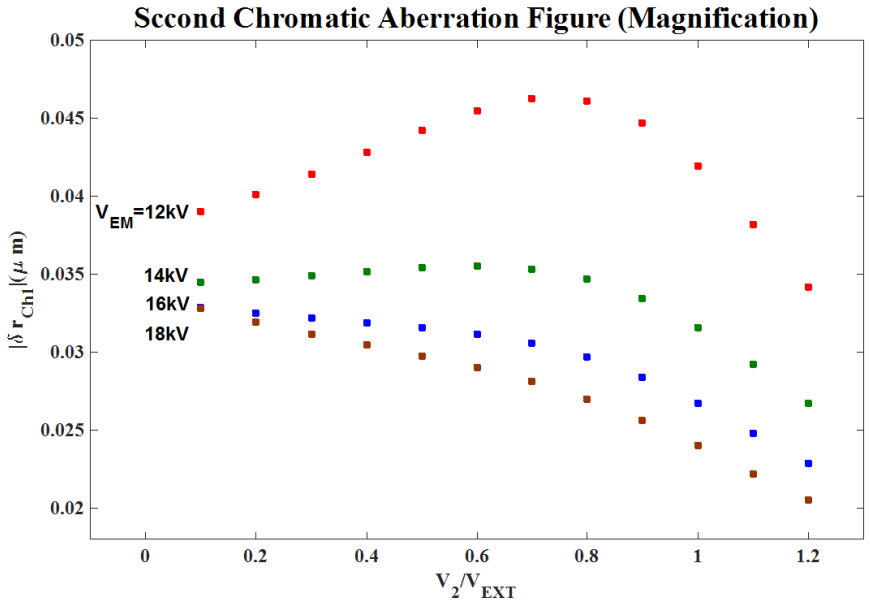

Figure 2.15: Absolute value of magnification chromatic aberration figure calculated for a range of emitter and central electrode potentials.

Axial chromatic aberration always affects the beam even for axial source. It can be seen that the axial chromatic aberration coefficient never changes sign so it cannot be compensated by another axisymmetric field. Chromatic aberration is similar and comparable to spherical aberration in that sense. Spherical aberration is dominant for larger aperture which provides higher slope due and chromatic aberration dominates in beams with lower half acceptance angle. The voltage difference across the beam for electrospray source has been measured in another research [25] and will be used in our numerical models here, The maximum energy change of $\delta V = 200V$ is reported.

The aberration figure is also could be seen in closed form solution as deviation of the trajectory because of the energy spread δV. The trajectory equation, Equation (2.11), for the charged particle with $V + \delta V$ is the following:

$$\frac{d^2r}{dz^2} + \frac{1}{2}\frac{V'}{V+\delta V}\frac{dr}{dz} = -\frac{r}{4}\frac{V"}{V+\delta V} \tag{2.31}$$

Above equation is written in the following matrix form after multiplying $\frac{V-\delta V}{V-\delta V}$. The term δV^2 is very small compared to large V and it is ignored.

$$\begin{pmatrix} r' \\ r" \end{pmatrix} = (A + \delta A) \begin{pmatrix} r \\ r' \end{pmatrix} \tag{2.32}$$

where A represents the unperturbed trajectory coefficient matrix and δA illustrates the effect of spread energy δV on trajectory, both of which depend on the potential distribution

along the axis.

$$A = \begin{pmatrix} 0 & 1 \\ -\frac{1}{4}\frac{V"}{V} & -\frac{1}{2}\frac{V'}{V} \end{pmatrix} \qquad \delta A = \begin{pmatrix} 0 & 0 \\ \frac{1}{4}\frac{V"}{V^2}\ \delta V & \frac{1}{2}\frac{V'}{V^2}\ \delta V \end{pmatrix} \tag{2.33}$$

The deviation of the particle trajectory is formed by integrating the solution of Equation (2.35) along the axis for the small increments where matrix coefficient δA is constant.

$$\begin{pmatrix} r \\ r' \end{pmatrix} = e^{(A+\delta A)z} \begin{pmatrix} r_0 \\ r'_0 \end{pmatrix} = \left(I + (A+\delta A) + \frac{1}{2}(A+\delta A)^2 + ... \right) z \begin{pmatrix} r_0 \\ r'_0 \end{pmatrix} \tag{2.34}$$

$$\delta \begin{pmatrix} r \\ r' \end{pmatrix} = \begin{pmatrix} \frac{1}{4}\frac{V"}{V^2}\delta V & \frac{1}{2}\frac{V'}{V^2}\delta V \\ -\frac{1}{8}\frac{V"V'}{V^3}\delta V & -\frac{1}{4}\frac{V'^2}{V^3}\delta V \end{pmatrix} z \begin{pmatrix} r_0 \\ r'_0 \end{pmatrix} \tag{2.35}$$

Here $\binom{r_0}{r'_0}$ represents the position vector of particle from last position increment. And integrating over the length of the focusing field from source to image defines the chromatic aberration in Gaussian image.

$$\Delta r_C = \int_{Z_0}^{Z_i} \left[\frac{1}{4}\frac{V"}{V^2}\ r + \frac{1}{2}\frac{V'}{V^2}\ r' \right] \delta V\ dz \tag{2.36}$$

Since the above expression for chromatic aberration figure relies on the ideal particle trajectory solution, it may not be useful in design or calibration experiments without integrating the particle trajectory equation. However, it is beneficial to compare the result from this simple closed form analysis with the one from method of characteristics.

Finally, the combination of all these error sources form a blurry disc on the image plane

around the original point image. As an example, a comparison between aberrated image with Astigmatism, Spherical,and chromatic aberrations, as previously discussed, gives an image size up to 105 μm for $V_2 = 0.5\ V_{EXT}$.

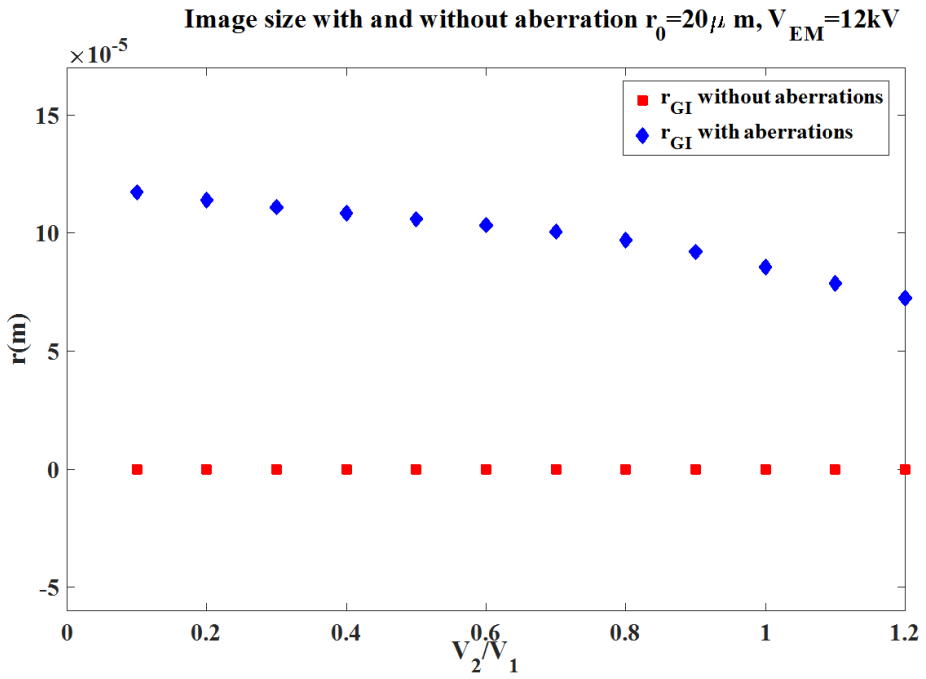

Figure 2.16: Total aberration disc compared to the image radial location on Gaussian image plan.

In addition to the aberration figures that were discussed and shown in previous sections, there are a few other terms adding up to the error seen on the image plane. These aberration terms might be negligible when compared to spherical aberration or chromatic aberration, but they affect the shape of the image like astigmatism. In the following, the other three aberration sources are described. Note that anisotropic aberration terms are not discussed in this chapter because only electrostatic lens is used for focusing the beam and no magnetic field exists.

2.8.1 Distortion

This source of error interfere with the linear relationship between the source and image. Even for very narrow beam which paraxial assumtion is valid, an offset from lens axis is seen as a shift of the Gaussian image plane along the axis. Distortion does not introduce a circle for each point and blurriness at the true image plane but changes the shape of the image on the linear Gaussian image plane. For instance, what appears as image of a square on the linear Gaussian image plane is in the form of a distorted barrel or cushion. This aberration figure depends on the cube of point distance from lens axis. But the kind of distortion depends on sign of the aberration coefficient.

$$\begin{aligned} \delta X(Z_i) &= A_D\ X_0\ (X_0^2 + Y_0^2) \\ \delta Y(Z_i) &= A_D\ Y_0\ (X_0^2 + Y_0^2) \end{aligned} \tag{2.37}$$

$$\delta r_i = A_D\ (X_0^2 + Y_0^2)^{3/2} \tag{2.38}$$

$\delta\ r_D i$ is the shift of the image plan not the radius. The aberration coefficient is derived as following:

$$A_D = \frac{M}{32}\int_{z_o}^{z_i}\left[\frac{V(z)-V_0}{V(z_0)-V_0}\right]^{1/2}\left\{\frac{V"^2}{[V(z)-V_0]^2}\ h\ g^3+\frac{4\,V"(z)}{[V(z)-V_0]}\ g\ g'\ (h\ g'+h'\ g)+\right.$$
$$16\ h'\ g'^3-\frac{V'(z)\ V"(z)}{[V(z)-V_0]}\ (h'\ g^3+3\ h\ g^2\ g')-$$
$$\frac{V"(z)}{[V(z)-V_0]}(h"\ g^3+6h'\ g'\ g^2+3\ h\ g"\ g^2+6\ h\ g'^2\ g)-$$
$$\left.\frac{3\,V'^2(z)\ V"(z)}{4\,[V(z)-V_0]^3}\ g^3\ h\right\}dz \tag{2.39}$$

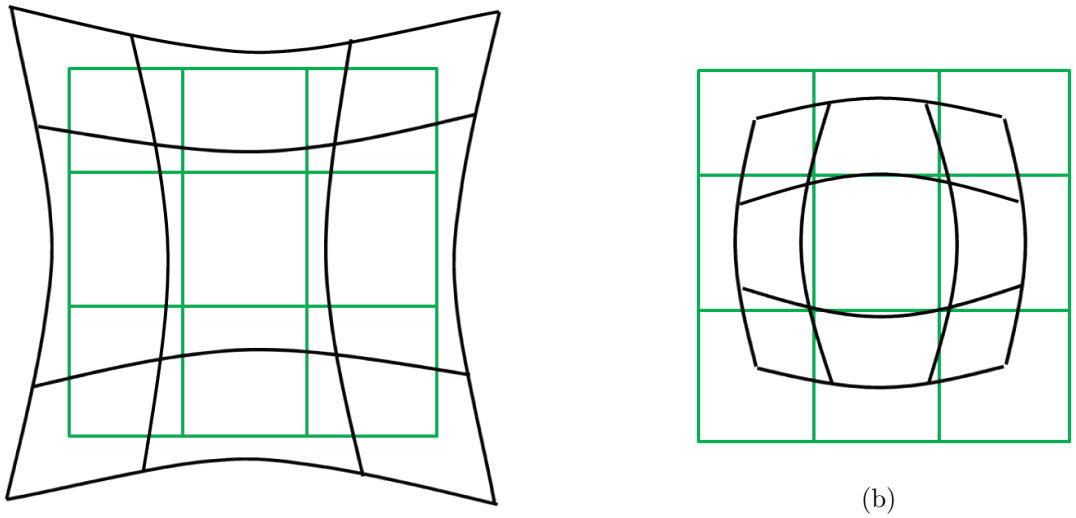

(a) (b)

Figure 2.17: Object(—), distoreted image(—)(a) Cushion distortion, (b) Barrel distortion.

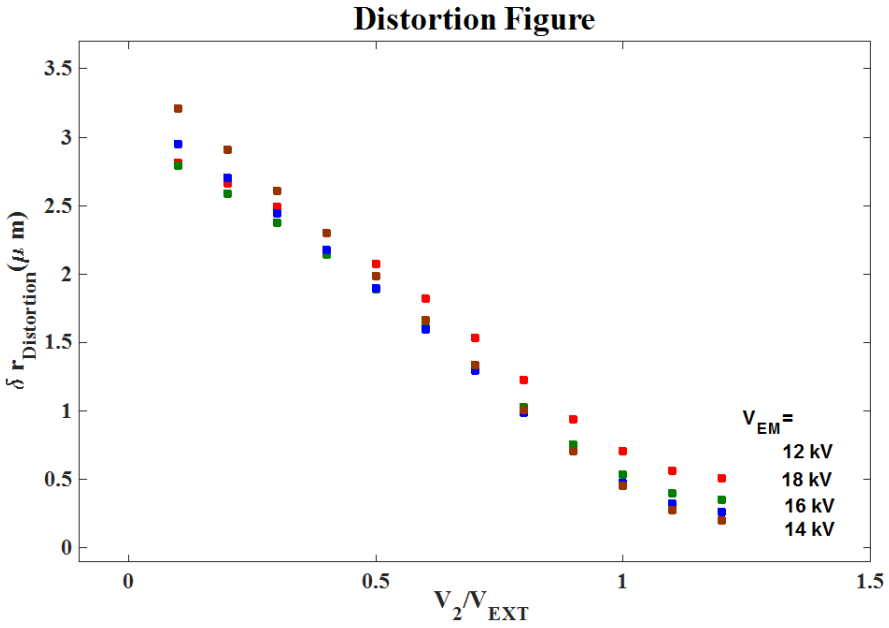

Figure 2.18: Distortion aberration figure calculated for a range of emitter and central electrode potentials.

2.8.2 Coma

Coma is another type of aberration that makes the image of a point source appears as a set of circles on the image plane. δX and δY due to aberration are:

$$\begin{aligned} \delta X(Z_i) &= A_{coma}\,[X_0\,(X_0'^2 + Y_0'^2) + 2\,X_0'\,(X_0\,X_0' + Y_0\,Y_0')] \\ \delta Y(Z_i) &= A_{coma}\,[Y_0\,(X_0'^2 + Y_0'^2) + 2\,Y_0'\,(X_0\,X_0' + Y_0\,Y_0')] \end{aligned} \tag{2.40}$$

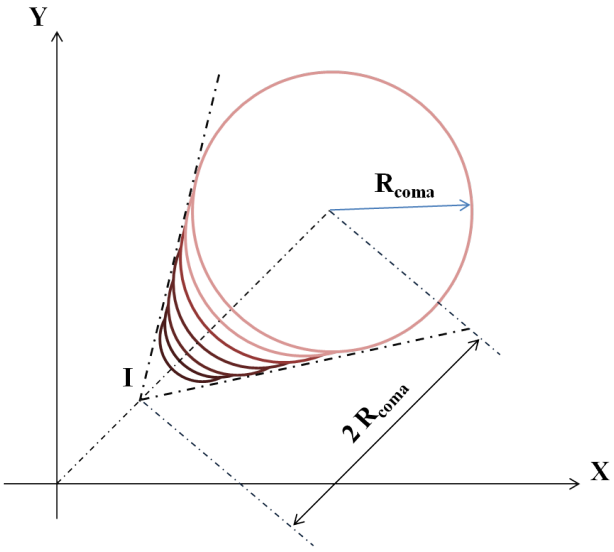

Figure 2.19: Image under coma aberration.

The radius of the largest image is R_{coma} and its center located at the X_c and Y_c or 2 R_{coma} from image point at the Gaussian plane:

$$R_{coma} = A_{coma}\ (X_0^2 + Y_0^2)^{1/2}\ tan^2\gamma_0 \tag{2.41}$$

$$\begin{aligned} X_c &= X_i + 2\ A_{coma}\ X_0\ (X_0'^2 + X_0'^2) \\ Y_c &= Y_i + 2\ A_{coma}\ Y_0\ (X_0'^2 + X_0'^2) \end{aligned} \tag{2.42}$$

where aberration coefficient A_{coma} is:

$$A_{coma} = \frac{M}{32}\int_{z_o}^{z_i}\left[\frac{V(z)-V_0}{V(z_0)-V_0}\right]^{1/2}\left\{\frac{V"^2}{[V(z)-V_0]^2}\, g\, h^3 + \frac{4\,V"(z)}{[V(z)-V_0]}\, h\, h'\,(g\,h' + g'\,h) + \right.$$
$$16\, g'\, h'^3 - \frac{V'(z)\,V"(z)}{[V(z)-V_0]}\,(g'\,h^3 + 3\,g\,h^2\,h') -$$
$$\frac{V"(z)}{[V(z)-V_0]}(g"\,h^3 + 6g'\,h'\,h^2 + 3\,g\,h"\,g^2 + 6\,g\,h'^2\,g) -$$
$$\left.\frac{3\,V'^2(z)\,V"(z)}{4\,[V(z)-V_0]^3}\, h^3\, g\right\} dz \tag{2.43}$$

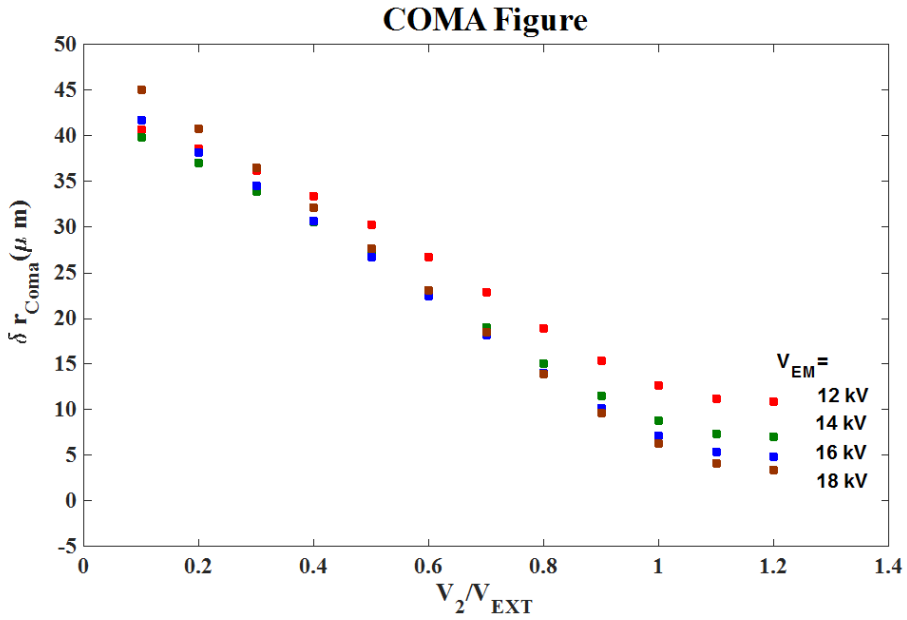

Figure 2.20: Coma aberration figure calculated for a range of emitter and central electrode potentials.

2.8.3 Curvature of Field

In the presence of curvature of field aberration, the image is formed at a curved surface that touched the Gaussian plane at the image point. The aberration figure in this case is also a circle. The radius of the circle is proportional to projectiles initial slope and the square distance of the source distance from lens axis.

$$\begin{aligned} \delta X(Z_i) &= A_{cu}\ X_0'\ (X_0^2 + Y_0^2) \\ \delta Y(Z_i) &= A_{cu}\ Y_0'\ (X_0^2 + Y_0^2) \end{aligned} \tag{2.44}$$

$$\begin{aligned} \delta\ r_{cui} &= A_c u\ (X_0^2 + Y_0^2)(X_0'^2 + Y_0'^2)^{1/2} \\ &\leq\ A_c u\ (X_0^2 + Y_0^2)\ tan\gamma_0 \end{aligned} \tag{2.45}$$

$$\begin{aligned} A_{cu} = & \frac{M}{32} \int_{z_o}^{z_i} \left[\frac{V(z) - V_0}{V(z_0) - V_0} \right]^{1/2} \left\{ \frac{3\ V"^2}{2\ \left[V(z) - V_0\right]^2}\ g^2\ h^2 + \frac{4\ V"(z)}{\left[V(z) - V_0\right]}\ (g^2\ h'^2 + g'^2\ h^2) + \right. \\ & 16\ g'^2\ h'^2 - \frac{2\ V'(z)\ V"(z)}{\left[V(z) - V_0\right]^2}\ (g\ g'\ h^2 + g^2\ h\ h') - \\ & \frac{2\ V"(z)}{\left[V(z) - V_0\right]} (g'^2\ h^2 + g\ g"\ h^2 + 8\ g\ g'\ h\ h' + g^2\ h'^2 + g^2\ h'\ h") - \\ & \left. \frac{3\ V'^2(z)\ V"(z)}{\left[V(z) - V_0\right]^3}\ g^2\ h^2 \right\} dz \end{aligned} \tag{2.46}$$

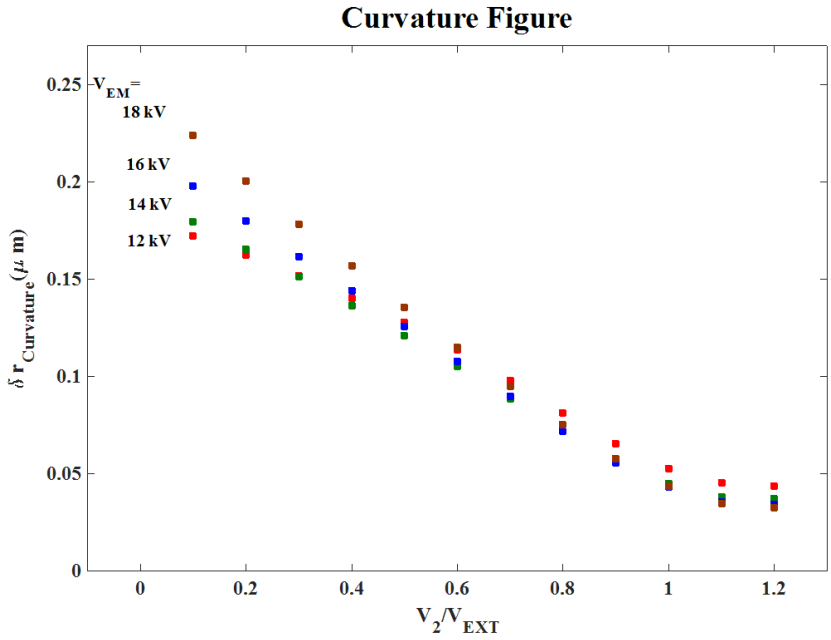

Figure 2.21: Curvature of field aberration figure calculated for a range of emitter and central electrode potentials.

2.9 Beam Deflection

In paraxial trajectory equation in section 2.2, the axial field component in an axisymmetric lens was assumed much stronger than transverse components. The transverse field was shown to focus the beam while accelerating along the axis by axial field. However, a stronger transverse field is needed for beam deflection. Electrostatic multipole lenses are charged particle optics elements with multiple planar symmetry and dominant transverse field for deflecting beam in the direction perpendicular to the axis. In addition to deflection, multipole lenses are used for aberration correction especially astigmatisms. i.e. a negative astigmatism coefficient of a multipole lens compensates for focusing lens astigmatism. [68, 77] This part is not explored experimentally; however, it is mentioned here in order to address a full

theoretical background on focusing and scanning lens. It is possible to combine the focusing and deflecting lens in one multipole lens configuration. [78] In this case the governing equation for focusing and deflecting a paraxial particle trajectory in x and y direction are as following:

$$\begin{aligned} X'' + \left(\frac{V'(z)}{2V(z)}\right) X' + \left(\frac{V''(z)}{4V(z)}\right) X &= \frac{U_1(z)}{2V(z)} \\ Y'' + \left(\frac{V'(z)}{2V(z)}\right) Y' + \left(\frac{V''(z)}{4V(z)}\right) Y &= \frac{W_1)z)}{2V(z)} \end{aligned} \tag{2.47}$$

$V(z)$ is the axisymmetric potential distribution (APD) and $U_1(z)$ and $W_1(z)$ are first harmonic field distribution for x and y deflecting directions. The field distribution of a deflector is given by a series expansion with Fourier coefficients A_m and B_m:

$$\begin{aligned} U(r,\alpha) = & V_f + \sum_{m=0}^{\infty} r^m \; A_m \; Cos\,(m\alpha) \\ & + \sum_{m=0}^{\infty} r^m \; B_m \; Sin\,(m\alpha) \end{aligned} \tag{2.48}$$

where A_m and B_m are defined as following:

$$\begin{aligned} A_m(r,z) &= \sum_{k=0}^{\infty} \frac{(-1)^k \; m!}{4^k \; k! \; (m+k)!} \; r^{2k} \; U_m^{2k}(z) \\ B_m(r,z) &= \sum_{k=0}^{\infty} \frac{(-1)^k \; m!}{4^k \; k! \; (m+k)!} \; r^{2k} \; W_m^{2k}(z) \end{aligned} \tag{2.49}$$

For planar electrodes, A_m and B_m are in fact constant and equal to first harmonic field distribution. The index m also represents the number of the planar symmetry in multipole lens $m = nN$ where N is the number of symmetries perpendicular to the optical axis. For example, $N = 1$ for a deflector, $N = 2$ for a quadrupole lens, and $N = 4$ for an octupole lens. It can be shown that n only takes odd values so the deflection in perpendicular direction are independent. The deflector field for $n = 1 - 3$ in terms of FHFD and THFD is as following:

$$\begin{aligned}
\Phi(r,z,\alpha) = & V(z) - \frac{1}{4}\, V''(z)\, r^2 + \frac{1}{64}\, V^2(z)\, r^4 + \dots \\
& + U_1(z) r\, Cos(\alpha) - \frac{1}{8} U_1''(z) r^2\, Cos(\alpha) + U_3(z) r^3\, Cos(3\alpha) + \dots \\
& + W_1(z) r\, Cos(\alpha) - \frac{1}{8} W_1''(z) r^2\, Cos(\alpha) + W_3(z) r^3 Cos(3\alpha) + \dots \\
= & \; V(z) - \frac{1}{4}\, V''(z)\, \left(x^2 + y^2\right) + \frac{1}{64}\, V^2(z)\, \left(x^2 + y^2\right)^2 + \dots \\
& + U_1(z)\, x - \frac{1}{8} U_1''(z)\, \left(x^3 + x y^2\right) + U_3(z)\, \left(x^3 - 3 x y^2\right) + \dots \\
& + W_1(z)\, y - \frac{1}{8} W_1''(z)\, \left(y^3 + y x^2\right) + W_3(z)\, \left(y^3 - 3 y x^2\right) + \dots
\end{aligned} \tag{2.50}$$

U_1 and W_1 are FHFD used in trajectory equation, Equation (2.47). An analytical solution for trajectory depends on these two terms.

$$\begin{aligned}
x(z) = & x_0\, g(z) + x_0'\, h(z) + x_p(z) \\
y(z) = & y_0\, g(z) + y_0'\, h(z) + y_p(z)
\end{aligned} \tag{2.51}$$

where g and h are two principal paraxial trajectory with initial condition given in Equation (2.22). x_p is the particular trajectory solution to FHFD functions.

$$\begin{aligned} x_p(Z_o) =& x_p'(Z_o) = 0 \\ y_p(Z_o) =& y_p'(Z_o) = 0 \end{aligned} \tag{2.52}$$

$$\begin{aligned} x_p(z) =& \frac{h(z)}{\sqrt{V(Z_o)}} \int_{Z_o}^{Z_i} \sqrt{V(\xi)}\, \frac{U_1(\xi)}{2V(\xi)}\, g(\xi)\, d\xi \\ & - \frac{g(z)}{\sqrt{V(Z_o)}} \int_{Z_o}^{Z_i} \sqrt{V(\xi)}\, \frac{U_1(\xi)}{2V(\xi)}\, h(\xi)\, d\xi \end{aligned}$$

$$\begin{aligned} y_p(z) =& \frac{h(z)}{\sqrt{V(Z_o)}} \int_{Z_o}^{Z_i} \sqrt{V(\xi)}\, \frac{W_1(\xi)}{2V(\xi)}\, g(\xi)\, d\xi \\ & - \frac{g(z)}{\sqrt{V(Z_o)}} \int_{Z_o}^{Z_i} \sqrt{V(\xi)}\, \frac{W_1(\xi)}{2V(\xi)}\, h(\xi)\, d\xi \end{aligned} \tag{2.53}$$

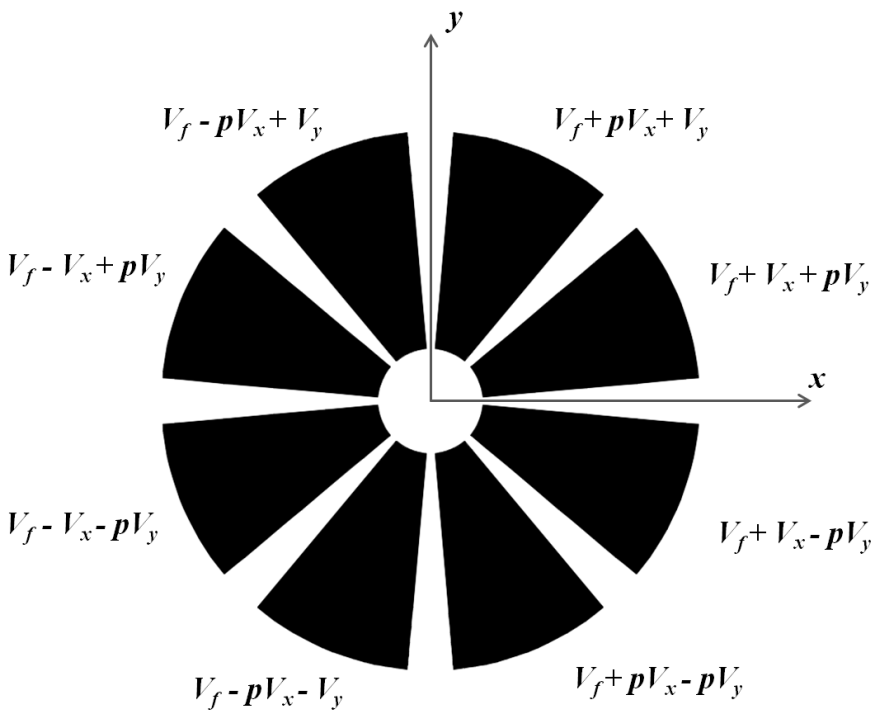

Figure 2.22: Voltage map on a focusing and deflecting octupole lens

Providing that the geometry of the deflector and field boundary conditions are chosen to eliminate the higher harmonic field distribution, a uniform deflector field is obtained and the geometrical aberration is minimized. Here is one of the deflector designs for x and y deflection in the shape of a planar octupole lens. V_f is actually the focusing axisymmetric potential and V_x and V_y are deflecting potentials in the x and y directions.

For this configuration, the Fourier coefficients in expansion series, Equation (2.48), define the FHFD functions, U_1 and W_1 in terms of p and design parameter ε.

$$U_1 = \frac{4V_x}{\pi R}\ J_0(\varepsilon)\ \frac{(\sqrt{2}-1)p+1}{\sqrt{2}}$$
$$W_1 = \frac{4V_y}{\pi R}\ J_0(\varepsilon)\ \frac{(\sqrt{2}-1)p+1}{\sqrt{2}} \tag{2.54}$$

It can be easily seen that for $p = \sqrt{2}-1$, third and fifth harmonic functions are canceled, and thus a uniform deflection field is derived for a series of planar octupole lenses. Here, the effect of deflection field on the droplet's trajectory is illustrated in Figure 2.23. The octupole deflecting field is superimposed on the axisymmetric lens field (discussed in 2.3). Figure 2.23 shows how a stronger deflecting field affects the trajectory and enables the focusing-deflecting lens to scan a larger area on the target.

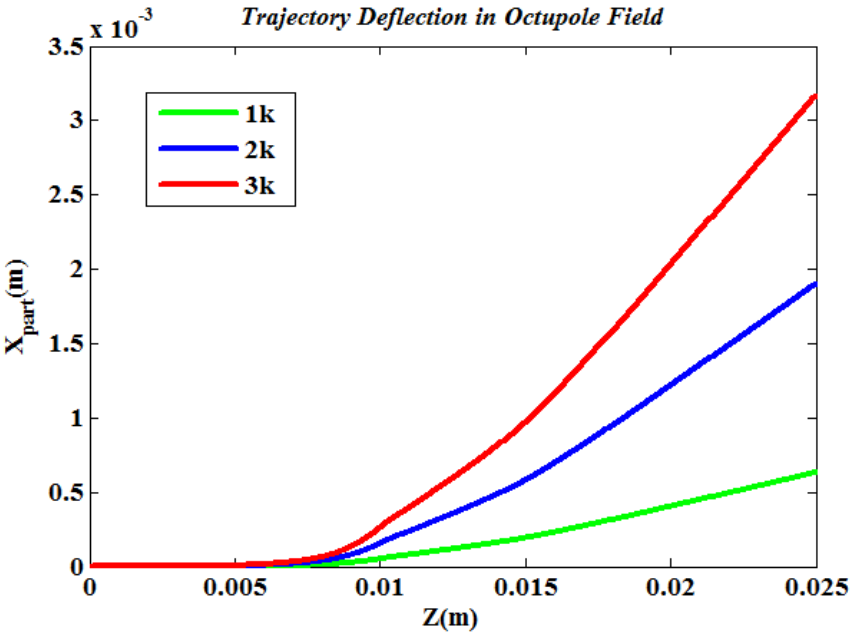

(a)

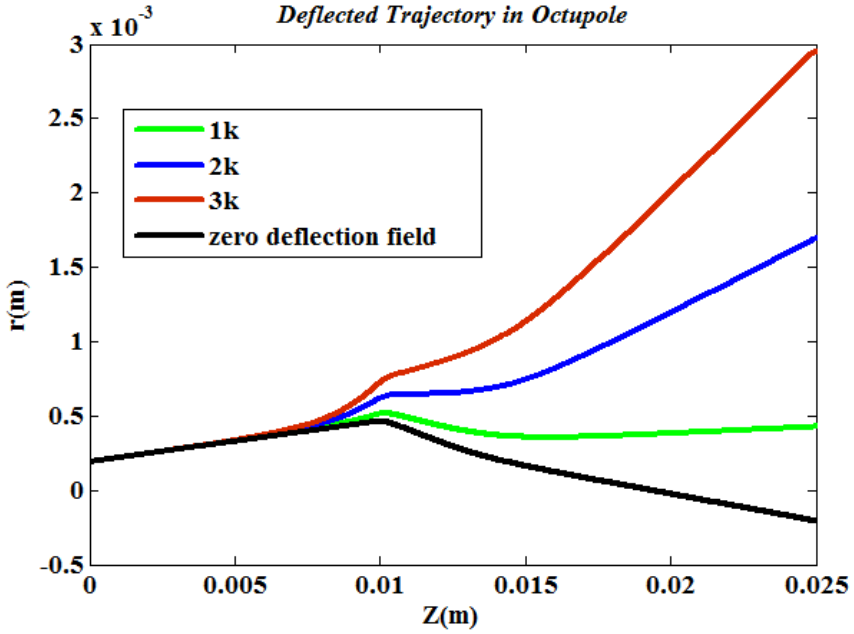

(b)

Figure 2.23: particular trajectory(a) and deflected trajectory(b) solutions in deflector field .

Chapter 3

Focused Electrospray Beam Column: Experimental Methods

A high voltage experiment set up was designed to operate in vacuum. In this setting, a jet of the ionic liquid is extracted from the reservoir when the voltage difference in the order of a few kV is applied on the extractor. A Taylor cone jet is formed when the viscous and electrostatic forces maintain the balance on the charged jet outer surface. The jet breaks up into the nano/micro spray of droplets after a transition happens from the cone jet to jet. Skimmer is an aperture electrode which is held at extractor potential. The beam angle is defined by skimmer electrode in zero electric field after jet breakup and forming spray beam. The beam is then focused in the electrostatic lens unit. An Einzel lens of three electrodes is considered to focus the coaxial electrospray beam.

In order to achieve the best alignment and astigmatism correction in practice, multiple focusing, deflection, and filtering can be used in series. A conceptual design of the Focused Electrospray Beam was considered as shown in Figure 2.3. In this design, the coaxial planar

elements with low tolerance in alignment are desired to deform the paraxial beam. Higher tolerance in the fabrication and assembly results in higher geometric aberrations. This thesis mainly includes the experimental study of one stage focusing of the ES beam at the Gaussian image of the sprayed beam source. The setup includes ES source, Extractor, Skimmer and Lens Electrodes. Two fabrication approaches were used for both conductors and insulator elements of the setup; Microfabrication and Macromachining. Microfabrication techniques offer more precision in fabrication and assembly of the electrodes. However, it is an expensive and time consuming method and needs an extensive amount of user training. Conventional machining on the other hand is not as precise, but much cheaper in terms of equipment and labor work. Next section discusses a focusing device, designed and fabricated using microfabrication techniques. The proposed device was successfully fabricated and tested in vacuum chamber. Because repeating the fabrication process was time consuming and expensive the alternative approach was preferred for the continuation of the project.

3.1 Experiment I: Microfabrication Approach

A few criteria have been prioritized in design and implementation of the focused ES beam column. This factors were decided based on the desired performance and the operation conditions. In addition to the required precision in fabrication and alignment of the E-field defining elements, the column should be assembled such that the voltage break out between adjacent parts happens in voltage difference around or higher than $20kV$. This specification makes the microfabrication techniques the best approach. It minimizes the fabrication error down to few microns. The other advantage of microfabrication approach is to minimize the post-fabrication assembly steps, i.e. lens electrodes are permanently assembled and perfectly aligned. Two inch silicon wafers are chosen to be used for electrodes to be able to fit into

the available vacuum chamber. The space between electrodes is to be filled with a dielectric material of high voltage breakdown strength; this, combined with fabrication constraints, make glass a good standoff/spacer candidate, and wafers of glass were chosen to fulfill this function.

Figure 3.1 shows a concept of the focusing apparatus with one Einzel lens focusing unit. A tube of fused silica brings the ionic liquid from the main reservoir to the emission point. Two electrodes are employed to keep the fused silica tube aligned with the axis of symmetry. The electrodes (shown in gray color) including the source alignment electrodes, the extractor, the skimmer and the lens electrodes are assembled along with a polymer insulating structure (in yellow). Two alignment bars assure the alignment of all the electrodes when assembly and will be removed after attachment is completed. Due to the importance of alignment in the electrostatic lens unit, these three electrodes are permanently bonded through the fabrication process. The polymers spacers and structure elements are machined by the conventional machining tools with the acceptable tolerance in surface flatness.

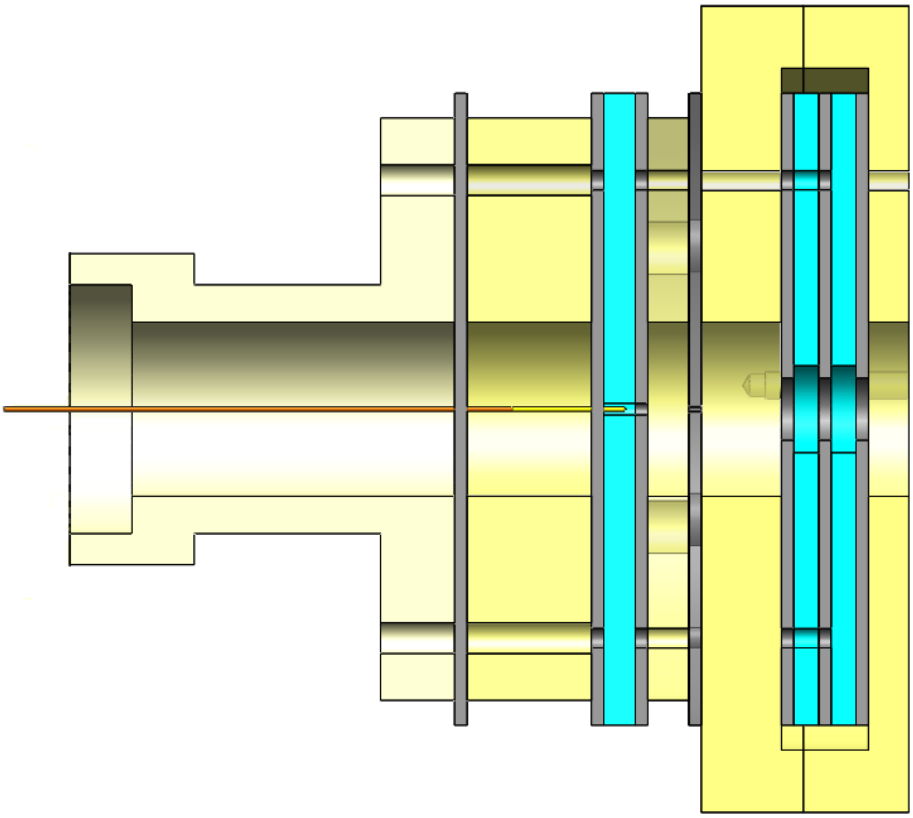

Figure 3.1: Focused electrospray beam column assembly concept I.

3.1.1 Material Selection

Polymer spacers were chosen to be made of white Delrin rods. With a good tensile and compact strength, Delrin has the temperature range of $-20 \sim 180\,^{\circ}F$. Delrin rods are available in market in 3/16" to 8" diameter. Thermal coefficient of expansion of this polymer is around $5 \times 10^{-5}\,^{\circ}F$ and the Rokwell hardness varies between M77 and M94 for different types of Delirn. Rods with diameter 1.75" and 3" provided by Mcmastercarr were machined for the required parts in the column. All the electrodes were made of silicon. Double sided polished (DSP), 2" silicon wafers with electrical resistance lower than 0.08 Ωcm and thickness of 500 ± 25 μm were used. Silicon electrodes were patterned with microfabricaiton techniques

providing a great precision in manufacturing and the advantage of alignment error less than a few micrometer. Besides the polymer spacer, glass wafers were used as the spacers where better alignment and low tolerance in the gap between electrodes are necessary. Similar to Pyrex but cheaper, Borofloat glass thermal properties is close to silicon. Boroflost wafers with a very low coefficient of thermal expansion, $3.25 \times 10^{-5}/K$, is resistant to thermal shock; and thus lets minimum mismatch when processing specially when they are bonded to silicon wafers.

3.1.2 MicroFabrication Process

The first phase of developing focus electrospray beam column includes seven electrodes. The source aligner electrode and emitter, extractor, skimmer, and three lens electrodes; the source aligner and skimmer are single silicon wafers. An orifice in the center of the electrodes are DRI etched. All three lens electrodes are also DRI etched wafers which are assumed to be the best to be bonded together before etching for better alignment and symmetry. The features including the central orifices, through holes for placing alignment bar during assembly and through holes for assembly screws where needed were printed on the soft masks. A standard lithography process has been used for patterning a thick layer, 20 μm, of positive Photoresist 4620 soft mask (See A.1). After the hard baked at 120 ℃, the 2 wafers were mounted on a 4 handle wafers and DRI etched through the wafers to have straight-wall trenches. The fabrication process for the lens unit is illustrated in Figure 3.2. Glass wafers are used as the spacers between silicon electrodes to provide the uniform spacing between the electrodes. First a stack of bonded silicon and glass wafers are fabricated (a). This stack composed of two silicon electrodes and two bonded glass wafers between them. Adhesive or direct bonding between silicon to glass wafers bonding or glass to glass wafers bonding may be used. In order to have the best alignment between lens electrodes, a permanent direct bonding is

preferred. Anodic bonding or plasma activated bonding are suitable bonding techniques for our purpose, and we chose the second one. Next, the features on both silicon wafers are etched through until reach the glass wafers (b). After two first electrodes are etched, the third electrode and glass wafers are added on top of the etched electrode stack (c). When the third electrode is DRI etched (d), the lens unit is ready for a glass wet etch to open the holes through the stack of lens unit. [79]

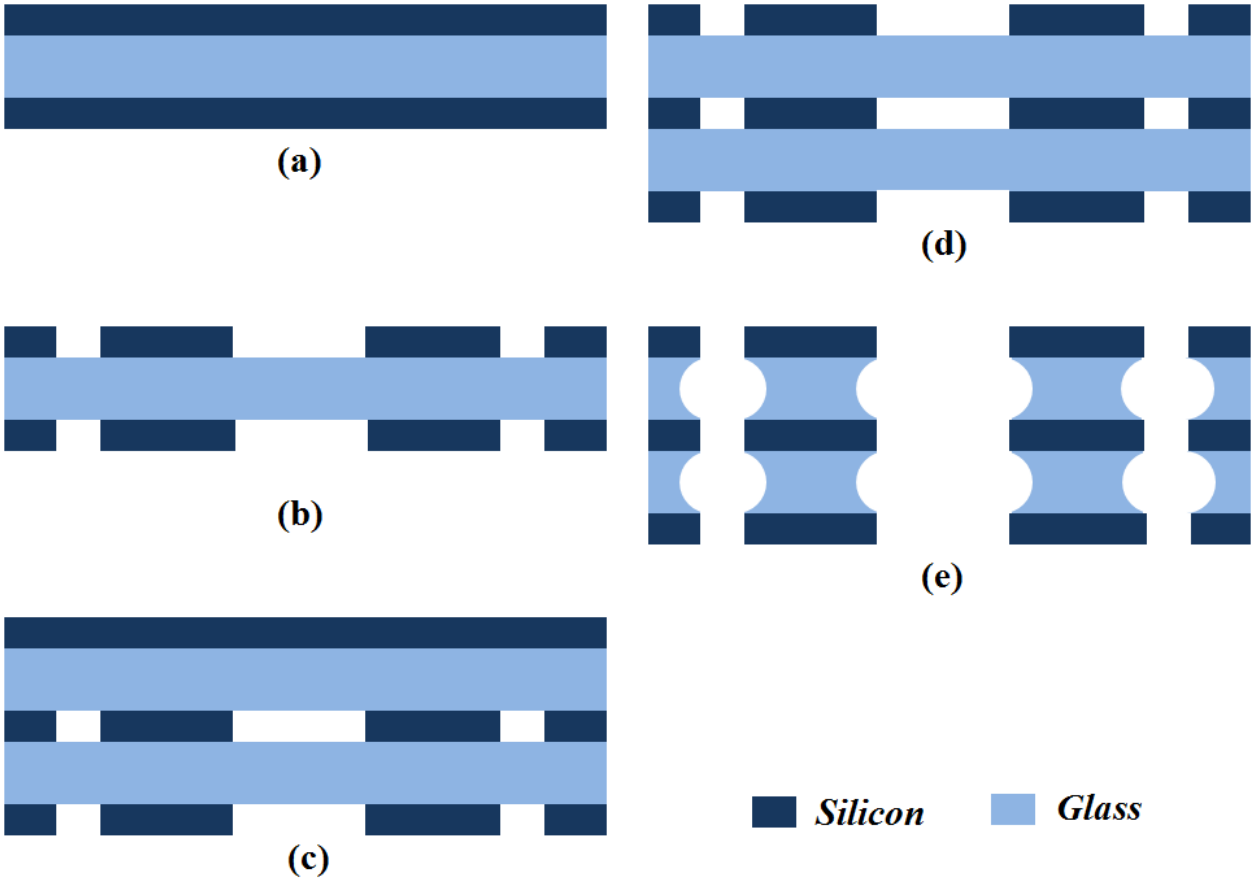

Figure 3.2: Fabrication process for electrostatic einzel lens: a) bond a stack of SoGoGoS, b) DRI etch two electrodes, c) bond SoGoG on SoGoGoS, d) DRI etch third electrode, e) wet etch glass spacers.

For the purpose of providing uniform distance and alignment between lens electrodes and possibly other components of the column, both adhesive bonding and direct bonding of

the silicon and glass wafers have been considered. [80] Three bonding methods: Adhesive Bonding, Anodic Bonding, and Plasma Activated Bonding are discussed in the following.

In adhesive bonding or glue bonding a layer of adhesive material is applied between two wafers and cured until produces a strong bond. [81] A razor blade test usually is used to verify the strength of the bond. In developing MEMS devices, a variety of UV sensitive materials are commonly used as the intermediate layer in adhesive bonding technology. SU-8 and Benzocyclobutene(BCB) are two examples of such materials.

In this research, Polyimide (Microsystem HD 4110) was used to experiment the adhesive bonding. Polyimide is a good insulator with a high cure temperature around 400 which can be spun coated on the substrate with a uniform thickness. High cure temperature and low outgassing makes it a good choice for the bonded device which is going to be placed in the vacuum chamber. The bonding process was performed successfully according to process in A.2. The bonding quality was verified by razor blade test.

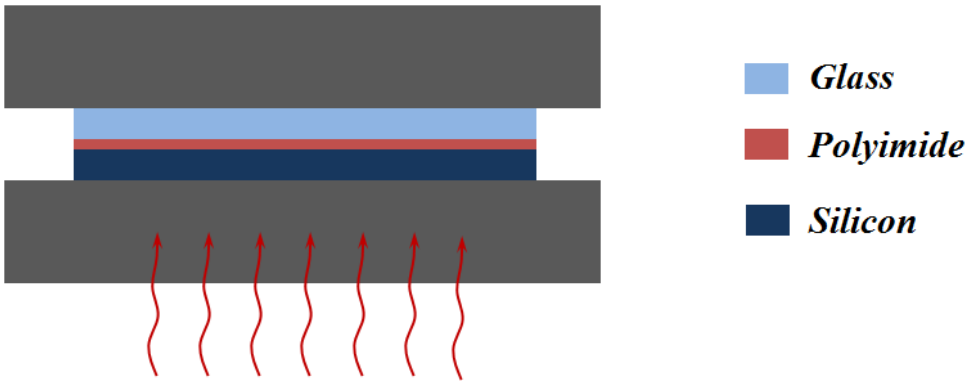

Figure 3.3: Adhesive bonding between two wafers; an intermediate coating layer is cured while a uniform load is applied.

In spite of the ease of using adhesive bonding, it is decided to not use it in fabricating the lens unit. Since further processing such as soaking in acid is not compatible with the adhesive coating, the glass wafers should be etched through before bonded to silicon wafers.

On the other hand, because the thickness of the intermediate layer may change with the applied pressure during soft bake and cure, the consistency of the thickness and thus the gap between electrodes is not guaranteed.

Anodic bonding or plasma activated bonding are suitable bonding techniques for permanent attachment of wafers. Anodic bonding is widely used for hermetic packaging in MEMS industry. It is a better option for bonding substrates with higher surface roughness. This method of bonding works best for Borosilicate glass such as Pyrex with close coefficient of thermal expansion to silicon. After cleaning and surface activation, a primary atomic bond is formed between the clean surfaces. The higher energy bond is formed through the electric field at high temperature and under uniform compression. Even though glass is considered an electrical insulator, during four-hour annealing a thermo-compression process at high voltage (up to 1000 V) and high temperature 400 ℃ increases the mobility of ions. Diffusion of Na^+ or H^+ ions out of the depletion zone and reacting with the humidity produces negatively charged glass (NaO_2) and O^{2-} ions which travel toward silicon wafer or anode and form glass (Si_2O). [82]

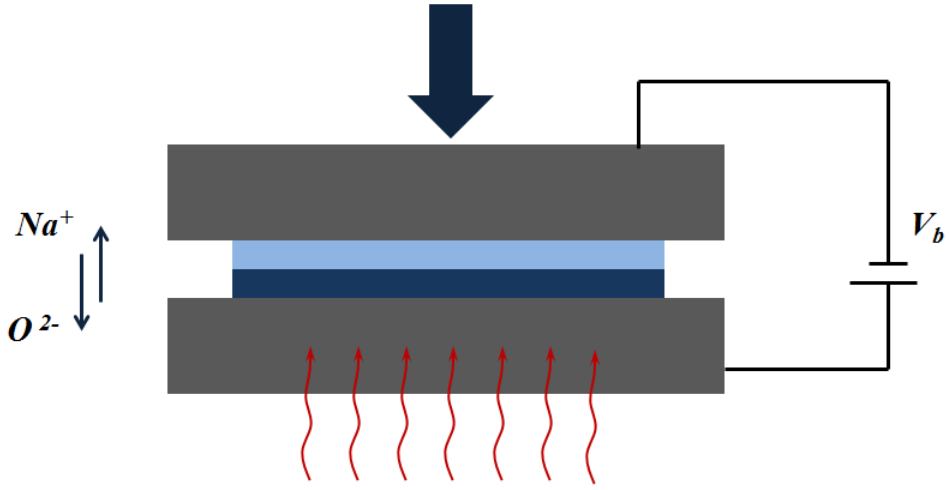

Figure 3.4: Anodic bonding; permanent bonding of glass to silicon wafers through electric field.

Plasma activated bonding in atmosphere pressure is an effective approach for bonding clean wafers. [83] Providing that surface roughness is low enough to form primary atomic bonding on plasma treated surfaces. As opposed to anodic bonding, no electric field or external pressure is needed during annealing; which makes it a good substitution for anodic bonding when multiple-stage bonding is desired. In plasma activation after a solvent rinse, wafers are cleaned by a standard RCA1 process followed by DI water rinse. In addition to removing organic contaminations, RCA1 leads to a hydrophobic surface with elevated amount of $Si-OH$ groups (Refer to A.3 for RCA1 standard process). An oxygen plasma treatment is done to activate the meeting surfaces on both wafers to increase $Si-OH$ bonds. After plasma activation, samples are soaked in the DI water to provide enough OH groups by bonding with water. After nitrogen blow drying, a temporary bond is formed by pressing the wafers against each other. At this point wafer surfaces come to atomic contact and $Si-OH$ groups combine and form glass (Si_2O) in room temperature. High energy bond is formed when bonded wafers are annealed at 200℃, for four hours when produced water is also diffused.

$$2SiOH \rightarrow Si_2O + H_2O \tag{3.1}$$

For both abovementioned direct bonding methods cleaning the wafer is a critical step. Any contamination or particle on the bonding surfaces results in voids, and thus unbounded area which can be avoided by proper cleaning and handling. Newton rings appear around the existing particle where the bonding energy (Van der Waals force) is much lower than the perfectly bonded area.

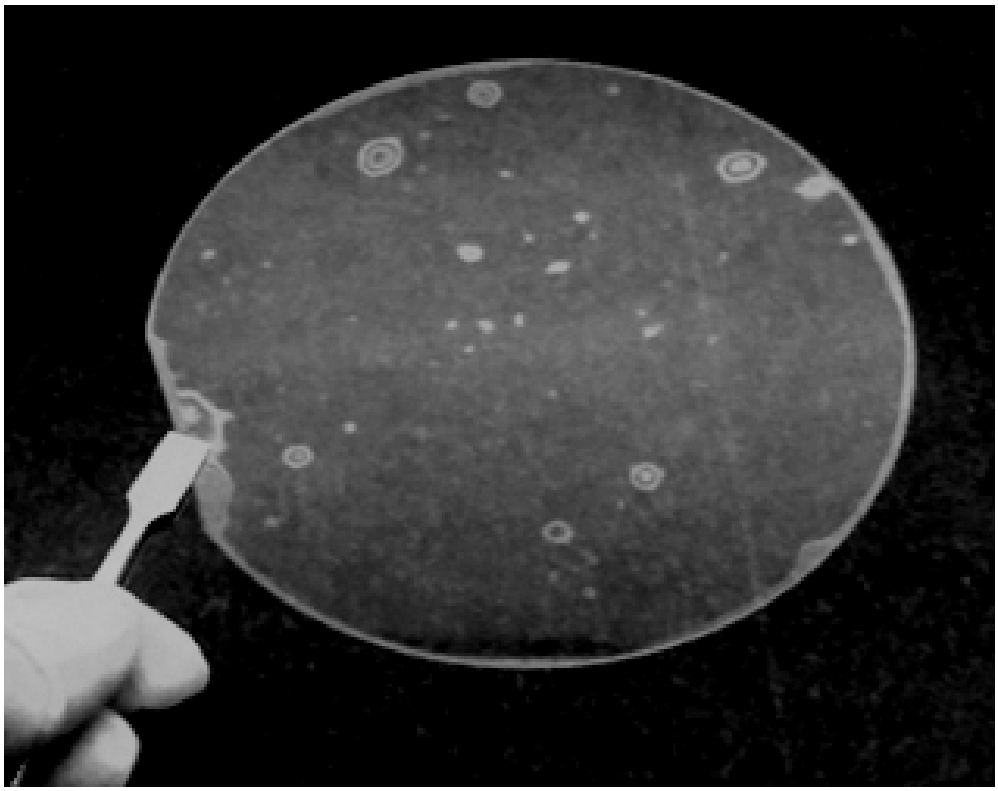

Figure 3.5: Bonded 4 glass to glass wafers using plasma activated bonding; Newton rings are seen and small voids are seen.

More promising results were achieved with Plasma activated bondig among trial runs for three above approaches. So it was used in the lens fabrication where silicon to glass wafers and glass to glass bonded wafers were needed in this research.

A sequential process of the lens fabrication is seen in Figure 3.6. The process starts with plasma activated bonding glass wafers to silicon using the recipe in A.4. Figure 3.5 shows one of the bonded SoG sandwiches. Small ring over the edge remain unbonded due to beveled edge of glass wafer. Another 500 μm glass wafer and a silicon wafer are bonded using the same technique on top of the SoG stack to create SoGoGoG sandwich as shown in Figure 3.6(b).

Positive photoresist AZ4620 is used as a soft mask for silicon DRI etch (See A.1 for DRI etch recipe.) The exposure of the AZ PR is performed in ultraviolet exposure tool MA6 with backside alignment capability. The main challenge during the front and back side etch of the SoGoGoS sandwich is overheating in STS chamber which may cause cracks in the bonded stack of silicon and glass wafers. Also protecting the backside of the stack during DRI etching is very important since both lens electrodes are to be as clean as possible for further bonding and also for better performance of the Einzel lens. A double sided conductive thermal tape by NITTO DENKO with the release temperature around 150 ℃ was used to attach the stack to the handle wafer. Not only it protects the backside silicon wafer, but also it provides heat conduction for better cooling during etching. All the DRI etching processes have been done in 10 to 20 minutes interval to avoid overheating and crack in bonded wafers on etching rate of 3 $\mu m/min$. Decomposition of the adhesive material nominally happens at 150 ℃. The sample was heated up to 170 ℃ on hotplate for 1 minutes and tape was removed. The surface was observed clean with minimum residue and minimum post-etch cleaning process.

When the first electrode is etched, the lithography on the second and third electrode is done while the mask features are matched with the etched features.

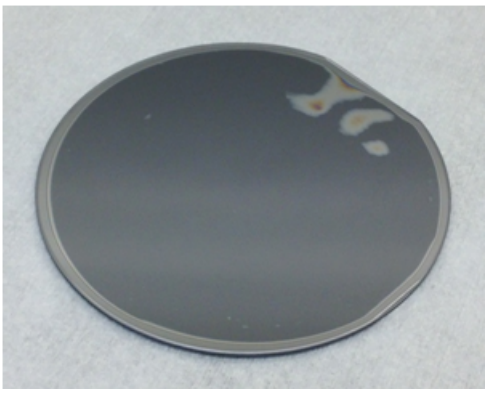

(a)

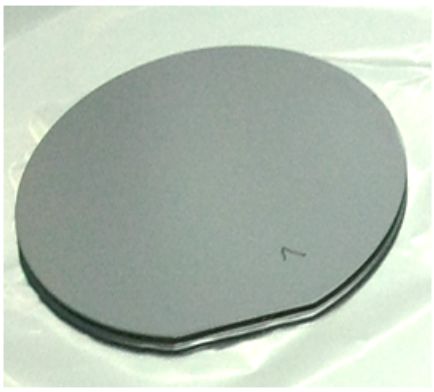

(b)

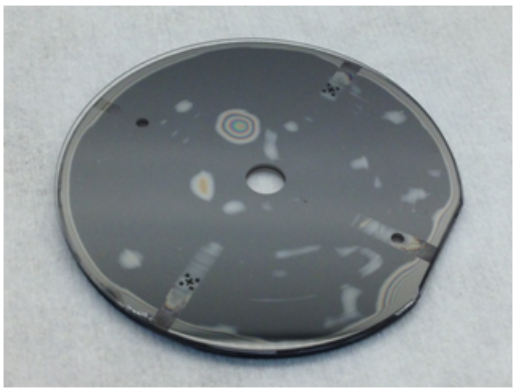

(c)

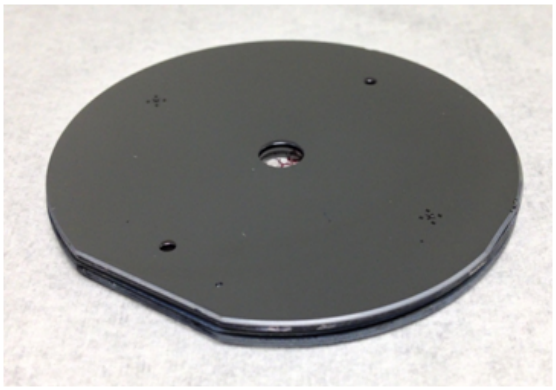

(d)

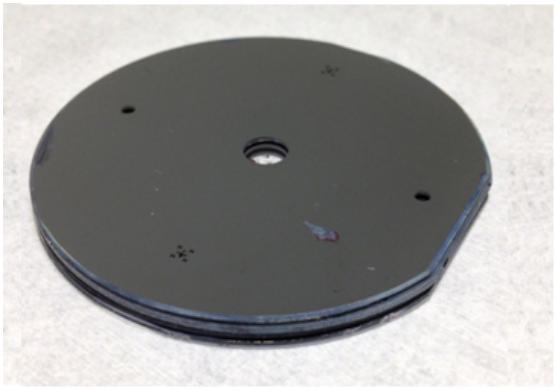

(e)

Figure 3.6: Microfabrication process of lens unit featuring three etched electrodes.

In Figure 3.6(a) another example of good glass to silicon bonding is seen for bonding

glass wafer to the process SoGoGoS stack of wafers. Despite the fact that the SoGoGoS stack was already gone through a long etching process. Notice the very few Newton rings in Figure 3.6(c). Although, proper handling and cleaning processes decreases the unbonded area and Newton rings, small residues of PR masks or trapped air are inevitable may cause small defects as opposed to the perfect bonding in first picture. In any case, these small defects do not compromise the structure. When observed through the optical profilometer, the alignment of the etched feature on three electrodes in the lens stack is verified. When all three electrodes were etched, the lens unit was exposed to %48 HF to dissolve glass wafers in the area that are exposed during the DRI etch. A mixed solution of %48 HF and HCl (10:1) was used to achieve higher etch rate of 8 $\mu m/min$. [84] A final step of Piranha cleaning was used before using the fabricated device in the column assembly.

(a) (b)

Figure 3.7: Side view of the microfabriated lens unit with etched electrode before wet etch (a) and after glass wet etch (b).

An optical profilometry on the lens aperture shows the alignment between three lens is within expected accuracy range of the process.

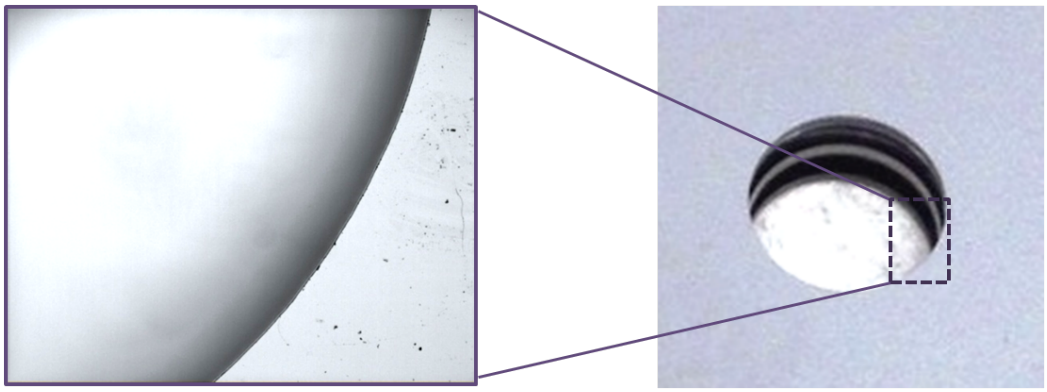

Figure 3.8: Closup at the lens apreture after glass etch.

The extractor electrode is also bonded to one of the source aligner electrodes with glass spacers. The fabrication process is similar to the lens. The etched SoGoGoS stack of extractor and source aligner electrodes before glass wet etch is seen in Figure 3.9. The big grove provides optical access to observe the electrospray emitter while testing. Other elements in the proposed focused electrospray column are single electrodes; which are etched through in DRI etching process.

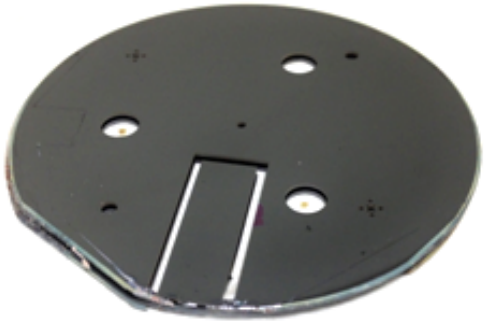

Figure 3.9: Extractor and source aligner electrode in one stack.

A SoGoGoS bonded prototype made of 4" wafers was tested in vacuum. The voltage difference between two silicon electrode was increased gradually up to $22kV$ without any spark or voltage breakdown between electrodes. This voltage is higher than needed in electrospray

focusing apparatus. The fact that we were able to sustain such a high voltage difference supports the choice of materials for the column.

Here is shown an assembled set of focusing electrodes to be tested in vacuum with an EMI-Im electrospray source (Figure 3.10). From left, the lens electrodes fixed between two Delrin panels, skimmer electrode, bonded extractor and second source aligner electrode, and first source aligner electrode are aligned with two aligner rods and held in place with a set of through screws. The needle tip is fixed at 0.5 mm from extractor electrode to grantee the spray formation. The desired voltages are applied on each individual electrode when mounted in vacuum chamber.

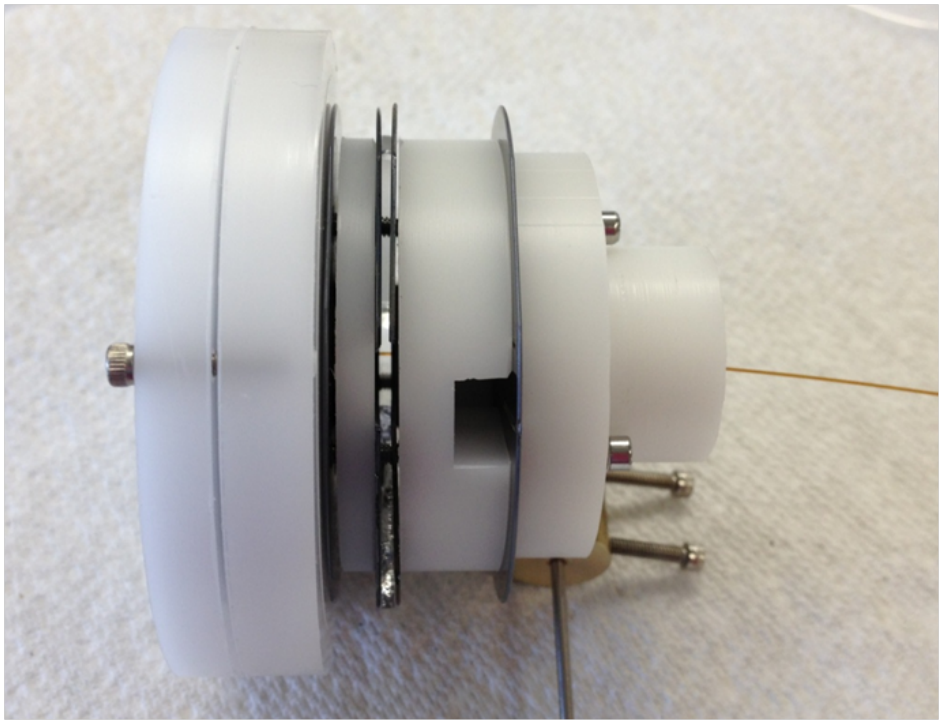

Figure 3.10: Assembled focusing electrodes.

3.2 Experiment II: Machining Method

The design of the focused electrospray column was slightly modified for machined part. The concept of the accelerating and focusing elements are the same as shown in Figure 3.1. One of the main differences between two approaches is the accuracy of fabrication. Higher manufacturing tolerances in machined parts may affect the axisymmetric assumptions. Because minimum offset from axis is desired for source to avoid offset aberrations,an external alignment mechanism was integrated in the design to be able to adjust the position of the needle in two directions.

The focusing electrodes are made of brass, and the gaps between electrodes are filled with 1 mm glass wafers. The needle (fused Silica tube)is fixed and carried through a source aligner part which is assembled inside the flange. Miniature micrometer heads, Mitutoyo 148-218 (range $0 - 0.2$", and graduation 0.001", and nominal accuracy ± 0.005 mm), were used for positioning the needle after assembly in X and Y directions. A ball thrust mechanism was used between the flange and source aligner to assure the tip of needle (source) stays on a paraxail direction to lens axis during the experiment. In this set up, the source is located $1mm$ far from the extractor. Figure 3.11 illustrates a cross section of this design. Alignment between electrodes and other elements are defined with 1/16" alignment rods.

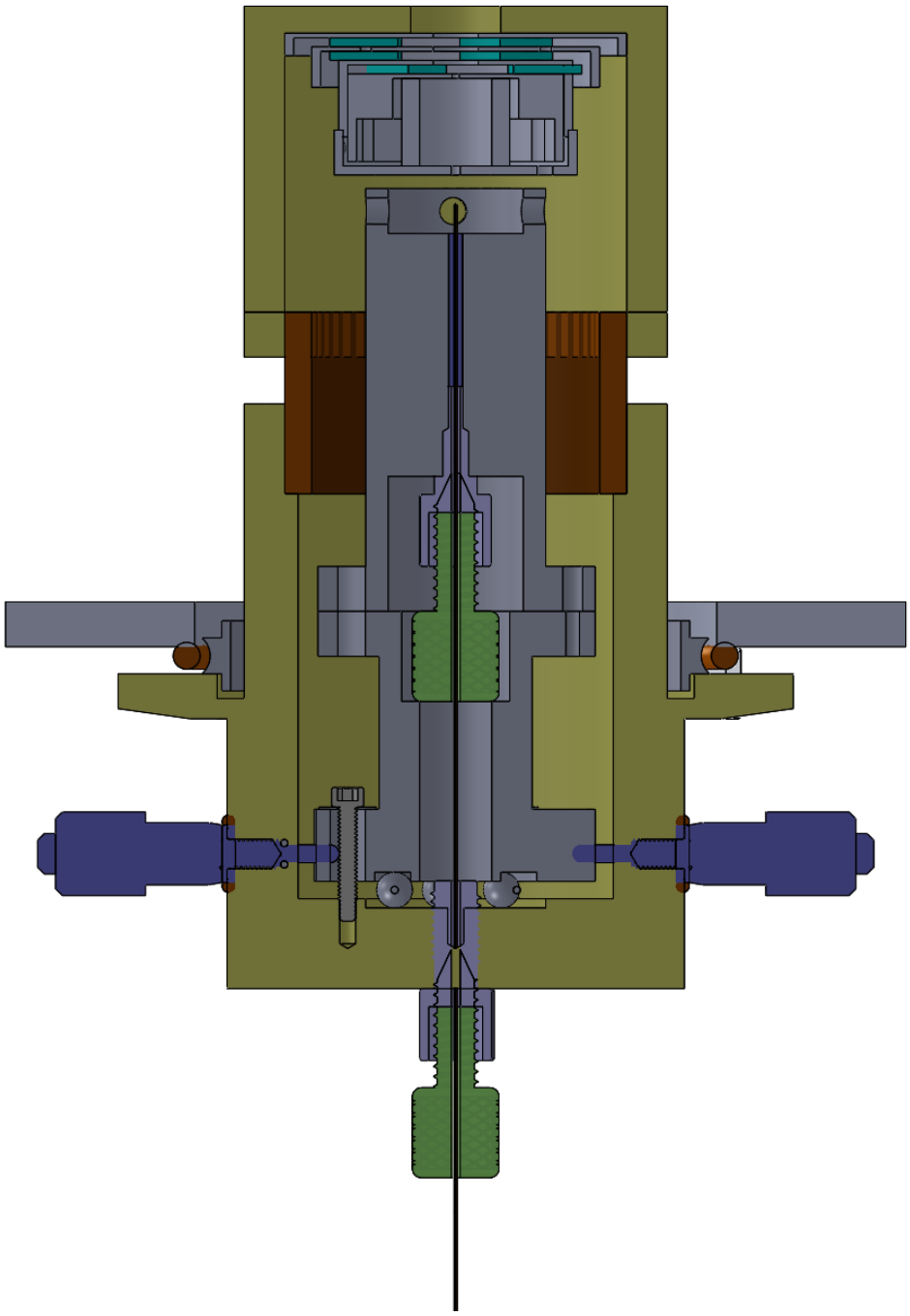

Figure 3.11: Focused electrospray beam column assembly concept II.

3.2.1 Experiment Method and Discussion

The ionic liquid EMI-Im was used in all the focusing experiments. A polymer-coated fused silica tube feeds the ionic liquid from a bottle outside the vacuum chamber to the source. The tip of this tube was chamfered 45° in electric propulsion laboratory using a customized device stabilizing the tube in a mini lathe. After sharpening, about 1 in of the tube from tip was metalized by sputtering Ir for 8-10 minutes with a rate of 1 nm/min. All the tubes used in this project have inner diameter of 50 μm or 40 μm. Higher pressure inside the liquid bottle originally drives the flow to the emission tip, where the Taylor cone forms. The pressure inside vacuum chamber was stabilized at $2 \sim 3\mu$ torr) and the bottle pressure are adjusted to start and maintain the spray flow.

A target is normally a wafer of silicon on other material on ground voltage mounted on a moving stage. In this project only silicon wafers were used as a target. Three stepper motors move the target in X,Y, and Z directions and controlled externally by a Labview program. In previous chapter, the location of target, distance of image or focusing point, was calculated numerically and tabulated based on second lens voltage. The goal is to verify the image formation which represents the focusing power of the lens, and compare experimental and numerical results.

A high voltage power supply provides three separate lines of DC voltage used in focusing experiments. Two lines supply up to 20 kV and third line supplies up to 10 kV. The actual limit of the voltages that can be applied on the electrodes should be confirmed under vacuum before performing the experiment.

Next chapter discusses the results of bombardment of silicon target by focused electrospray beam.

Chapter 4

Bobmardment of silicon target by focused electrospray beam

This chapter presents the characterization of the electrospray focusing apparatus through bombardment of semiconductor targets. As discussed in introduction chapter, the accelerated projectiles are capable of damaging the surface by transferring energy during impact. The damage includes sputtering the atoms from surface in areas affected by impact and topographic changes around the impact zone specially seen as amorphization in single crystalline silicon target. [54] With a comparable sputtering yield, higher sputtering rate was reported for the electrospray nanodroplet projectiles over ion beam source for several single and poly crystalline material. [16] Given enough exposure time, accelerated electrosprayed nanodroplets can etch the material and leave visible traces. When an energetic focused beam strikes the target, a smaller traces of surface damage expected, ideally as small as size of a single droplet. The higher energy density of focused beam also helps with the higher sputtering rate on the impacted spot. This can be used to characterize the focusing process and determine the involving physical parameters. When the target located on

the Gaussian image plane, An ideal electrostatic lens system bends the trajectory of all the droplets to the same coordinates on the Gaussian image plane where target is located. It is important to know that this ideal case almost never happens primarily because of intrinsic error sources discussed in The size and shape of the damaged area on surface determines the type of aberration and quantifies these error sources such as misalignments and energy loss. In this chapter, the focusing experiment methodology for any of two focusing apparatus is explained. And the results of bombardment of silicon target by focused electrospray beam is discussed.

4.1 Electrospray and Beam Characteristics

The EMI-Im electrospray beam (from ionic liquid 1-ethyl-3-methylimidazolium bis (trifluoromethylsulfonyl) imide) used in these experiments has been characterized in vacuum. [85] The voltage drop in jet breaking zone used to calculate the chromatic aberration figure is assumed based on experimental findings independent of the emitter voltage. All the electrodes are connected to the high voltage power supply with positive polarity or ground potential when applicable. A voltage difference of 1900V between the emitter tip and the extractor electrode form the electrospray with flow of EMI-Im liquid through the capillary tip to begin. An stabilized Taylor cone under very low pressure difference continues to emit the sprayed nanodroplet from cone-tip. Below a recorded picture of a Taylor cone at the tip of metalized fused silica tube with inner diameter 50 μm.

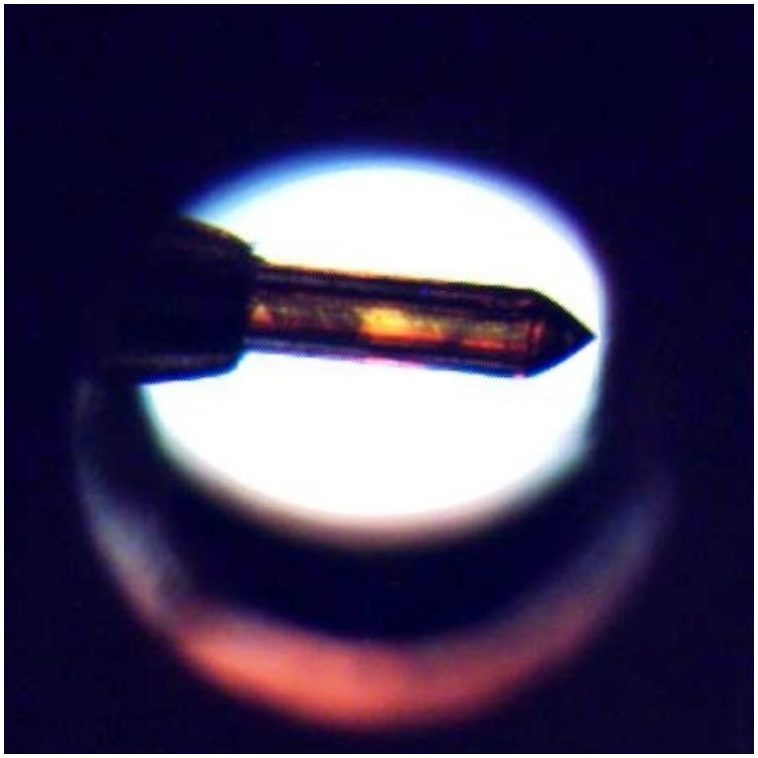

Figure 4.1: Stable Taylor Cone formed at the tip of the metalized fused silica tube.

Before elevating the electric field, the experimental setup was tested to determine the breakdown voltage for all electrodes under vacuum. The characterization stage concludes a voltage limit of 15 kV on emitter and 8 kV on second electrode. These voltage limits were measured before sprays formed. For the safety reasons the potential limits were set to a considerable lower voltages to avoid any spark in the system. The focusing experiment was performed for two emitter voltages of 12 kV and 14 kV. The voltage difference of 2 kV maintained for selected emitter voltage, V_{EM} and extractor voltage, V_{EXT} in all experiments. The skimmer and first lens electrode are on same potential as extractor. The beam is skimmed to half angle of 2 deg by design in approximately zero electric field. The middle electrode's voltage is set to a fraction of V_{EXT}, $V_2 = aV_{EXT}$. The last electrode and the target are connected to ground potential according to the schematic of experiment shown in Figure 2.3. For the 50 μm tube, a static pressure difference between the external reservoir

bottle and the chamber (driving pressure) maintained on and around 140 torr. When spray formed the voltages on all three potentials are increased gradually to reach desired voltage for the target placed at ZI. A live feed of both electrospray cone and the target under bobmardment are captured by external cameras. Here a comparison between unfocused and focused electrospray beam on target is illustrated. In this particular experiment, $V_{EM} = 12\ kV$, $V_{EX} = 10\ kV$, and $V_2 = 5\ kV$. This picture has taken while bobmardment of target. The larger, shimmery circle $1 - 2\ mm$ is where electrospray beam hit the target before increasing voltage on electrodes to focus the beam. Smaller dots on top right and lower right corner of sprayed spot are created by focused beam.

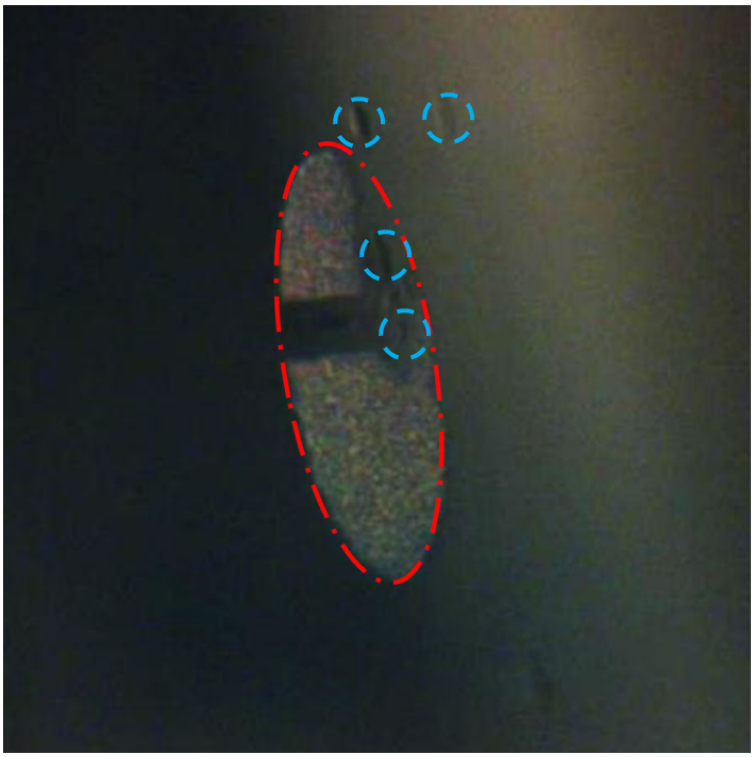

Figure 4.2: Eletrospray beam diameter compared before focusing(·····) and after focusing(- - -).

The retarding potential method determines the velocity of the particles at each point

through the lens based on the voltage at the point and the emitter voltage.

$$\frac{1}{2}mv(z)^2 + q\,V = \; = qV_{EM} \tag{4.1}$$

or

$$v(z) = \sqrt{2\,\frac{q}{m}\,(V_{EM} - V)} = \sqrt{2\,\xi\,\varphi_{RP}} \tag{4.2}$$

The charge to mass ration $\xi = q/m$ is normally determined in time of flight experiment from velocity and retarding potential:

$$\xi = \frac{1}{2\,\varphi_{RP}}\,(\frac{L_{TOF}}{TOF})^2 \tag{4.3}$$

The charge to mass ratio was characterized for EMI-Im for different values of current and mass flow of spray. In calculations showed in chapter 2 the value of $\xi = 1571$, where the jet diameter is measured 12 nm. [85] EMI-Im has a molecualr mass of 391.12 amu and density of 1520 kg/m^3. The molecular energy of projectiles in varies between 76.4 eV and 89.2 eV for accelerating voltage 12 and 14 kV commonly used for electrospray bombardment experiments here which leads to impact velocities 6.1 and 6.6 km/s. Figure 4.3 is an example of silicon target struck by the focused beam. Both experiments are performed at $V_{EM} = 12\ kV$, $V_{EXT} = 10\ kV$ and $V_2 = 5\ kV$. The image location was calculated at 21.64 mm from center of the lens. In both cases the craters formed on the impact spot. The maximum diameter of the craters for 180s and 120s are 102 and 85 μm respectively. The dark shadow on the edge of the crater shows the amorphous Si deposited on the edge. The dark and bright rings surrounding the craters show the sputtering and smoothing effect of the liquid molecules ejected from hit spot after the drops break.

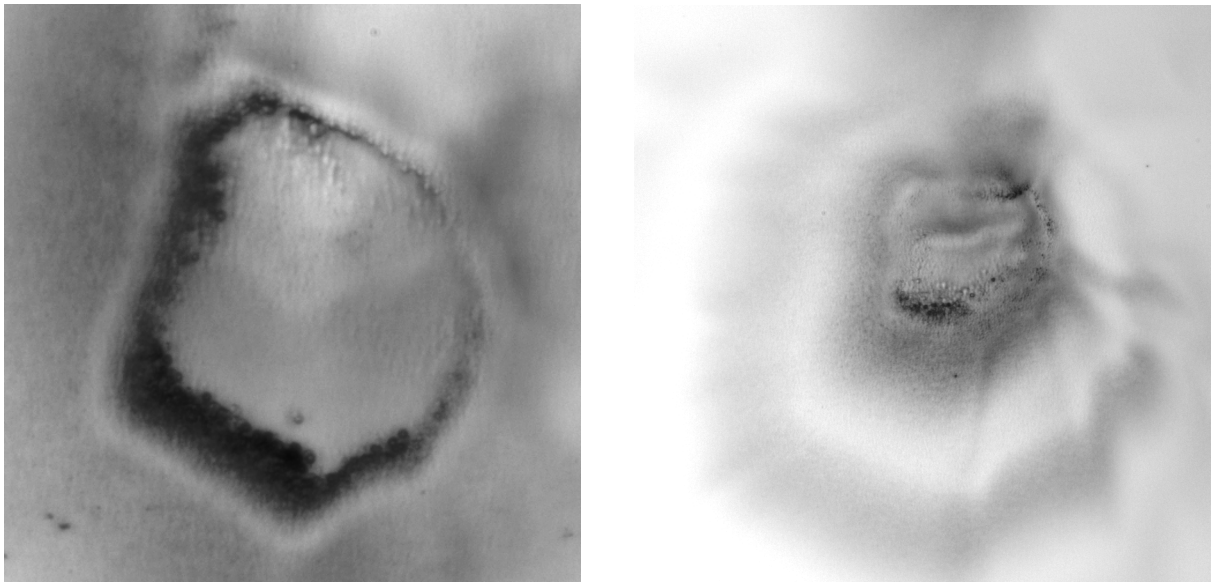

(a) (b)

Figure 4.3: Optical photos of the target bombarded by a focused electrospray beam for 180s and 120s. $V_{EM} = 12\ kV, V_2 = 5\ kV$, (a) $D_{max} = 102\ \mu m$, (b) $D_{max} = 85\ \mu m$.

4.2 Experiment I

Despite precision manufacturing, some deviation from design might be seen in final assembly of experimental setup. This affects the location of the image from center of the lens. A voltage sweep experiment for V_2 provides the accurate voltage for each image location. The smallest crater is associated with the correct image of the point source. Below a series of 20x optical images compares the focused ES beam trace on the target. In this case it is relatively easy to distinguish the effective focusing voltage from other values without accurate measurement. In addition to the size of the sputtered spot, the depth and type of damage can also help to find out the correct value of focusing voltage among all values experimented. A close examination of image at 4.7 kV, Figure 4.4(c), reveals further surface damage instead of a superficial sputtering seen as dark area here. This images are taken before the ionic liquid

was rinsed from the surface. This is particularly helpful to define the borders of the sputtered area, as well as the area that was under surface smoothing process during bombardment.

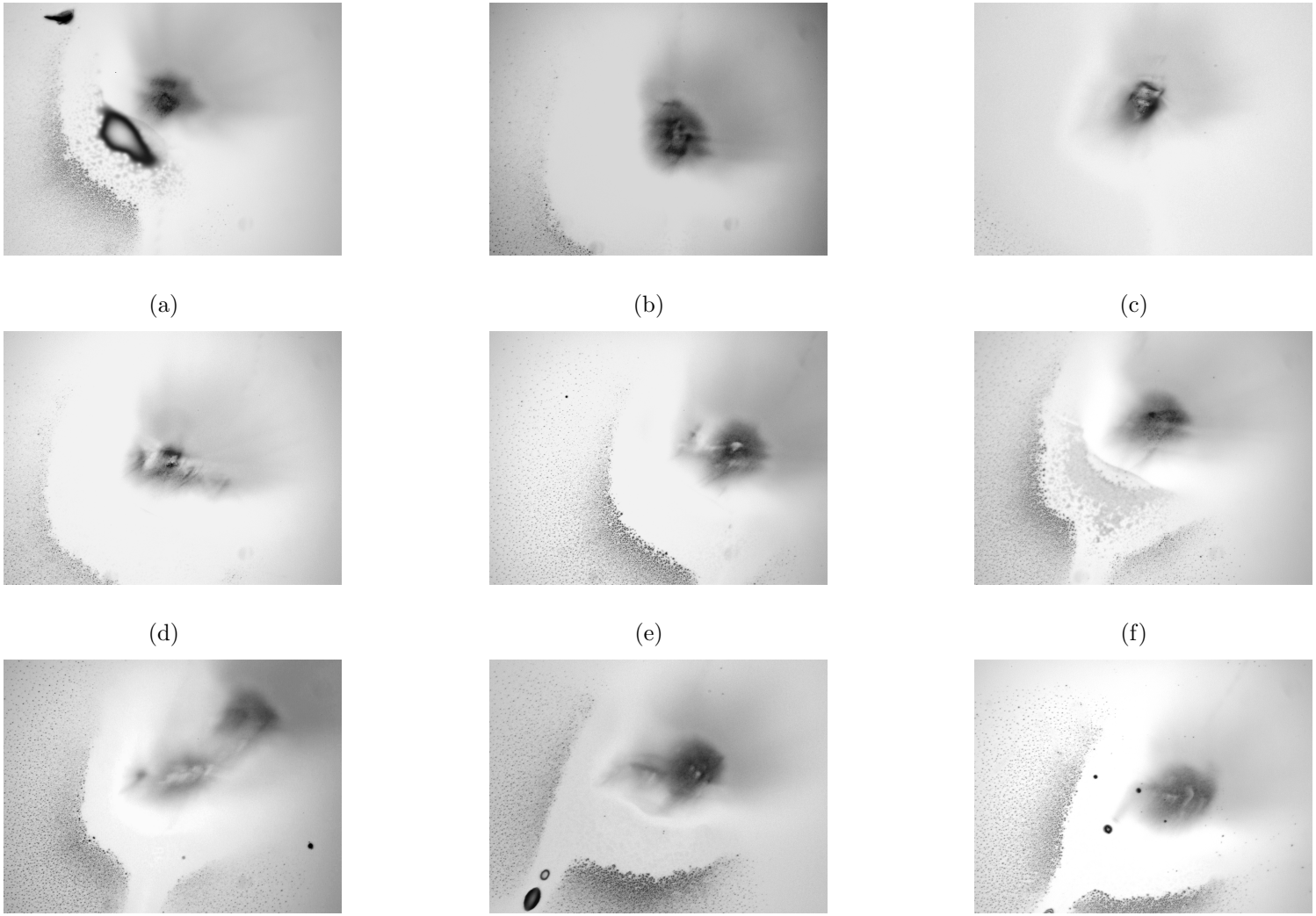

(a) (b) (c)

(d) (e) (f)

(g) (h) (i)

Figure 4.4: $V_{EM} = 12\ kV, V_2 = 4.5 \sim 5.3\ kV$, Image forms at (c): $V_2 = 4.7\ kV$.

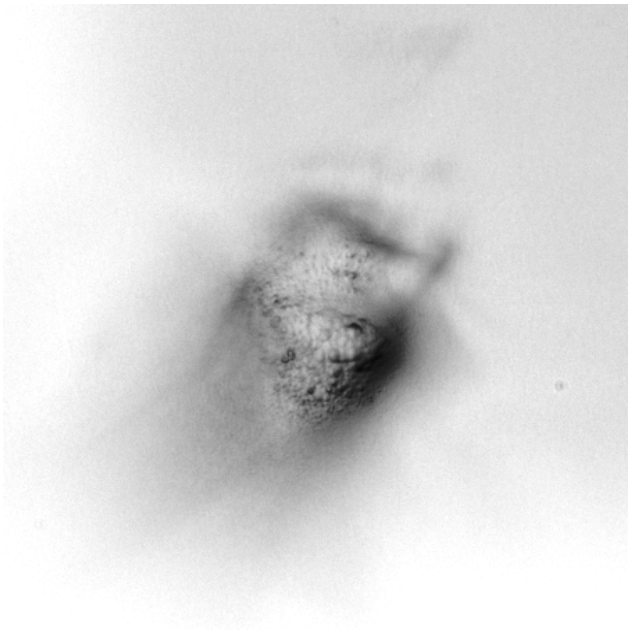

Figure 4.5: Closup view of sputtered area in Figure 4.4(c)

Figure 4.6 shows the effect of duration of exposure on the size of area under physical sputtering. Each small circle seen as dots in this image are bombarded only for 2s, and left a $3-4\ \mu m$ spot, while 30s bombardment creates a $130\ \mu m$ spot. This area is formed of two distinct region; first, the extension of the small crater where the beam is focused, second, the area seen as large dark shade around the small crater. It is concluded that in short-duration bombardment the low energy projectiles do not leave visible effect on the surface. When bombarding the target continued for 30s, a low rate sputtering made the visible trace around the originally sputtered region. Longer exposure not only increases the radius of surface changes, it also increases the depth and size of the crater. An important observation in this experiment is that the point image, where the sputtering appears to happen at highest rate, is not necessarily located at the center of the sputtered area. This phenomenon is commonly seen in other experiments performed with similar or slightly modified setting. This is less likely due to interaction between droplets and material in micro scale and angle of incident. The probable cause can be explained in terms of relative angle of the needle and

lens axis which leads to directional emission of the projectiles or an offset between source and lens axis. Another example is shown in Figure 4.7 comparing the craters created under 60s and 120s bombardment, using a 40 μm tube. V_{EM} was set to 12 kV and the image for two nominal V_2 values of 5 kV and 6 kV were inspected for exposure time 60s and 120s. The progress of the crater is vividly seen between these two cases.

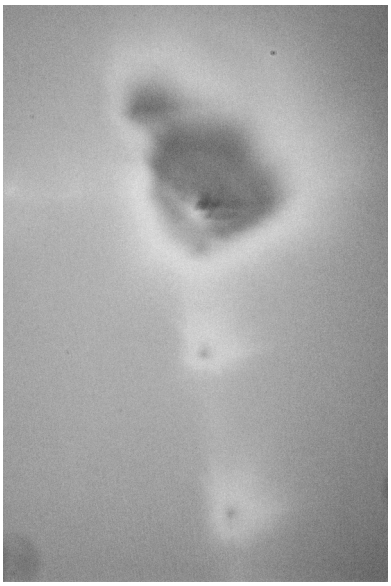

Figure 4.6: Sputtered area grow in longer exposure time, compare the smaller point images exposed only for 2s and sputtered area after 30s exposure.

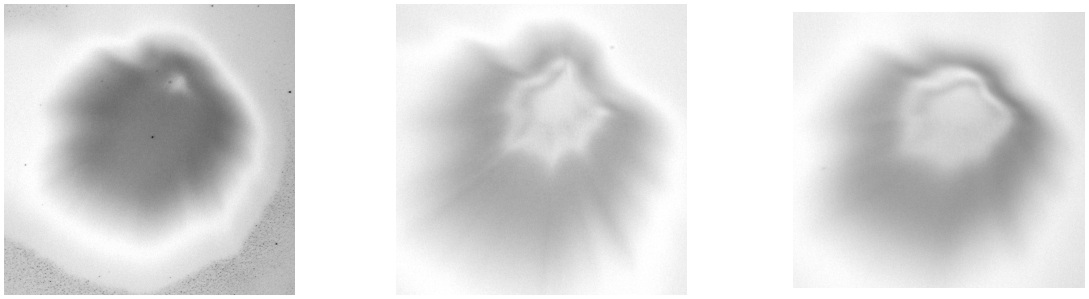

(a) (b) (c)

Figure 4.7: $V_{EM} = 12\ kV, V_{EXT} = 10\ kV$,(a) $V_2 = 5.1\ kV, a = 0.6, t = 60s, Z = 20.64\ mm$, (b) $V_2 = 5.5\ kV, a = 0.6, t = 120s, Z = 20.645\ mm$, (c) $V_2 = 4.9\ kV, a = 0.5, t = 120s, Z = 19.24\ mm$.

The retarding potential level determines the sputtering or etching rate in addition to the energy density of the beam. Higher molecular energy in charged droplets for $V_{EM} = 14\ kV$ leads to higher sputtering rate. A high rate energy transfer to the silicon atoms causes silicon melt around the striking spot and fast cooling as seen below for four different voltage values applied on lens's second electrode. In this experiment, the target was located at $ZI = 15.15\ mm$ from the center of lens. A point image for a point source should form on the target surface for $V_2 = 5.64\ kV$. The bright spot at the center shows where the beam strikes with highest intensity, encircled with a darker lava shape that become more symmetric at proper lens field, here achieve by $V_2 = 5.7\ kV$ which is very close to voltage calculated by theory. It can be concluded that projectiles impacted the surface with a much higher frequency than sputtering rate and a large portion of molten material accumulates around the impacted spot.

In order to confirm the accuracy of the focusing process, both size and shape of the craters and damages on the surface are to be investigated. In absence of all error sources, the crater diameter represents how the focusing was affected by spherical and Chromatic aberrations. Spherical aberration depends on the third order slop (γ) where projectiles are emitted from source and chromatic aberration resulted from the voltage loss during jet breakup.

$$r = \sqrt{\delta r_{s_o}^2 + \delta r_{ci1}^2} \tag{4.4}$$

Figure 4.8(c) shows the focusing voltage $V2 = 5.7\ kV$, with $D \sim 170\ \mu m$, the diameter of the bombarded spot including the blurry perimeter. The crater diameter affected by spherical aberration was calculated 138 μm which leads to the chromatic aberration figure of 40 μm, indicating a voltage drop of 119.4 V for ES beam. Here is a visual comparison between the size of damaged are with the aberration figures predicted by theory. The dotted

yellow circle at the center compares the central spot, bombarded by high intensity portion of the beam, with image size in case of 20 μm source offset. The dotted red circle indicates the spherical aberration disk and green circle represents the chromatic aberration disk, 40 μm. This two are combined to form the full image including high resolution and blurry area measured on an optical image of the affected area.

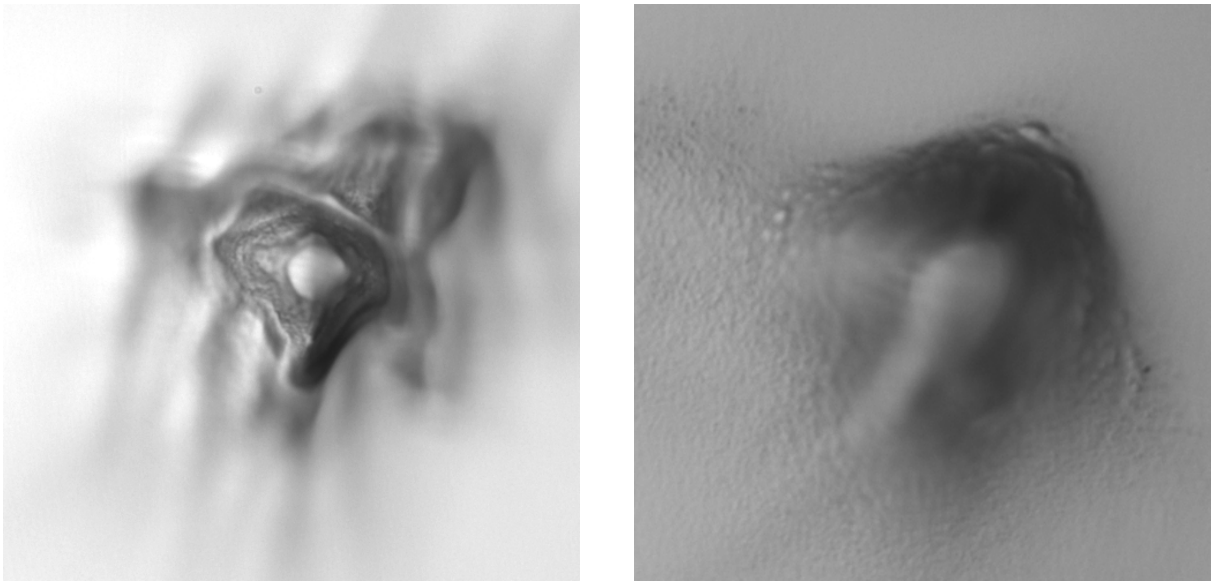

(a)

(b)

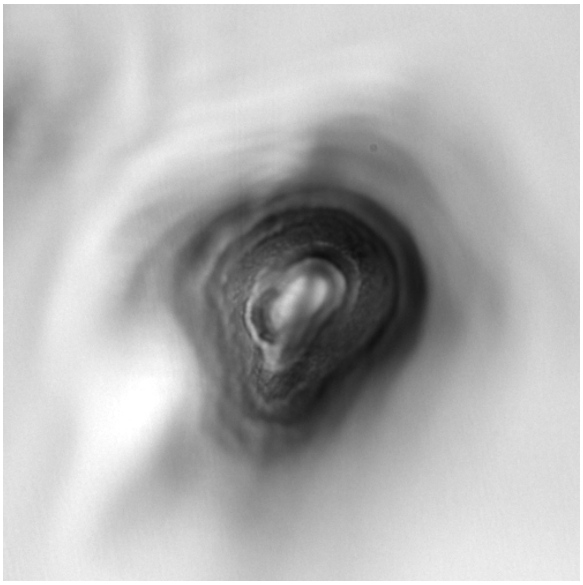

(c)

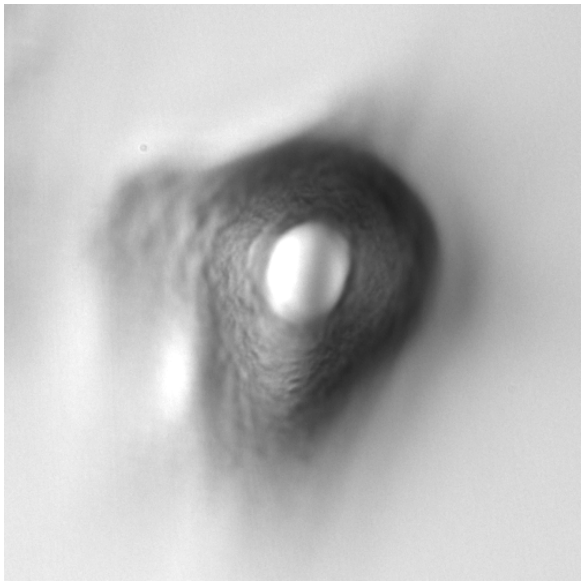

(d)

Figure 4.8: $V_{EM} = 14\ kV, a = 0.5, t = 60s, Z = 15.17\ mm$, (a) $V_2 = 5.4\ kV, D = 7\ \mu m$,(b) $V_2 = 5.6\ kV, D = 9\ \mu m$, (c) $V_2 = 5.7\ kV, D = 4\ \mu m, (d) V_2 = 5.8\ kV, D = 10\ \mu m$.

As seen in chapter 2, the contribution of Astigmatism figure is much smaller than spherical and chromatic aberration figures in final image. For instance, in this experiment the

numerical simulation shows that a 20 μm offset from lens axis leads to a 190 nm increase in image dimensions. This does not indicate that astigmatism is not detected in the image. On the contrary, astigmatism as well as field curvature result in a distorted image. In presence of astigmatism, the image at the Gaussian image is a circle. The astigmatic image under field curvature becomes an ellipse at the Gaussian image and two perpendicular lines form on the planes before and after the Gaussian image plane. The sputtered or deposited features in this experiment do not show signs of distorted image caused by varying magnification of lens with radial distance from lens axis.

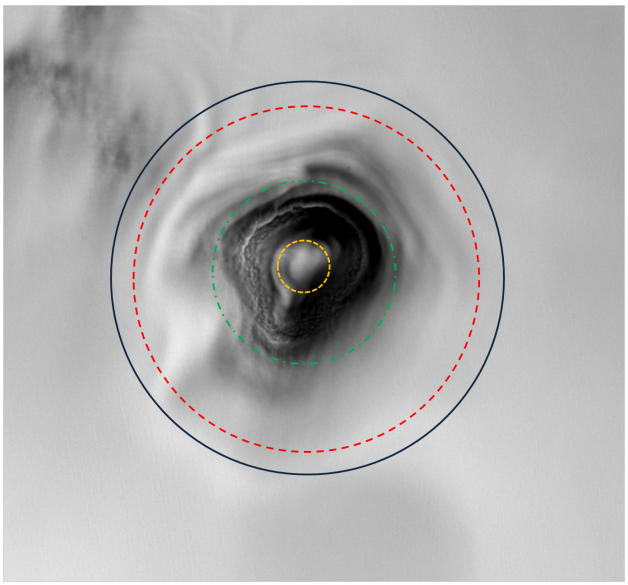

Figure 4.9: Contribution of spherical aberration(- - -) and chromatic aberration (- - -) in size of sputtered area(——) for one point bombardment.

4.3 Experiment II

The next experiment was performed to compare the effect of the electrostatic lens power on the overall size of the image spot at $V_{EM} = 12\ kV$. The experiment was repeated for three values of a=0.4, 0.5, and 0.6. In each step the target was located on the corresponding

image location and potential on second electrode changed within 2 kV around the nominal value of $(0.4 - 0.6)$ V_{EXT} and bombarded for t=180s. At $V_2 = 3.5$ and 3.7 kV, the energy of the beam is consumed for surface transition to an amorphized phase and re-depositing the molten material. At $V_2 = 3.9$ kV sputtering process started to happen. The optical and SEM images of the bombarded spots for a=0.4 are shown in Figure 4.10 to 4.16 confirm the focusing voltage of $V_2 = 3.9$ kV leading to a 90×63 μm area of exposure on target. This area is where the beam had the most intensity seen in the optical image. The affected area on the surface is a 310×265 μm ellipse which is visible on the SEM images. The surface smoothing process most likely occurred in this region due to low energy of the projectiles with trajectories deviated from focused rays. As voltage increased to 5 kV, the sputtered pattern remained more or less similar. For voltages above 5 kV, the aspect ratio of the sputtered spot increases and the star shaped feature becomes closer to a line, indicating the presence of astigmatism away from the image plane. The contribution of spherical aberration on the sputtered spot size only depends on the beam half angle defined by design and not the source offset. Its part can be separated from the overall size of the bombarded spot from the part added from other sources. The bombarded area investigated here have a distinct shape that indicates other existing sources of aberration. The sputtered area appears in the shape of star or pincushion with shape corners and general shape of the smooth surface is deviated from a symmetric disk to an oval shape. The cushion shape indicates distortion in the image resulted by the magnification factor shift with radial distance from lens axis, and ellipse can be an indication of the source offset that led to coma. The oval shape can be a result of astigmatism combined with field curvature as well. However, for any misalignment these two aberration figure are much smaller than coma figure. On the other hand, coma implies a larger misalignments than what can be seen as astigmatism on image plane. In addition to spot size, this spot is closest to a circle shape. The center of image is shifted $2\delta r_{coma} = 45$ μm, leading to the fact that there is an offset of 13.5 μm between the electrospray source and

lens axis. Assuming this is the only misalignment in the focusing column, the rest of the aberrations figure, associated with 13.5 μm misalignment, are as seen in Table (4.1).

Table 4.1: Aberration figures for $V_2 = 3.9\ kV$ for 13.5 μm source offset.

V_2	Spherical Aberration	Astigmatism	Curvature of Field	Distortion
kV	µm	µm	µm	µm
3.9	84	0.12	63e-3	0.69

The chromatic aberration figure is the last contributing factor on the image size and it can be derived from deducting the combination of other figures from measured radius of sputtered spot. The chromatic figure turns out to be 100 μm leading to a value of 242V for voltage drop in this experiment.

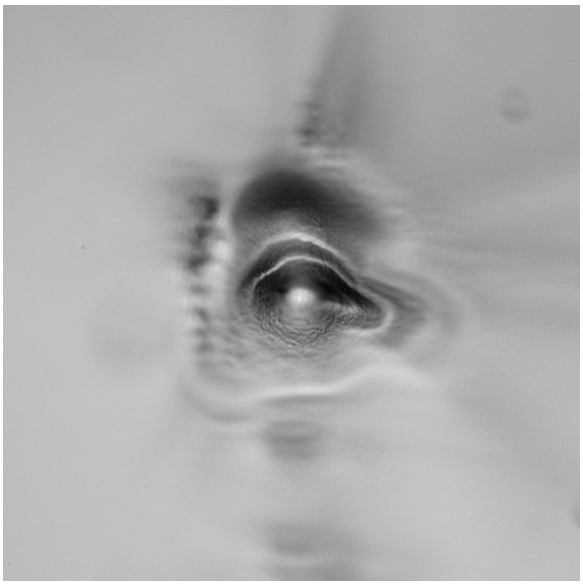

(a)

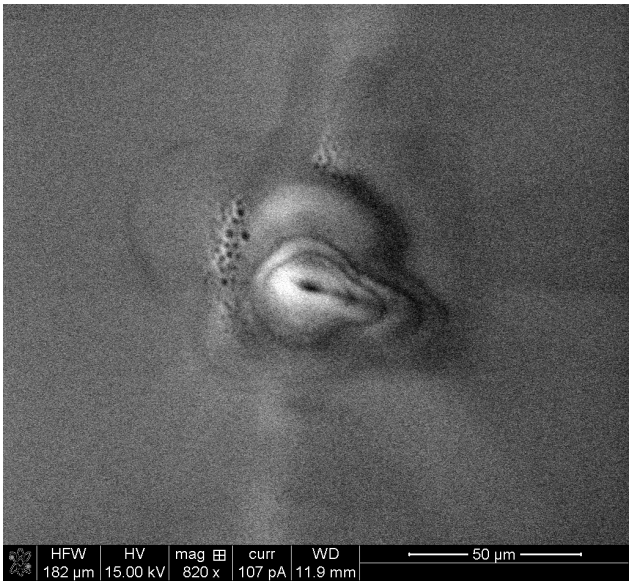

(b)

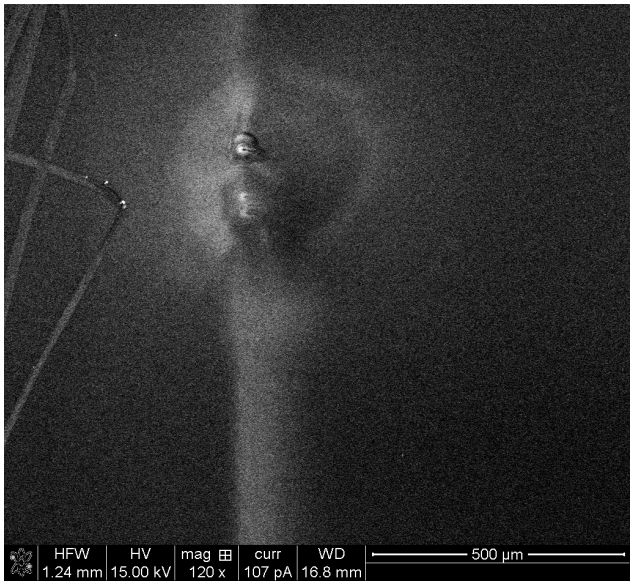

(c)

Figure 4.10: $V_{EM} = 12\ kV, V_{EXT} = 10\ kV, V_2 = 3.5\ kV$ (a) Otical Image, (b)-(c) SEM Image.

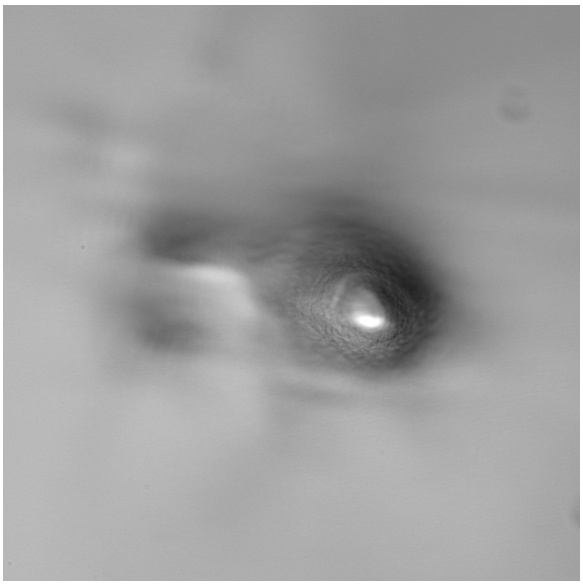

(a)

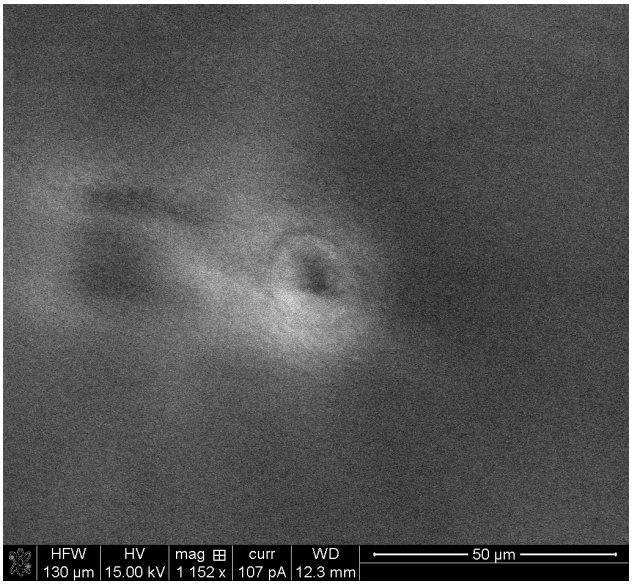

(b)

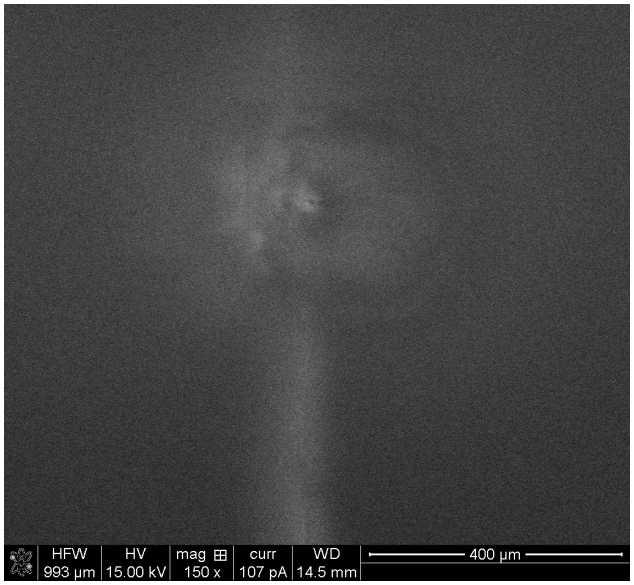

(c)

Figure 4.11: $V_{EM} = 12\ kV, V_{EXT} = 10\ kV, V_2 = 3.7\ kV$ (a) Otical Image, (b)-(c) SEM Image.

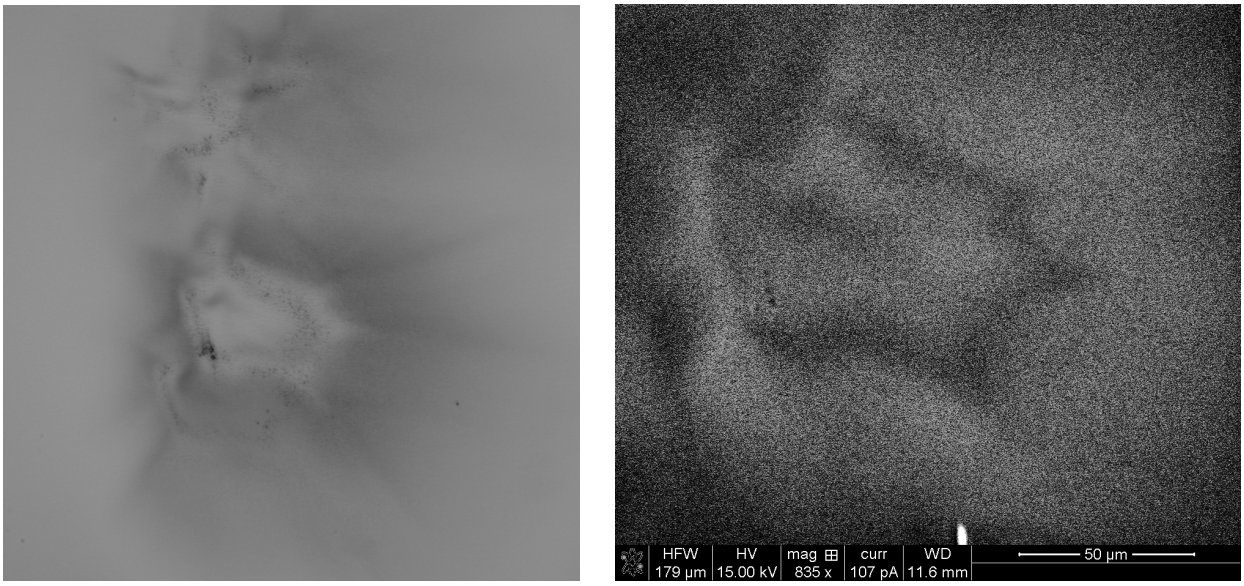

(a) (b)

Figure 4.12: $V_{EM} = 12\ kV, V_{EXT} = 10\ kV, V_2 = 3.9\ kV$ (a) Otical Image, (b) SEM Image.

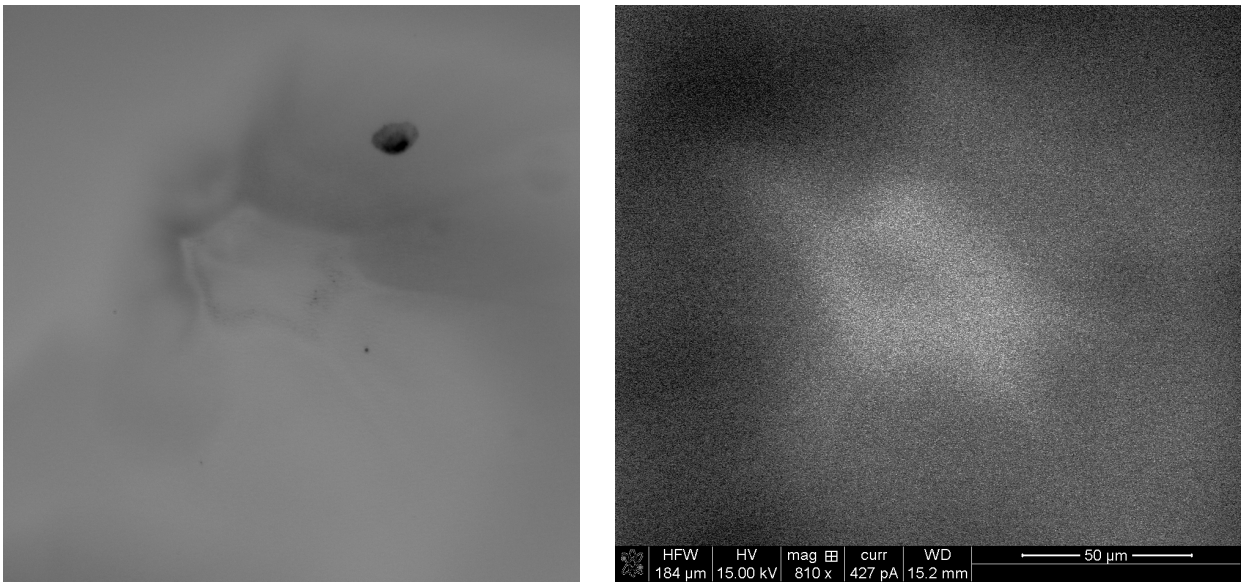

(a) (b)

Figure 4.13: $V_{EM} = 12\ kV, V_{EXT} = 10\ kV, V_2 = 4.3\ kV$ (a) Otical Image, (b) SEM Image.

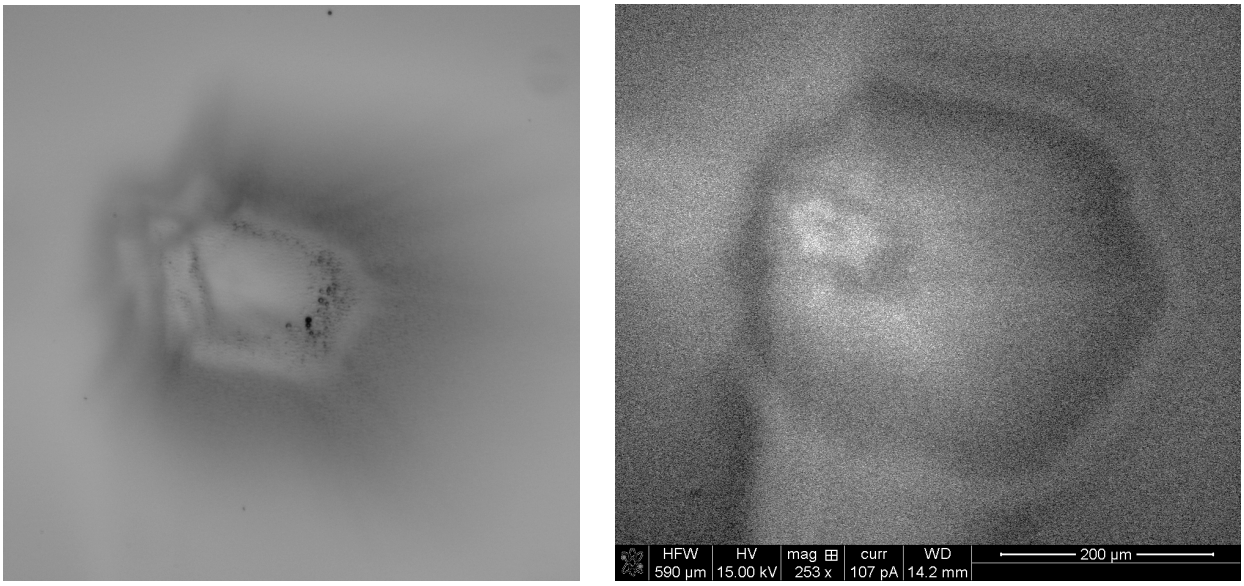

(a) (b)

Figure 4.14: $V_{EM} = 12\ kV, V_{EXT} = 10\ kV, V_2 = 4.5\ kV$ (a) Otical Image, (b) SEM Image.

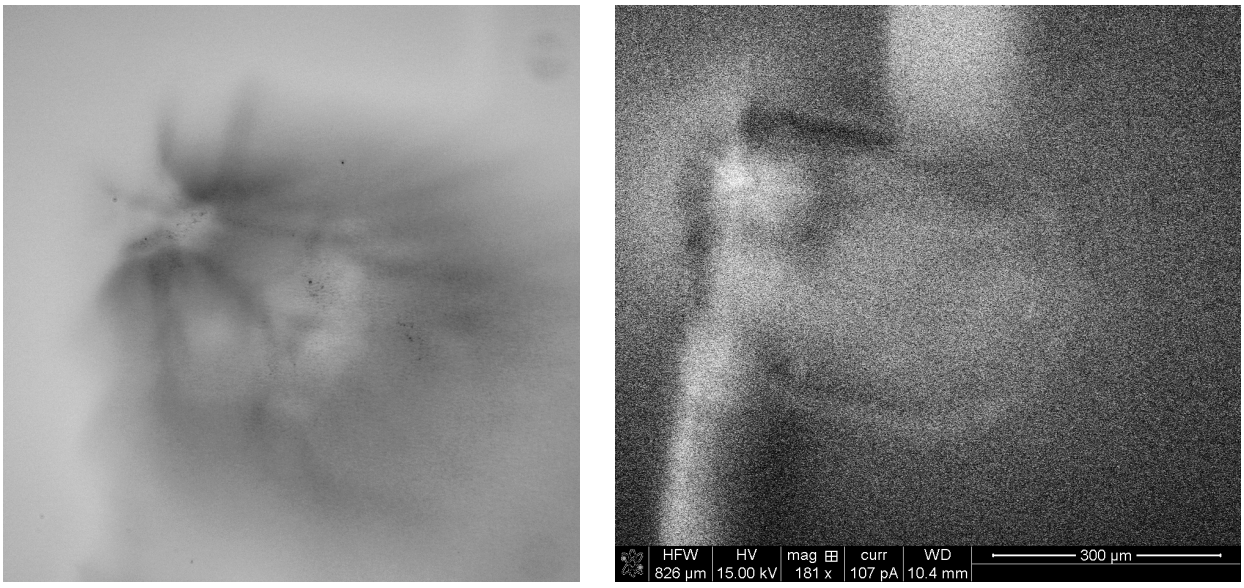

(a) (b)

Figure 4.15: $V_{EM} = 12\ kV, V_{EXT} = 10\ kV, V_2 = 4.7\ kV$ (a) Otical Image, (b) SEM Image.

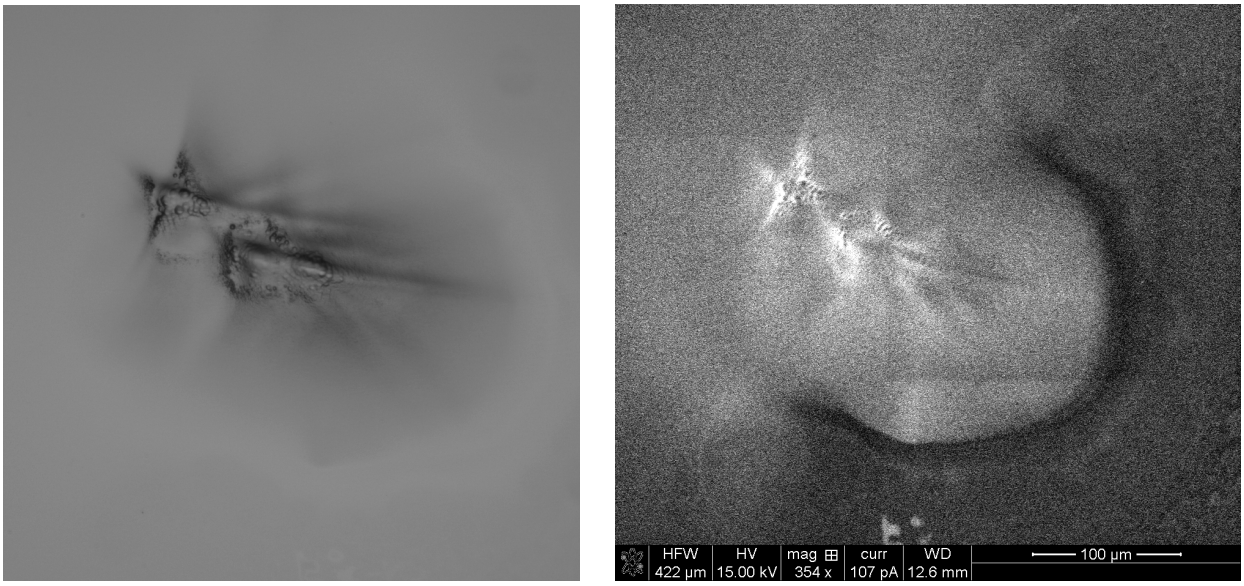

(a) (b)

Figure 4.16: $V_{EM} = 12\ kV, V_{EXT} = 10\ kV, V_2 = 5.1\ kV$ (a) Otical Image, (b) SEM Image.

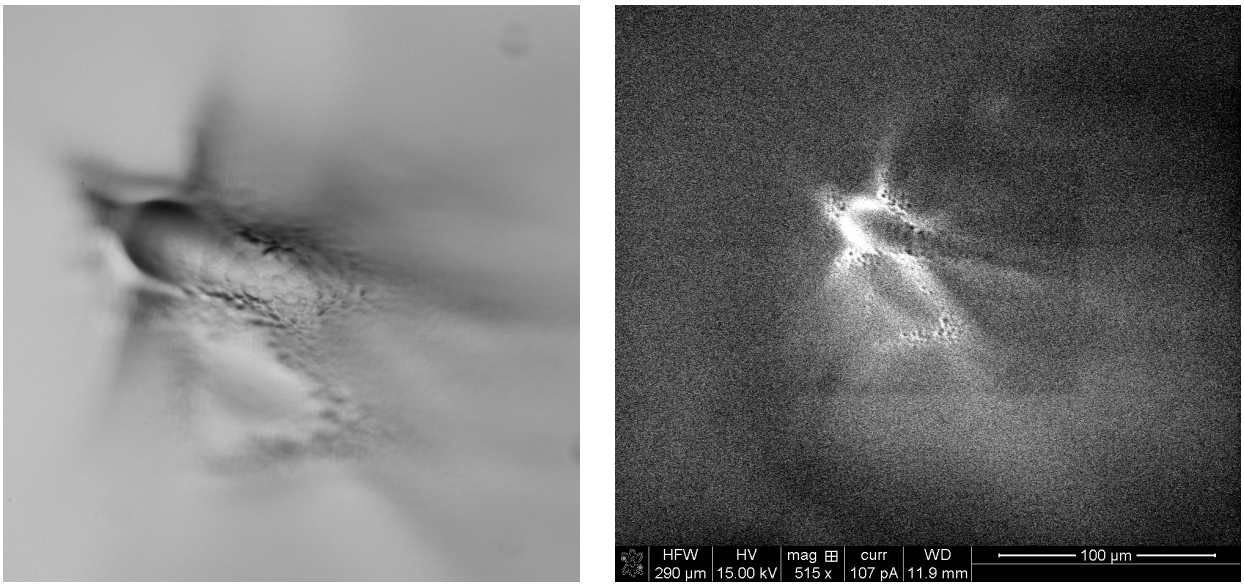

(a) (b)

Figure 4.17: $V_{EM} = 12\ kV, V_{EXT} = 10\ kV, V_2 = 5.1\ kV$ (a) Otical Image, (b) SEM Image.

The aberration figures are plotted and shown for comparison Figure 4.18. The red dash-dot line defines the overall size of the spot struck by beam including both high and low energy projectiles. The blue circle and green circle represent the axial chromatic aberration and spherical aberration figures consequently. The dark shade surrounding the highly sputtered middle area of $90 \times 63\ \mu m$ is where the low energy projectiles start to have sputtering effect on the surface in long exposure.

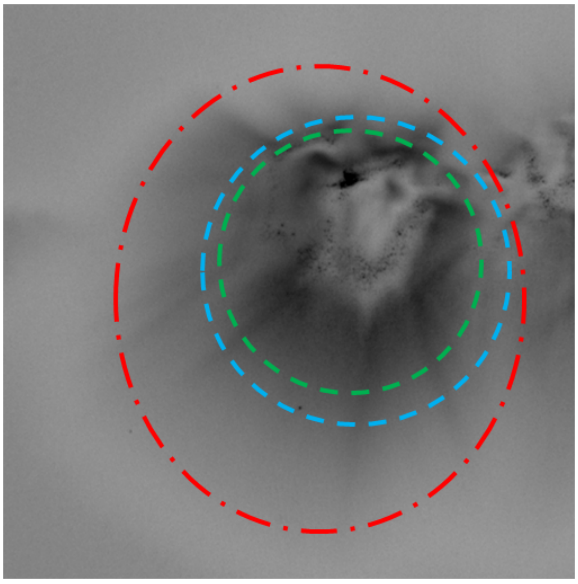

Figure 4.18: Contribution of spherical sberration(- - -) and chromatic aberration (- - -) in spot size (-·-·-) at image plane at $V_2 = 3.9\ kV$.

In the following sections, the optical and SEM images from two other silicon bombardment experiments, a=0.5 and a=0.6 are analyzed similarly. Sputtering is seen around $V_2 = 5\ kV$ and the source image is smaller at $V_2 = 5.1\ kV$ among other potentials that were tested. The dimension of the spot is measured $150 \times 185\ \mu m$. The theory concluded that increasing the potential on second lens makes the dimension of the sputtered spot where the beam struck smaller. The bright core of this spot is a $55 \times 60\ \mu m$ area. Since the experiment setup was not altered from experiment one, it can be assumed that the source misalignment from lens axis is same. All aberration figure discussed above are calculated in a numerical simulation

using the principal trajectories and the equations that were discussed in chapter 2.

Table 4.2: Aberration figures for $V_2 = 5.1\ kV$ for 13.5 μm source offset.

V_2	Spherical Aberration	Astigmatism	Curvature of Field	Distortion	Chromatic Aberration
kV	µm	µm	µm	µm	µm
5.1	76	0.11	0.61	56e-3	15

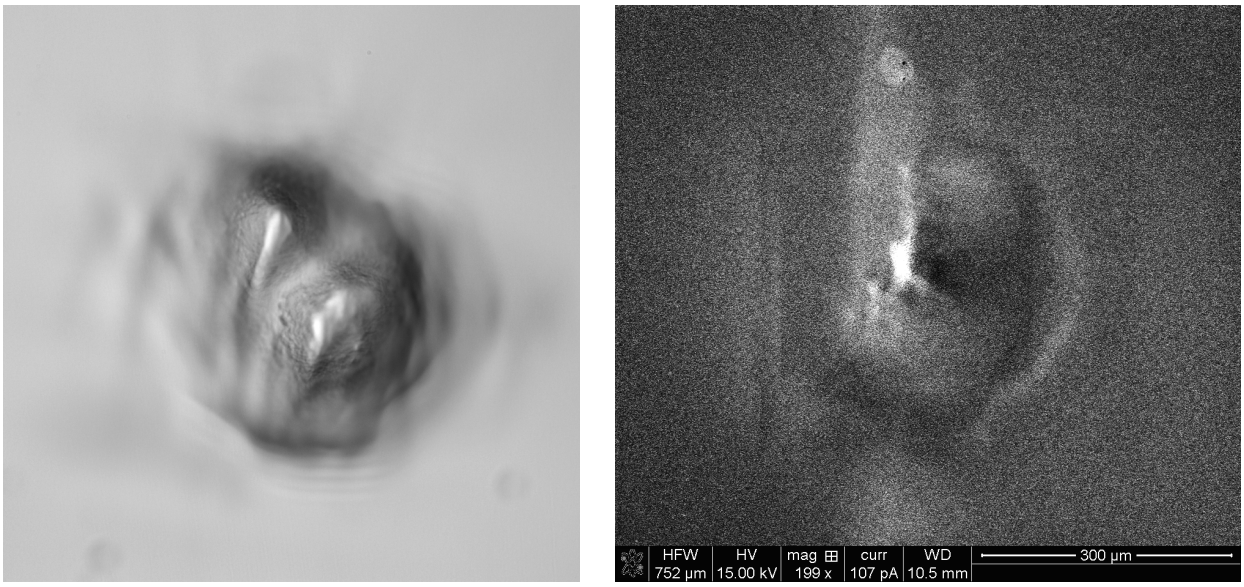

(a) (b)

Figure 4.19: $V_{EM} = 12\ kV, V_{EXT} = 10\ kV, V_2 = 4.5\ kV$ (a) Otical Image, (b) SEM Image.

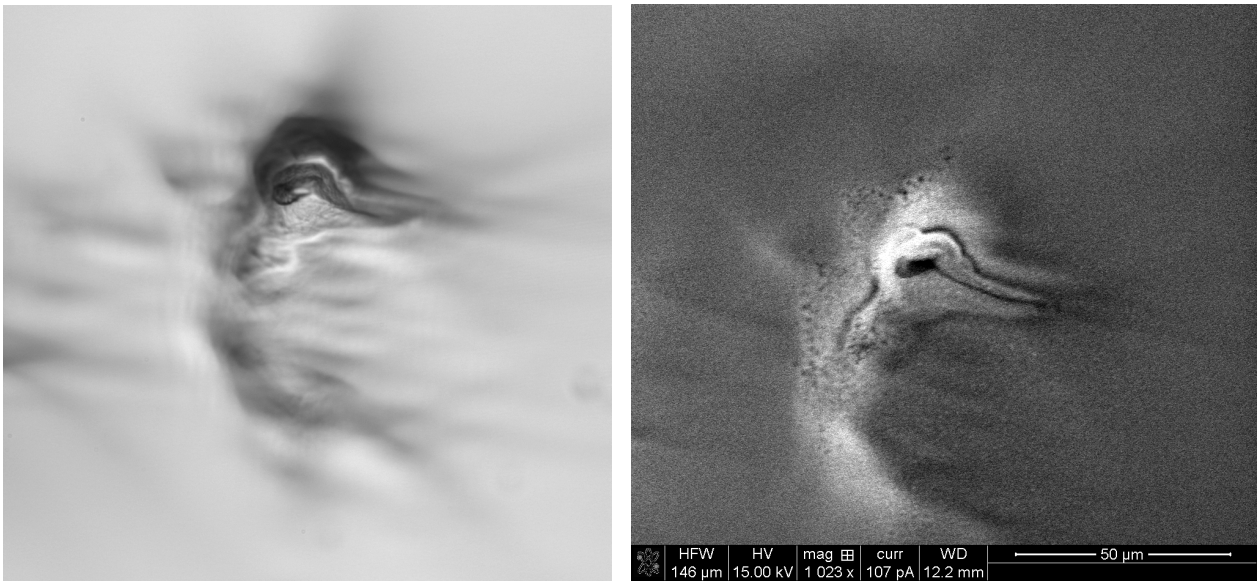

(a) (b)

Figure 4.20: $V_{EM} = 12\ kV, V_{EXT} = 10\ kV, V_2 = 4.7\ kV$ (a) Otical Image, (b) SEM Image.

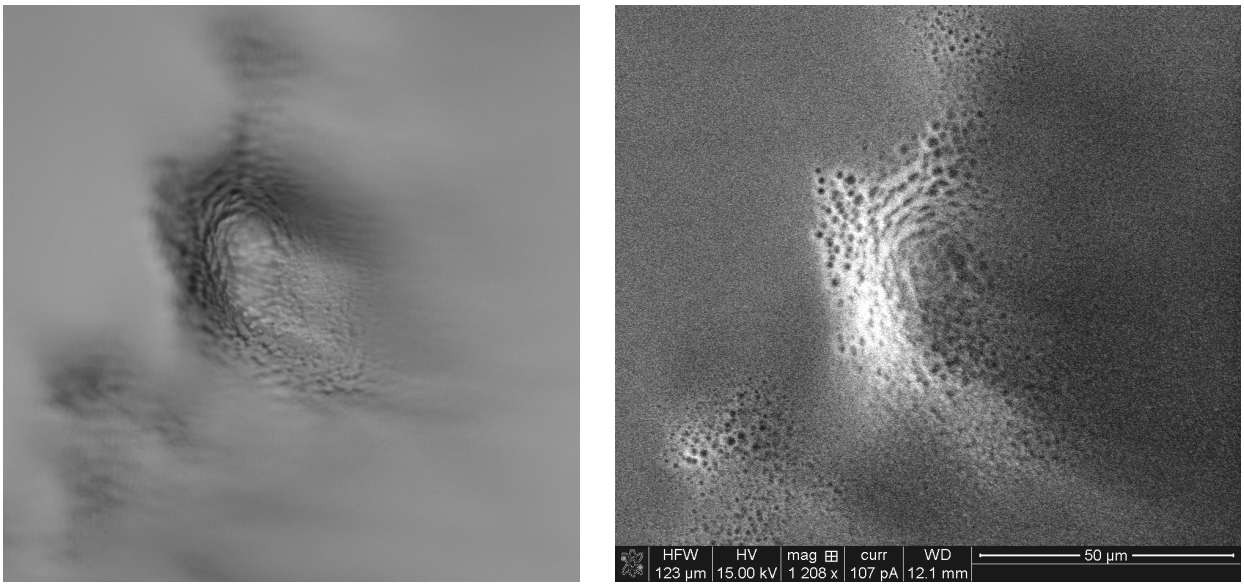

(a) (b)

Figure 4.21: $V_{EM} = 12\ kV, V_{EXT} = 10\ kV, V_2 = 4.9\ kV$ (a) Otical Image, (b) SEM Image.

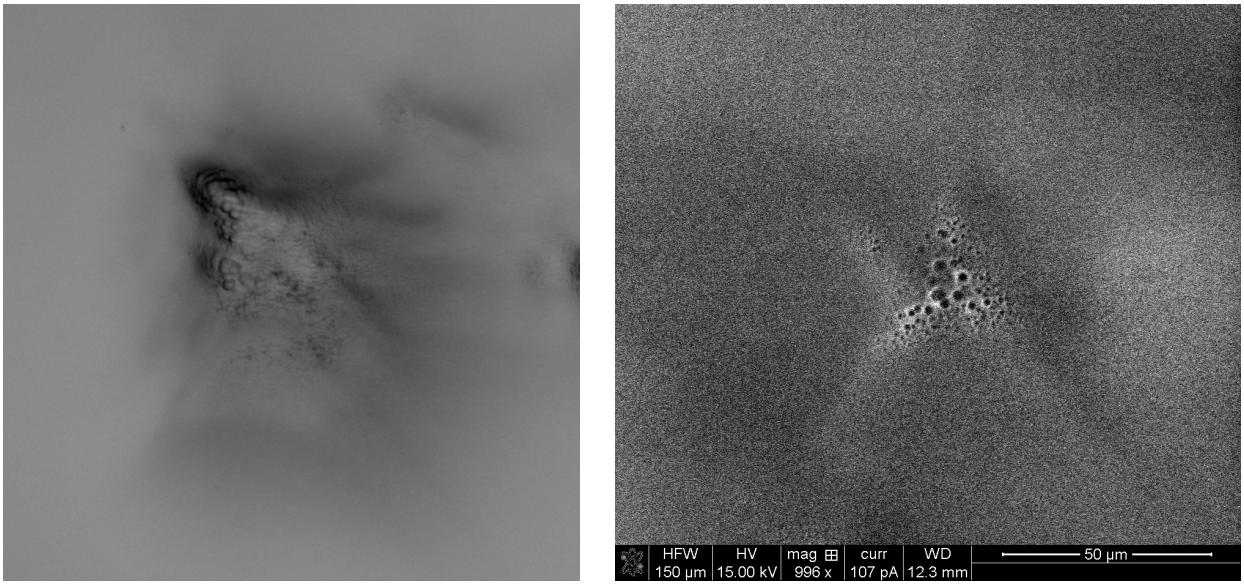

(a) (b)

Figure 4.22: $V_{EM} = 12\ kV, V_{EXT} = 10\ kV, V_2 = 5\ kV$ (a) Otical Image, (b) SEM Image.

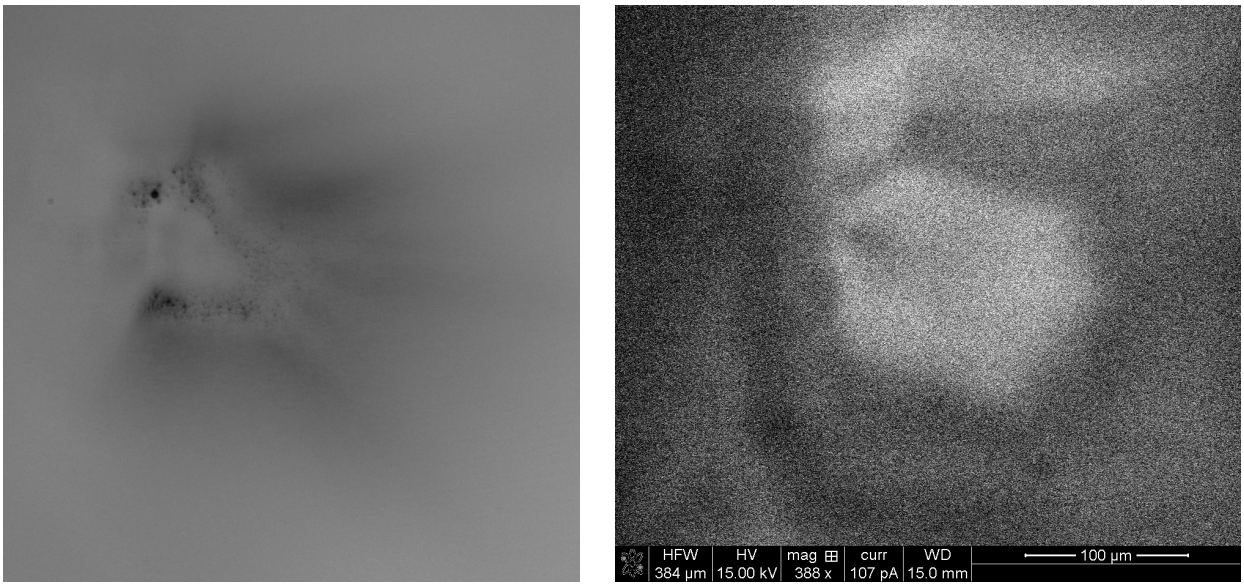

(a) (b)

Figure 4.23: $V_{EM} = 12\ kV, V_{EXT} = 10\ kV, V_2 = 5.1\ kV$ (a) Otical Image, (b) SEM Image.

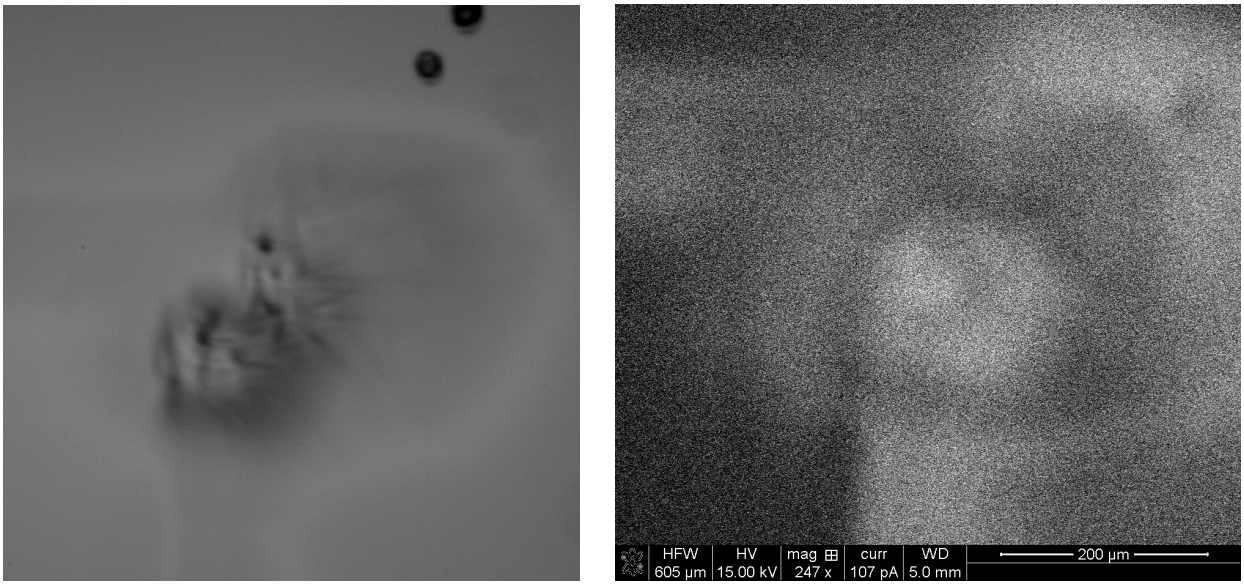

(a) (b)

Figure 4.24: $V_{EM} = 12\ kV, V_{EXT} = 10\ kV, V_2 = 5.3\ kV$ (a) Otical Image, (b) SEM Image.

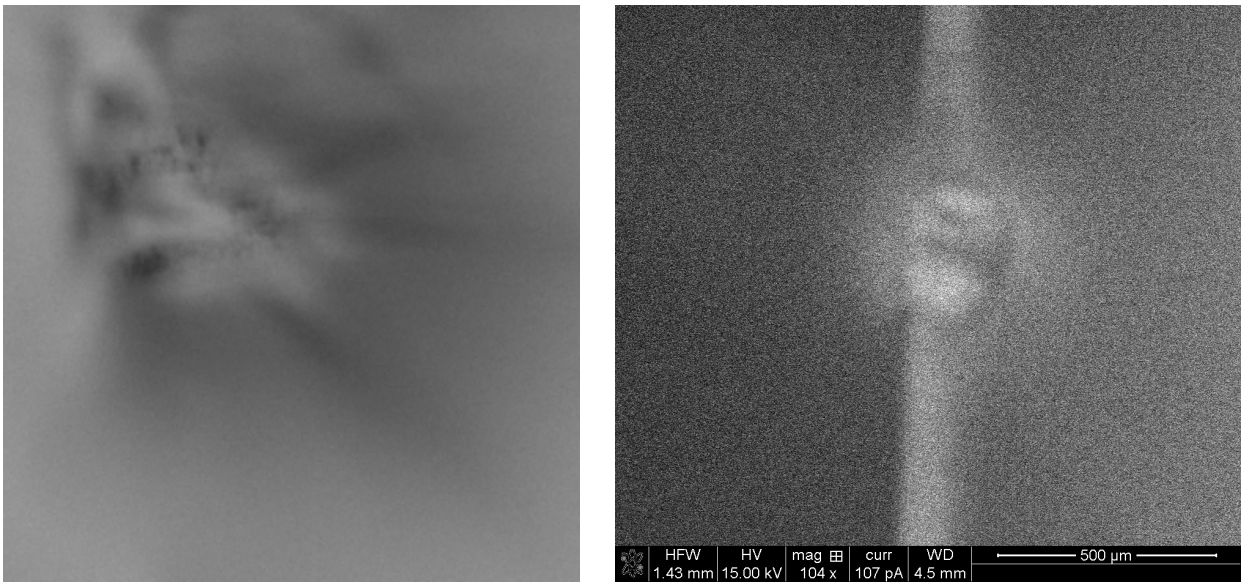

(a) (b)

Figure 4.25: $V_{EM} = 12\ kV, V_{EXT} = 10\ kV, V_2 = 5.5\ kV$ (a) Otical Image, (b) SEM Image.

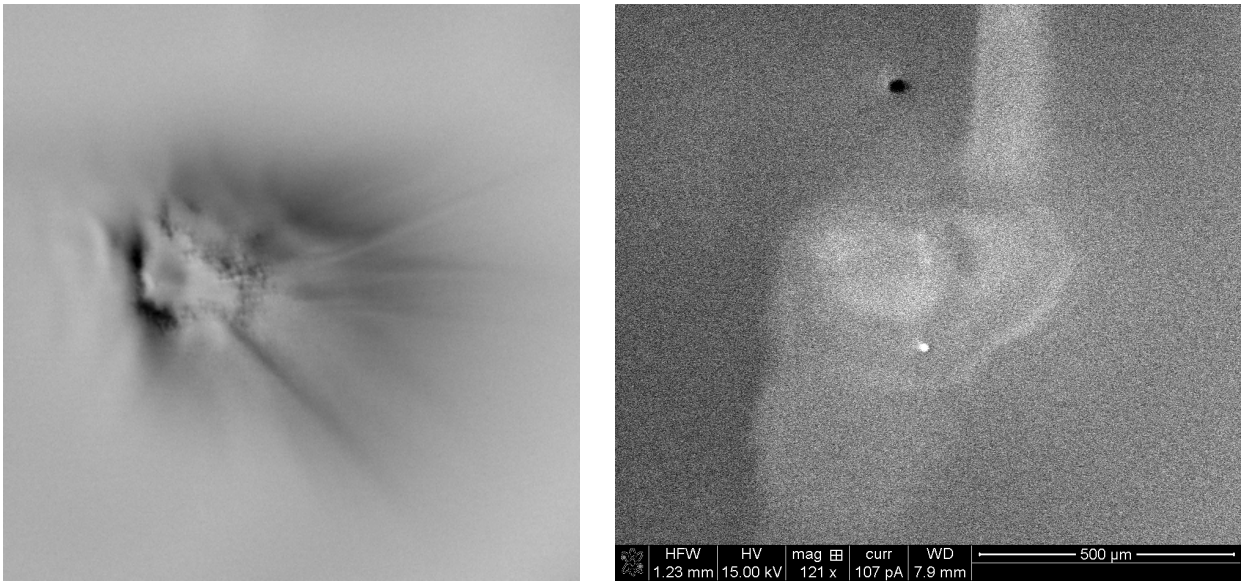

(a) (b)

Figure 4.26: $V_{EM} = 12\ kV, V_{EXT} = 10\ kV, V_2 = 5.7\ kV$ (a) Otical Image, (b) SEM Image.

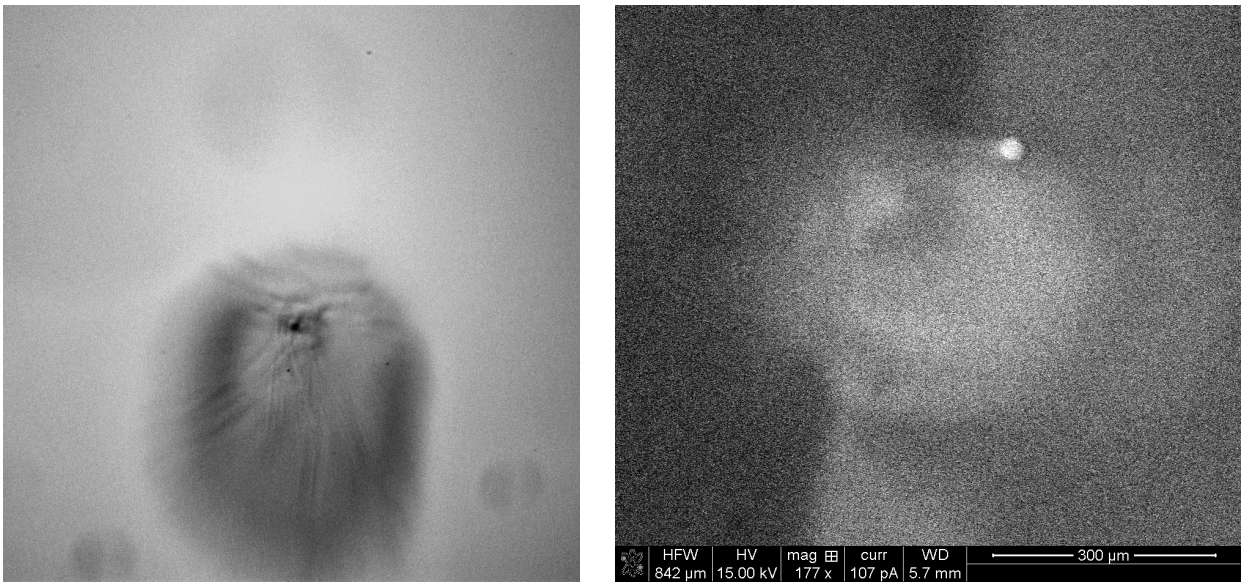

(a) (b)

Figure 4.27: $V_{EM} = 12\ kV, V_{EXT} = 10\ kV, V_2 = 5.9\ kV$ (a) Otical Image, (b) SEM Image.

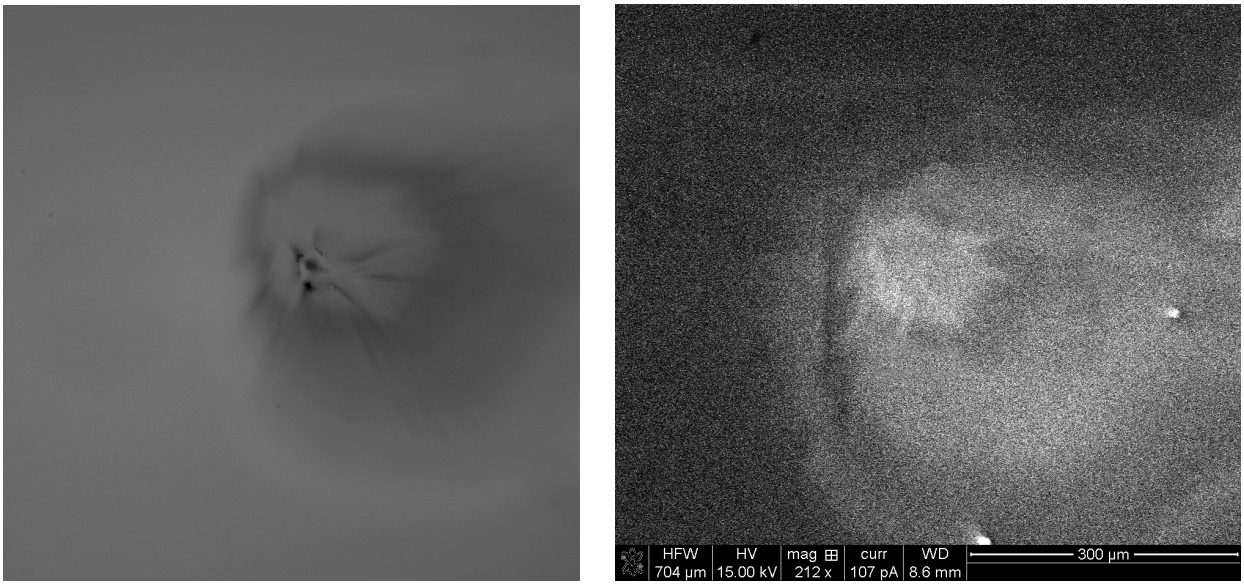

(a) (b)

Figure 4.28: $V_{EM} = 12\ kV, V_{EXT} = 10\ kV, V_2 = 6.1\ kV$ (a) Otical Image, (b) SEM Image.

In Figure 4.29 the aberration figures are plotted for comparison. The red dash-dot line defines the overall size of the spot struck by beam including both high and low energy projectiles. The blue circle and green circle represent the axial chromatic aberration and spherical aberration figures consequently. The central bright spot in this case appears to be slightly deviated from a symmetric circular spot. Applying the same method of analysis on results for the third value of a=0.6 confirms that the focusing voltage of 6 kV for target located at 20.63 mm from center of lens. As the field becomes stronger the dimension and shape of the bombarded area changes. In this case, a dramatic change in pattern is observed. The area struck by a concentrated portion of the beam is seen clearly under microscope. A combination of the sputtering and depositing process appeared to form this area. The circular center sized about 20 μm and overall spot size is measured to $140 \times 180\ \mu m$.

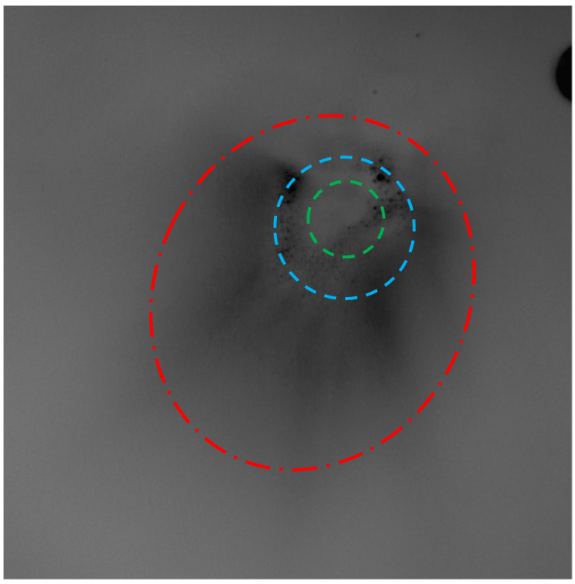

Figure 4.29: Contribution of spherical sberration(- - -) and chromatic aberration (- - -) in spot size (-·-·-) at image plane at $V_2 = 5.1\ kV$.

Following images are from the third part of this experiment. The second electrode's potential was changed between 5 to 7 kV for a=0.6 indicating that nominal voltage is 6 kV.

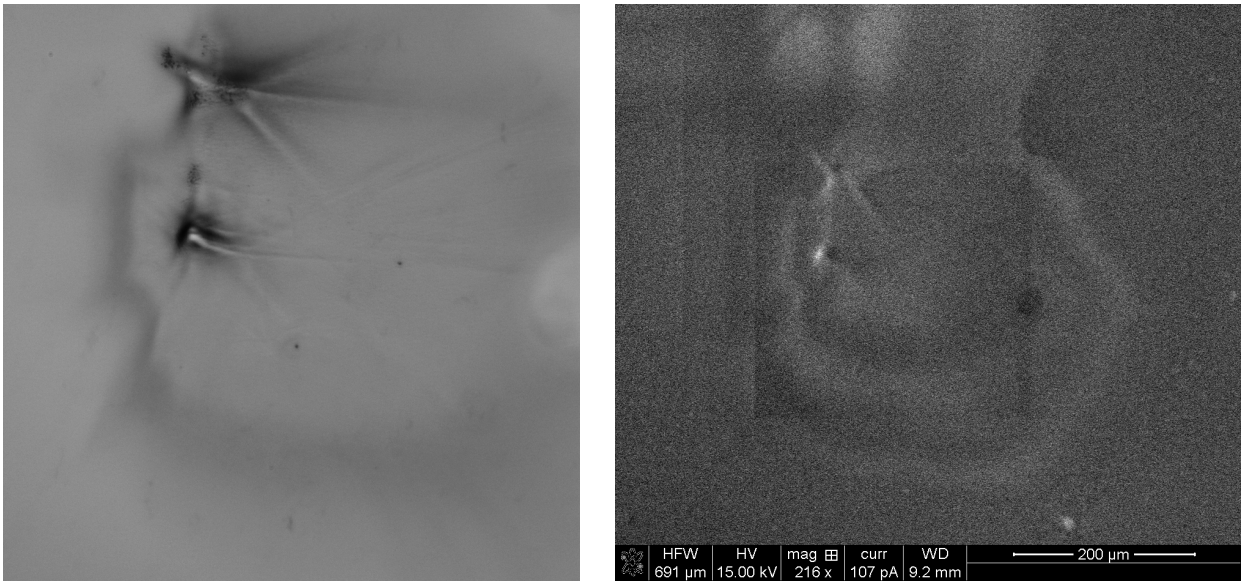

(a) (b)

Figure 4.30: $V_{EM} = 12\ kV, V_{EXT} = 10\ kV, V_2 = 5\ kV$ (a) Otical Image, (b) SEM Image.

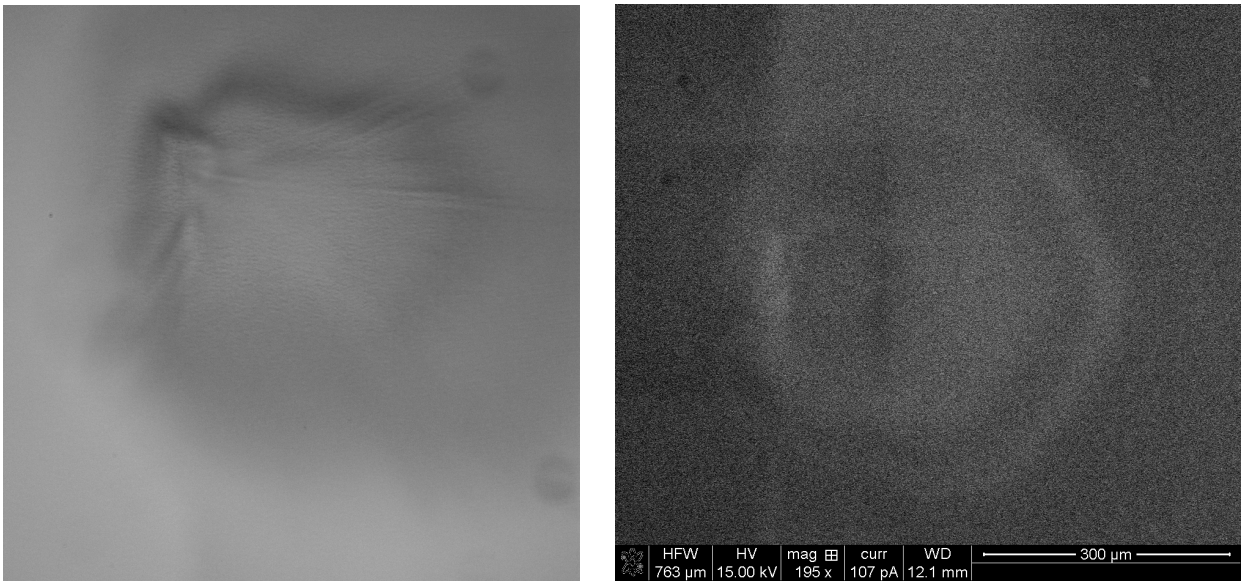

(a) (b)

Figure 4.31: $V_{EM} = 12\ kV, V_{EXT} = 10\ kV, V_2 = 5.2\ kV$ (a) Otical Image, (b) SEM Image.

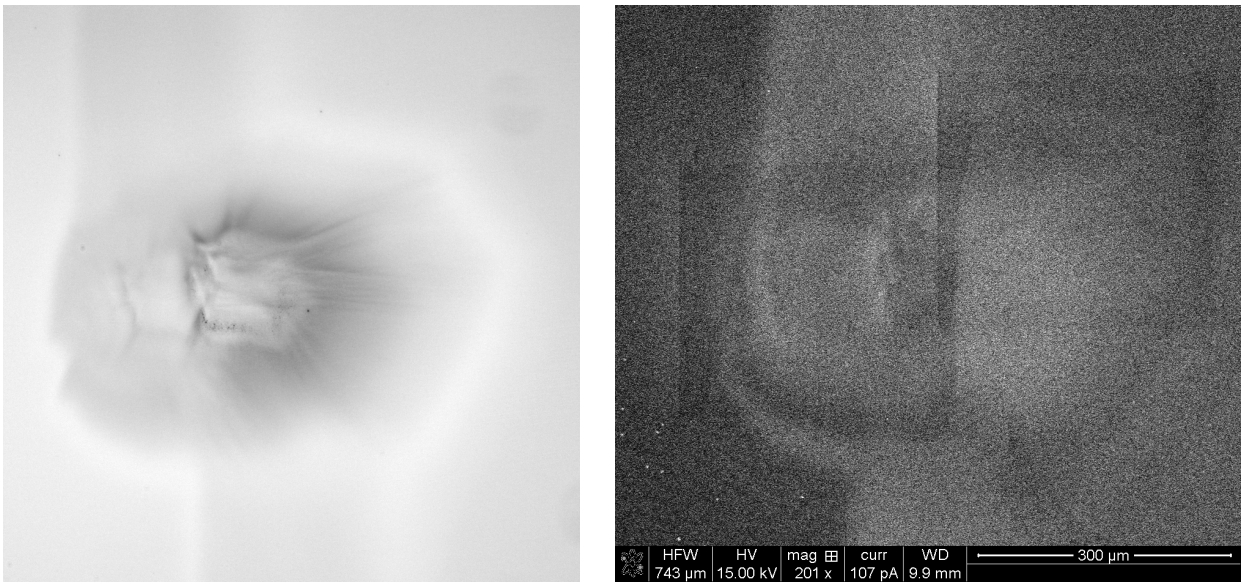

(a) (b)

Figure 4.32: $V_{EM} = 12\ kV, V_{EXT} = 10\ kV, V_2 = 5.4\ kV$ (a) Otical Image, (b) SEM Image.

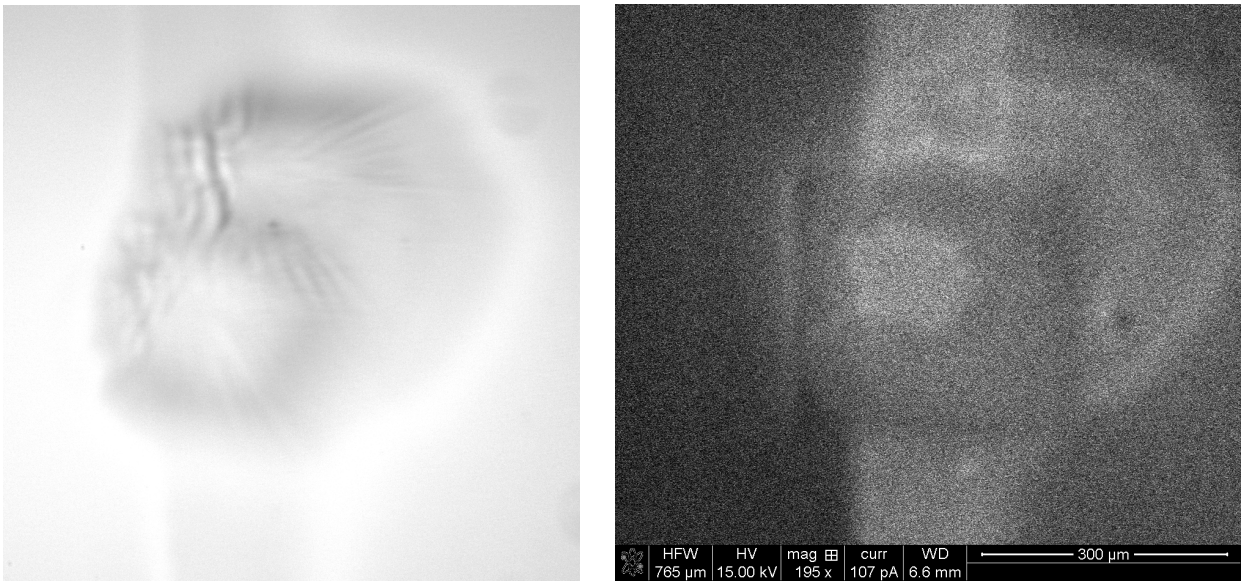

(a) (b)

Figure 4.33: $V_{EM} = 12\ kV, V_{EXT} = 10\ kV, V_2 = 5.4\ kV$ (a) Otical Image, (b) SEM Image.

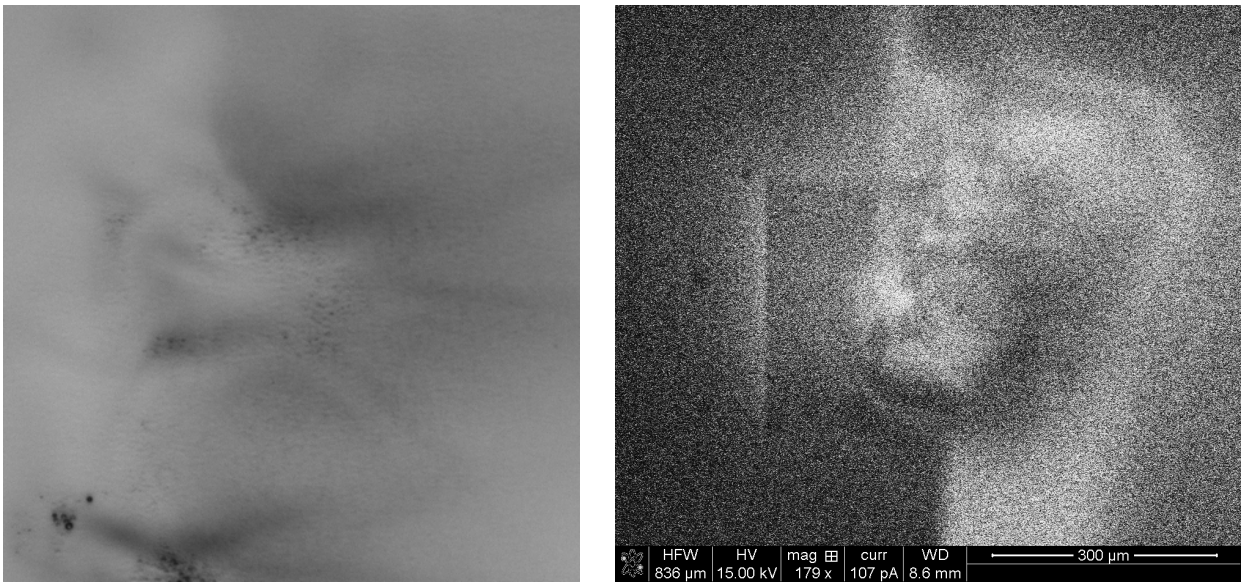

(a) (b)

Figure 4.34: $V_{EM} = 12\ kV, V_{EXT} = 10\ kV, V_2 = 5.8\ kV$ (a) Otical Image, (b) SEM Image.

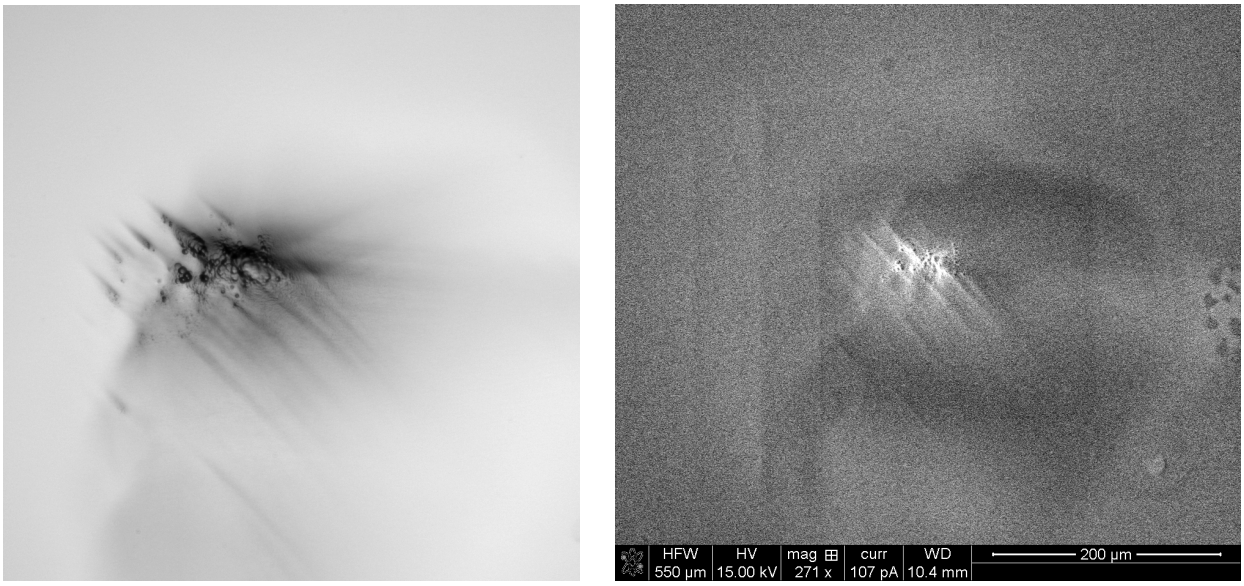

(a) (b)

Figure 4.35: $V_{EM} = 12\ kV, V_{EXT} = 10\ kV, V_2 = 6\ kV$ (a) Otical Image, (b) SEM Image.

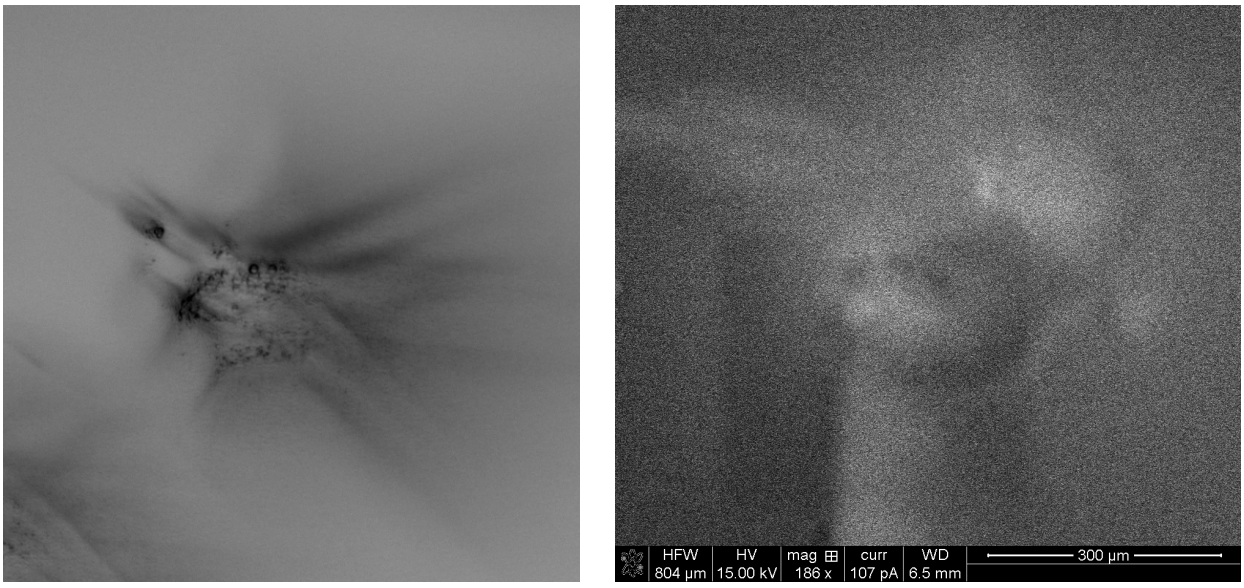

(a) (b)

Figure 4.36: $V_{EM} = 12\ kV, V_{EXT} = 10\ kV, V_2 = 6.2\ kV$ (a) Otical Image, (b) SEM Image.

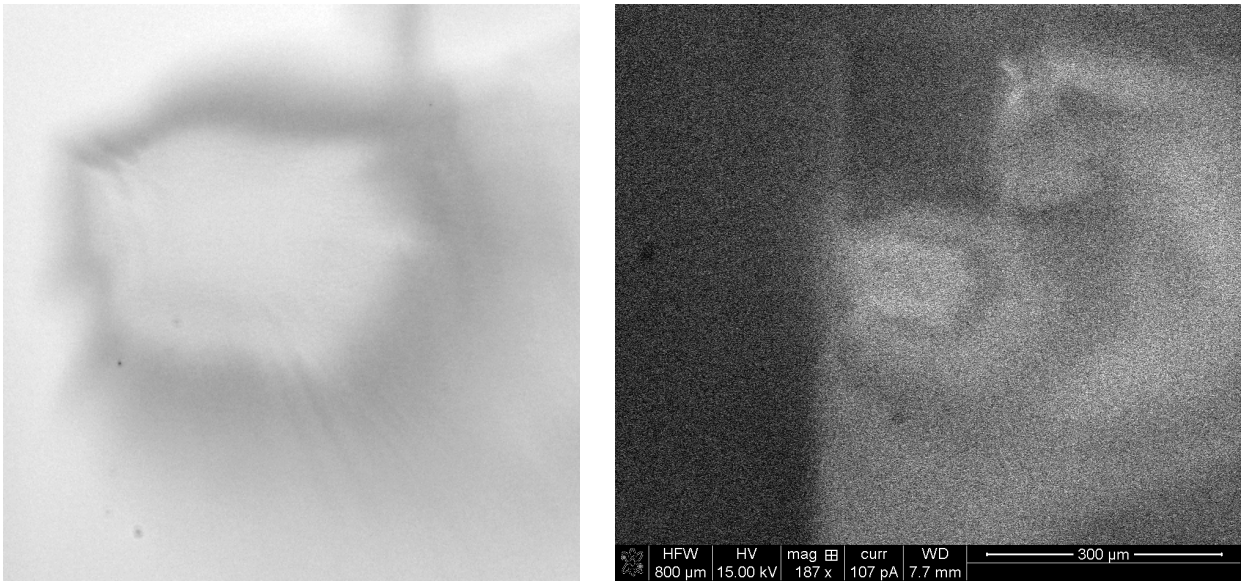

(a) (b)

Figure 4.37: $V_{EM} = 12\ kV, V_{EXT} = 10\ kV, V_2 = 6.4\ kV$ (a) Otical Image, (b) SEM Image.

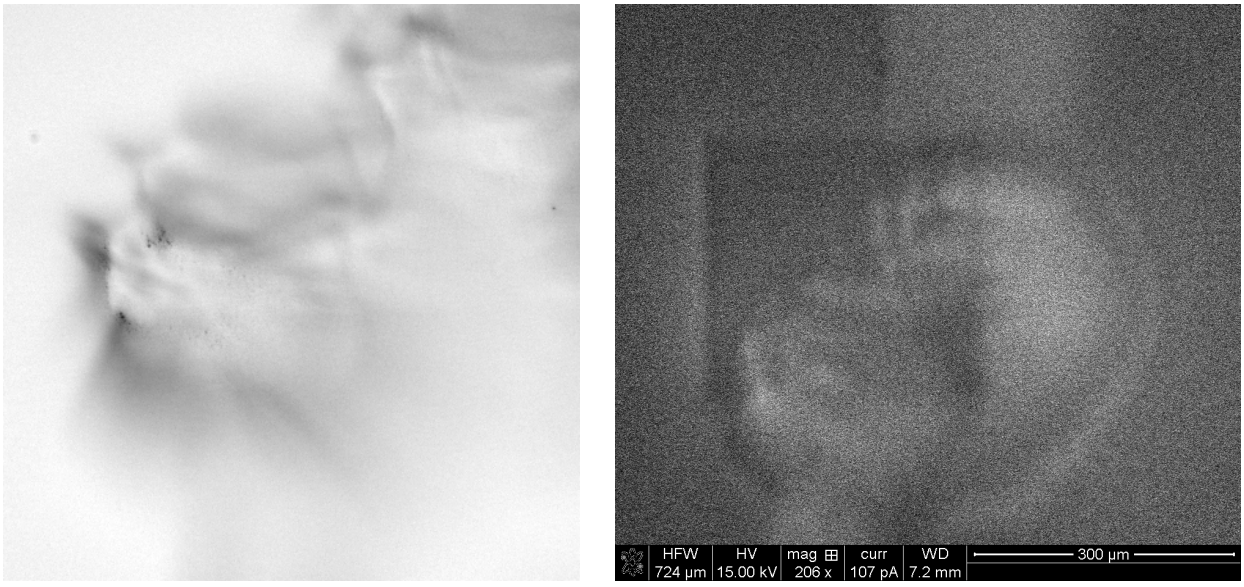

(a) (b)

Figure 4.38: $V_{EM} = 12\ kV, V_{EXT} = 10\ kV, V_2 = 6.8\ kV$ (a) Otical Image, (b) SEM Image.

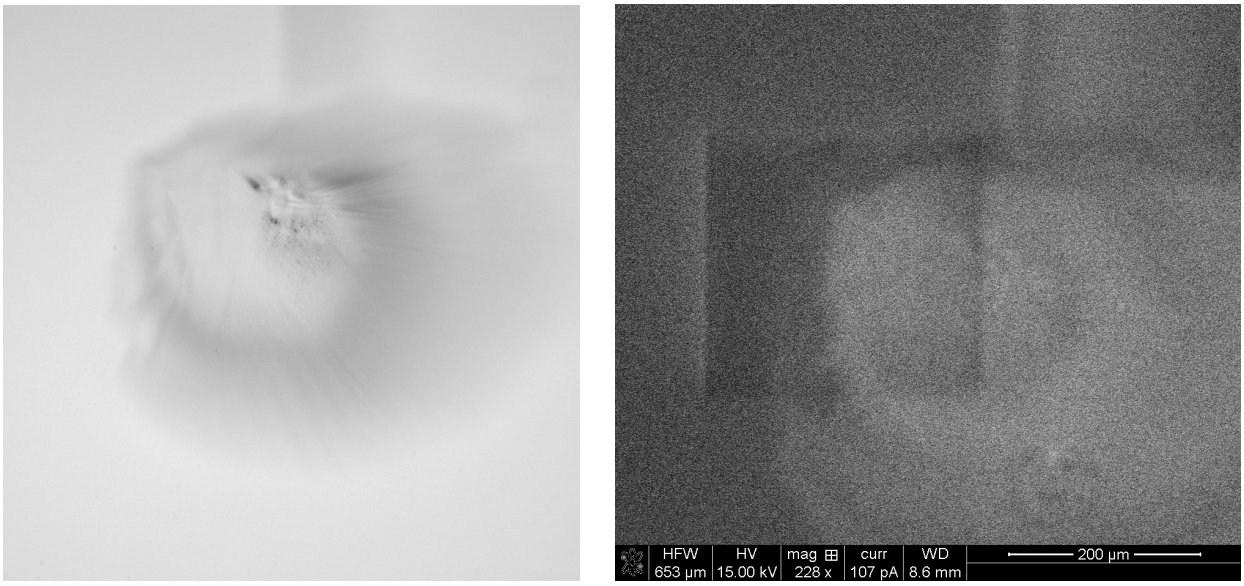

(a) (b)

Figure 4.39: $V_{EM} = 12\ kV, V_{EXT} = 10\ kV, V_2 = 6.8\ kV$ (a) Otical Image, (b) SEM Image.

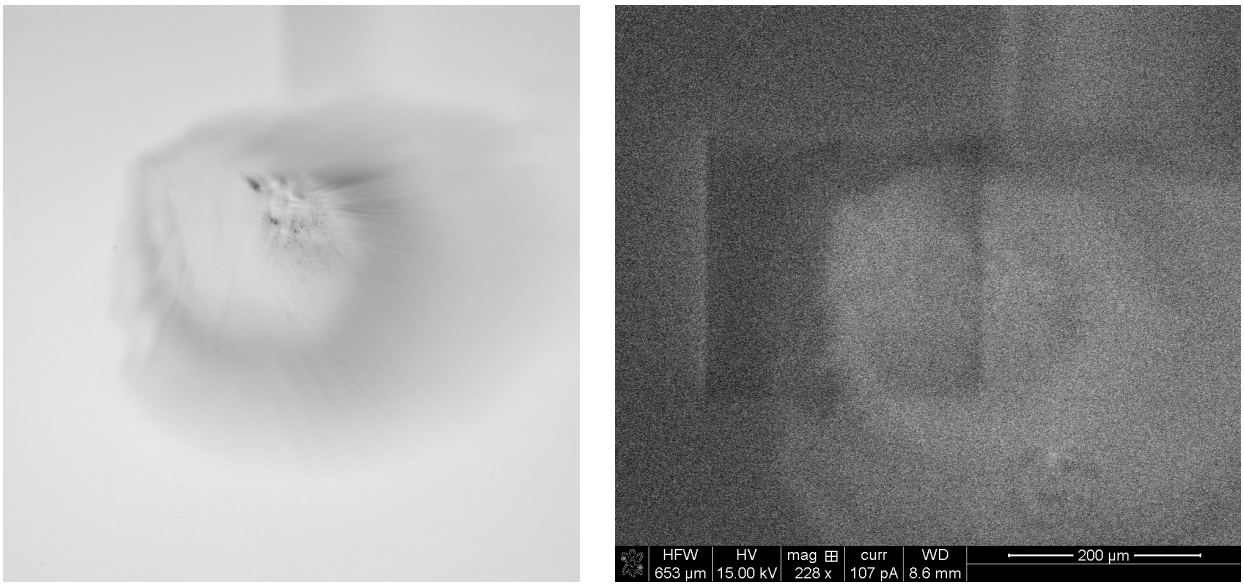

(a) (b)

Figure 4.40: $V_{EM} = 12\ kV, V_{EXT} = 10\ kV, V_2 = 7\ kV$ (a) Otical Image, (b) SEM Image.

The closest focusing voltage is the nominal voltage, $V_2 = 6\ kV$, associated with the target location. A close inspection of the center of activities in a sputtered area of $140 \times 180\ \mu m$ shows an obvious distinction with two previous parts of this experiment. The impacted area is more dense than damages that beam under $V_2 = 3.9$ and $5.1\ kV$ caused on the surface. The astigmatism effect is still visible in this image causing a dimension stretch. The closeup view in Figure 4.41 shows how the impact caused a crater at the center and few small satellite craters around this point. Table 4.3 has the aberration figures discussed before for two other field strength under experiment.

Table 4.3: Aberration figures for $V_2 = 6\ kV$ for $13.5\ \mu m$ source offset.

V_2 (kV)	Spherical Aberration (µm)	Astigmatism (µm)	Curvature of Field (µm)	Distortion (µm)	Chromatic Aberration (µm)
6	69	0.1	50e-3	0.54	12

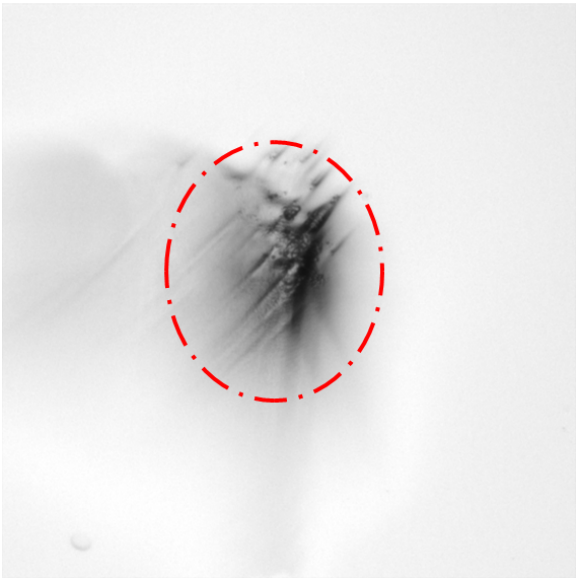

Figure 4.41: Sputtering at the impact spot at $V_2 = 6\ kV$.

In all above experiments the accelerating voltage was set the same as well as other physical parameters during the experiment. One of the circumstances that can affect the size and shape of the bombarded region is stability of the cone jet. Initial pressure that drives the flow to the needle tip depends on the tube's inner diameter and length. After the spray formed and stabilized, providing the driving pressure remains constant the cone-jet and therefore the spray should remain stable. When fused silica tube with smaller inner diameter is used, a higher range of pressure is needed to maintain the spray. During this experiment initially atmosphere level pressure was applied to transfer the liquid to the needle tip and then the bottle pressure was kept around 200 torr. Very high pressure might cause flooding the system and causing a short between electrodes or sparks. The cone-jet was observed continuously during bombardment. At few points the cone became unstable and its tip shifted to the edge of the needle. None of these incidents were at the focusing voltage mentioned in previous analysis. In order to sum up this experiment, the dimension of the sputtered area for three level of field strength are compared in Table 4.4. These dimensions agree with the decreasing trend with increasing potential that was predicted in Figure 2.8.

Table 4.4: Dimension of the sputtered area.

V_2 (kV)	3.9	5.1	6
dimension(µm)	265×310	150×185	140×180

4.4 Experiment III

The approach used in the previous experiment can be used to determine the focusing field strength for any relative distance between target and lens. It is going to be more efficient if smaller voltage range and interval chosen. Below another example of sputtering silicon by electrospray bombardment for target located 20 mm far from the lens center. Target was exposed to the beam for 120s at each point. The potential was increased 50 V in transition between spots. Figure 4.42 shows a series of SEM images from bombarded spots under same magnification. A visual examination of these images gives the focusing voltage at $V_2 = 5.45\ kV$. For the best part, this resolution of voltage suffice. The power supply used in this experiment can be adjusted to $\delta\ V_2 = 1\ V$, however adjustments smaller than 10 V might not even be useful or practical.

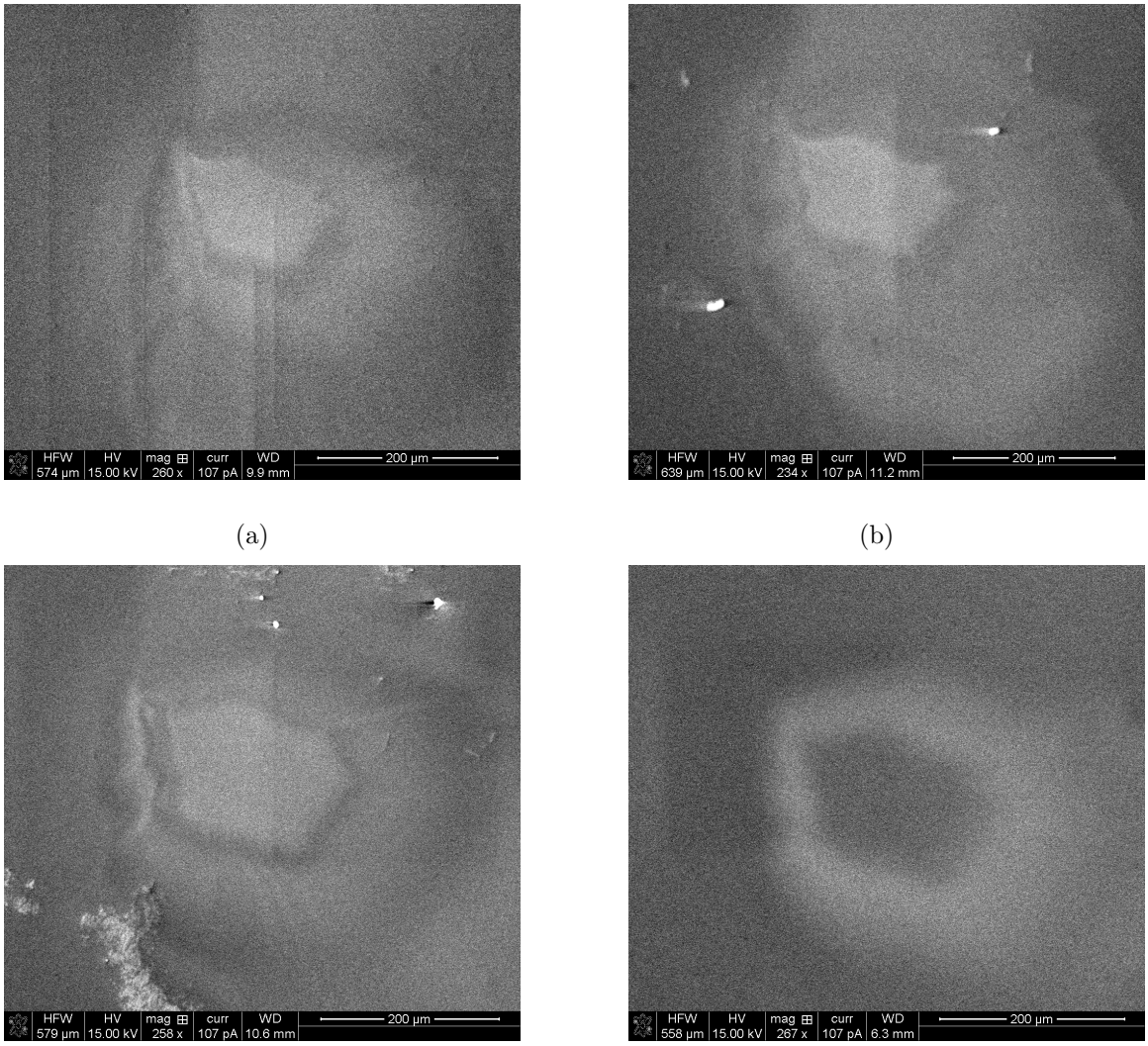

(a) (b)

(c) (d)

Figure 4.42: $V_{EM} = 12\ kV, V_{EXT} = 10\ kV, V_2 = 5.35 - 5.6\ kV, ZI = 20\ mm$, (a) 5.45 kV, (b)5.5 kV, (c) .5.55 kV, (d) 5.6 kV.

Chapter 5

Summary and Conclusion

The experimental research on electrospray beam focusing is presented in chapters 2, 3, 4. The ultimate goal of this study is to seek the possibility of introducing electrospray nanodeoplet beam as a new source of charged particles for microfabrication and surface engineering processes. Electrosprayed charged droplets have proven to have an efficient sputtering effect on different material especially semiconductor material. The higher sputtering rate has root in their lower charge to mass ratio than ion beam that provides higher momentum under same accelerating voltage. In addition, the variety of the chemical composition and molecular mass of ionic liquid source used in atomization process are appealing characteristics for microfabrication technology. In this thesis, a focusing apparatus is presented which deflects the diverging projectiles trajectories from source through a tailors electrostatic field. Electrospray beam tracing theory and numerical integration performed to define the image of the source where beam is focused to a point again with highest energy density along the beam trajectory. In a series of experiments, a number of silicon targets were bombarded with energetic charged nanodroplet sprayed from EMI-Im source and focused in electrostatic field with different strength. The bombarded area were inspected for two purposes: first, deter-

mine the electrostatic field strength imposed by lens electrodes associated with the target location and second, to learn about the existing source of errors such as misalignment in the focusing columns. The lens's different type of aberration are seen both in shape and size of the sputtered area when compared to the ideal image of a point source. Some aberrations such as spherical aberration cannot be avoided by increasing accuracy in fabrication and need to be corrected with further elements such as multipole commonly used in charge particle optics. This can be next stages in electrospray focusing research. Other types of geometric aberrations such as astigmatism can be improved by minimizing the fabrication imperfections and eliminating misalignment in focusing column assembly. To this end, a novel design of electrostatic lens is presented that uses microfabrication techniques to minimize the fabrication and assembly errors. Microfabrication process of the electrostatic lens made of bonded silicon and glass wafers was successfully implemented and presented in experimental methods. Preliminary experiments confirmed that this design meets the voltage and physical accuracy requirements. Improvement of the fabrication process and including multipole deflector and corrector are suggested for the next stages of this research.

Appendix A

Fabrication Recipes

A.1 DRI Etch Recipe

1. Spin AZ4620 photoresist for 10 sec at 500 rpm (spread) followed by 30 sec at 2000 rpm (spin).
2. Soft bake at 90 ℃ for 18 min.
3. Spin AZ4620 photoresist for 10 sec at 500 rpm (spread) followed by 40 sec at 5000 rpm (spin).
4. Soft bake at 90 ℃ for 18 min.
5. Expose photoresist using soft contact for 105 sec.
6. Develop in AZ 400K diluted 3.5:1 with water for 4 min.
7. Hard bake at 120 ℃ for 20 min.

8. DRI etch in STS tool using Process B recipe (in case of bonded wafer DRIE process runs in the intervals of 10 min etching followed by 5 min cooling.

9. Remove soft mask by soaking in Solvent followed by a Piranha process to remove PR residues.

A.2 Adhesive Bonding

1. Spin Adhesion Promoter (Microsystem VM 652); 500rpm,10s, 2500rpm;30 sec.

2. Bake on hotplate for 1 min at 120 ℃.

3. Thickness less than $4\mu m$ is expected after cure!

4. Locate the top wafer on coated piece on hotplate, locate the load.

5. Soft bake for 18 min at 120 ℃.

6. Cure

   Reach 200 ℃ from room temperature with the slope 10 ℃/min.

   Bake at 2 Bake on hotplate for 1 min at 120 ℃ for 30 min.

   Reach 375 ℃ from 200 ℃ with the slope 10 ℃/min.

   Bake at 375 ℃ for 1hr.

   Return to room temperature.

A.3 RCA1 (Surface clean and activation process)

1. Mix 325 ml DI water and 65 ml Ammonium Hydroxide.

2. Heat the mix up to 70 ℃.

3. Remove the container from the hotplate and add 65 ml Hydrogen Peroxide.

4. Keep the temperature of the solution around 70 ℃ on hotplate.

5. Soak samples in the solution for 10 to 15 min.

6. Rinse with DI water.

A.4 Plasma Activated Bonding

1. Solvent clean.

2. Piranha or RCA1 Surface clean and activation

3. 3 min Plasma Activation in Plasma-therm or Gasonics tools.

4. Soak in DI water.

5. N_2 blow dry.

6. Bring surfaces into contact and press to form primary bond.

7. Anneal at 24 to 200 ℃ on hotplate, ramp (60 ℃/hr)for 4 hours

Bibliography

[1] C.-S. Kim, S.-H. Ahn, and D.-Y. Jang, "Review: Developments in micro/nanoscale fabrication by focused ion beams," *Vacuum*, vol. 86, no. 8, pp. 1014 – 1035, 2012.

[2] J. Mayer, L. A. Giannuzzi, T. Kamino, and J. Michael, "Tem sample preparation and fib-induced damage," *MRS Bulletin*, vol. 32, pp. 400–407, 005 2007.

[3] A. Kirkpatrick, "Gas cluster ion beam applications and equipment," *Nuclear Instruments and Methods in Physics Research Section B: Beam Interactions with Materials and Atoms*, vol. 206, pp. 830 – 837, 2003. 13th International Conference on Ion Beam Modification of Materials.

[4] N. Winograd, "The magic of cluster sims," *Analytical Chemistry*, vol. 77, no. 7, pp. 142 A–149 A, 2005.

[5] I. Yamada, J. Matsuo, N. Toyoda, T. Aoki, and T. Seki, "Progress and applications of cluster ion beam technology," *Current Opinion in Solid State and Materials Science*, vol. 19, no. 1, pp. 12 – 18, 2015. Ion Beam Modification of Materials.

[6] I. Yamada and N. Toyoda, "Nano-scale surface modification using gas cluster ion beams a development history and review of the japanese nano-technology program," *Surface and Coatings Technology*, vol. 201, no. 1920, pp. 8579 – 8587, 2007. {SMMIB} 200514th International Conference on Surface Modification of Materials by Ion Beams.

[7] J. Greer, D. Fenner, J. Hautala, L. Allen, V. DiFilippo, N. Toyoda, I. Yamada, J. Matsuo, E. Minami, and H. Katsumata, "Etching, smoothing, and deposition with gas-cluster ion beam technology," *Surface and Coatings Technology*, vol. 133134, pp. 273 – 282, 2000.

[8] J. Orloff, L. W. Swanson, and M. Utlaut, "Fundamental limits to imaging resolution for focused ion beams," *Journal of Vacuum Science & Technology B: Microelectronics and Nanometer Structures Processing, Measurement, and Phenomena*, vol. 14, no. 6, pp. 3759–3763, 1996.

[9] M. Gamero-Castaño and M. Mahadevan, "Sputtering of silicon by a beamlet of electrosprayed nanodroplets," *Applied Surface Science*, vol. 255, no. 20, pp. 8556 – 8561, 2009.

[10] B. D. Prince, B. A. Fritz, and Y.-H. Chiu, *Ionic Liquids in Electrospray Propulsion Systems*, ch. 2, pp. 27–49.

[11] L. P. Francois Martel and P. Lozano, "Miniature ion electrospray thrusters and performance test on cubesat," in *26th annual AIAA/USU conference on small satellites*, 2012.

[12] G. Lenguito, J. F. de la Mora, and A. Gomez, "Scaling up the power of an electrospray microthruster," *Journal of Micromechanics and Microengineering*, vol. 24, no. 5, p. 055003, 2014.

[13] S. Dandavino, C. Ataman, C. N. Ryan, S. Chakraborty, D. Courtney, J. P. W. Stark, and H. Shea, "Microfabricated electrospray emitter arrays with integrated extractor and accelerator electrodes for the propulsion of small spacecraft," *Journal of Micromechanics and Microengineering*, vol. 24, no. 7, p. 075011, 2014.

[14] M. Gamero-Castaño, "The expansion of colloid thruster beams," in *31st International Electric Propulsion Conference, University of Michigan, Ann Arbor*, 2009.

[15] J. B. Fenn, "Electrospray ionization mass spectrometry: How it all began," *Journal of Biomolecular Techniques*, vol. 13, pp. 101–118, September 2002.

[16] R. Borrajo-Pelaez, E. Grustan-Gutierrez, and M. Gamero-Castao, "Sputtering of si, sic, inas, inp, ge, gaas, gasb, and gan by electrosprayed nanodroplets," *Journal of Applied Physics*, vol. 114, no. 18, pp. 184304–1–6, 2013.

[17] R. Borrajo-Pelaez, F. Saiz, and M. Gamero-Castao, "The effect of the molecular mass on the sputtering of si, sic, ge, and gaas by electrosprayed nanodroplets at impact velocities up to 17km/s," *Aerosol Science and Technology*, vol. 49, no. 4, pp. 256–266, 2015.

[18] S. Banerjee and S. Mazumdar, "Electrospray ionization mass spectrometry: A technique to access the information beyond the molecular weight of the analyte," *International Journal of Analytical Chemistry*, vol. 2012, 2012. Article ID 282574.

[19] P. Kebarle and U. H. Verkerk, "Electrospray: From ions in solution to ions in the gas phase, what we know now," *Mass Spectrometry Reviews*, vol. 28, no. 6, pp. 898–917, 2009.

[20] A. P. Bruins, "Mechanistic aspects of electrospray ionization," *Journal of Chromatography A*, vol. 794, no. 12, pp. 345 – 357, 1998.

[21] G. Taylor, "Electrically driven jets," *Proceedings of the Royal Society of London A: Mathematical, Physical and Engineering Sciences*, vol. 313, no. 1515, pp. 453–475, 1969.

[22] J. F. de la Mora, "The fluid dynamics of taylor cones," *Annual Review of Fluid Mechanics*, vol. 39, no. 1, pp. 217–243, 2007.

[23] M. S. Wilm and M. Mann, "Electrospray and taylor-cone theory, dole's beam of macromolecules at last?," *International Journal of Mass Spectrometry and Ion Processes*, vol. 136, no. 23, pp. 167 – 180, 1994.

[24] G. Taylor, "Disintegration of water drops in an electric field," *Proceedings of the Royal Society of London A: Mathematical, Physical and Engineering Sciences*, vol. 280, no. 1382, pp. 383–397, 1964.

[25] M. Gamero-Castaño, "Energy dissipation in electrospray and the geomertic scaling of the transition region of con-jets," *J. Fluid Mech*, vol. 662, pp. 493–513, 2010.

[26] M. Gamero-Castaño, "Retarding potential and induction charge detectors in tandem for measuring the charge and mass of nanodroplets," *Review of Scientific Instruments*, vol. 80, no. 5, p. 053301, 2009.

[27] M. Wilm, "Principles of electrospray ionization," *Molecular & Cellular Proteomics*, vol. 10, no. 7, 2011.

[28] J. N. Smith, R. C. Flagan, and J. L. Beauchamp, "Droplet evaporation and discharge dynamics in electrospray ionization," *The Journal of Physical Chemistry A*, vol. 106, no. 42, pp. 9957–9967, 2002.

[29] L. Rayleigh, "Xx. on the equilibrium of liquid conducting masses charged with electricity," *Philosophical Magazine Series 5*, vol. 14, no. 87, pp. 184–186, 1882.

[30] J. S. Shrimpton, "Dielectric charged drop break-up at sub-rayleigh limit conditions," *IEEE Transactions on Dielectrics and Electrical Insulation*, vol. 12, pp. 573–578, June 2005.

[31] M. Gamero-Castaño and M. Mahadevan, "Sputtering yields of si, sic, and b4c under nanodroplet bombardment at normal incidence," *Journal of Applied Physics*, vol. 106, no. 5, p. 054305, 2009.

[32] I. Yamada, "Historical milestones and future prospects of cluster ion beam technology," *Applied Surface Science*, vol. 310, pp. 77 – 88, 2014. Selected manuscripts arising from the 18th International Conference on Surface Modification of Materials by Ion Beams (SMMIB-2013).

[33] Z. Insepov, L. Allen, C. Santeufemio, K. Jones, and I. Yamada, "Crater formation and sputtering by cluster impacts," *Nuclear Instruments and Methods in Physics Research Section B: Beam Interactions with Materials and Atoms*, vol. 206, pp. 846 – 850, 2003. 13th International Conference on Ion Beam Modification of Materials.

[34] T. Aoki, "Molecular dynamics simulations of cluster impacts on solid targets: implantation, surface modification, and sputtering," *Journal of Computational Electronics*, vol. 13, no. 1, pp. 108–121, 2014.

[35] L. Romano, K. S. Jones, K. Sekar, and W. A. Krull, "Amorphization of si using cluster ions," *Journal of Vacuum Science & Technology B: Microelectronics and Nanometer Structures Processing, Measurement, and Phenomena*, vol. 27, no. 2, pp. 597–600, 2009.

[36] L. Pelaz, L. A. Marqus, and J. Barbolla, "Ion-beam-induced amorphization and recrystallization in silicon," *Journal of Applied Physics*, vol. 96, no. 11, pp. 5947–5976, 2004.

[37] T. Seki, T. Murase, and J. Matsuo, "Cluster size dependence of sputtering yield by cluster ion beam irradiation," *Nuclear Instruments and Methods in Physics Research Section B: Beam Interactions with Materials and Atoms*, vol. 242, no. 12, pp. 179 – 181, 2006. Ion Beam Modification of MaterialsProceedings of the 14th International Conference on Ion Beam Modification of Materials14th International Conference on Ion Beam Modification of Materials.

[38] B. Thijsse, T. Klaver, and E. Haddeman, "Molecular dynamics simulation of silicon sputtering: sensitivity to the choice of potential," *Applied Surface Science*, vol. 231232, pp. 29 – 38, 2004. Proceedings of the Fourteenth International Conference on Secondary {IOn} Mass Spectrometry and Related Topics.

[39] J. Kozole and N. Winograd, "Controlling energy deposition during the c60+ bombardment of silicon: The effect of incident angle geometry," *Applied Surface Science*, vol. 255, no. 4, pp. 886 – 889, 2008. Proceedings of the Sixteenth International Conference on Secondary Ion Mass Spectrometry, {SIMS} {XVI}.

[40] J. Walsh, G. Stradling, G. Idzorek, B. Shafer, WX-DO, and H. C. Jr., "Microparticle impacts at ultra-high velocities: Their relation to macroparticle impacts," *International Journal of Impact Engineering*, vol. 14, no. 14, pp. 775 – 784, 1993.

[41] M. Gamero-Castaño and J. F. de la Morandez de la Mora, "Mechanisms of electrospray ionization of singly and multiply charged salt clusters," *Analytica Chimica Acta*, vol. 406, no. 1, pp. 67 – 91, 2000.

[42] M. Gamero-Castaño, I. A. de Carcer, L. de Juan, and J. F. de la Mora, "On the current emitted by taylor cone-jets of electrolytes in vacuo: Implications for liquid metal ion sources," *Journal of Applied Physics*, vol. 83, no. 5, pp. 2428–2434, 1998.

[43] M. Gamero-Castaño and V. Hruby, "Electric measurements of charged sprays emitted by cone-jets," *Journal of Fluid Mechanics,*, vol. 459, p. 245276, 2002.

[44] M. Gamero-Castaño, "The structure of electrospray beams in vacuum," *Journal of Fluid Mechanics*, vol. 604, pp. 339–368, 006 2008.

[45] M. Gamero-Castaño, "Energy dissipation in electrosprays and the geometric scaling of the transition region of cone-jets," *Journal of Fluid Mechanics*, vol. 662, pp. 493–513, 11 2010.

[46] J. F. Mahoney, "Microclustersurface interactions: a new method for surface cleaning," *International Journal of Mass Spectrometry and Ion Processes*, vol. 174, no. 13, pp. 253 – 265, 1998. Polyatomic Ion-Surface Interactions.

[47] J. F. Mahoney, J. Perel, S. A. Ruatta, P. A. Martino, S. Husain, K. Cook, and T. D. Lee, "Massive cluster impact mass spectrometry: A new desorption method for the analysis of large biomolecules," *Rapid Communications in Mass Spectrometry*, vol. 5, no. 10, pp. 441–445, 1991.

[48] Y. Sakai, Y. Iijima, K. Mori, and K. Hiraoka, "Molecular-level etching by electrospray droplet impact," *Surface and Interface Analysis*, vol. 40, no. 13, pp. 1716–1718, 2008.

[49] Y. Sakai, Y. Iijima, K. Mori, and K. Hiraoka, "Extremely smooth surface etching by giant cluster ion impact," *Journal of Surface Analysis*, vol. 4, no. 4, pp. 466–468, 2008.

[50] R. Takaishi, Y. Sakai, K. Hiraoka, H. Wada, S. Morita, T. Nakashima, and H. Nonami, "Electrospray droplet impact secondary ion mass spectrometry using a vacuum electrospray source," *Rapid Commun Mass Spectrom*, vol. 29, pp. 1420–6, Aug 2015.

[51] K. Mori, D. Asakawa, J. Sunner, and K. Hiraoka, "Electrospray droplet impact/secondary ion mass spectrometry: cluster ion formation," *Rapid Communications in Mass Spectrometry*, vol. 20, no. 17, 2006.

[52] F. Saiz and M. Gamero-Castao, "Atomistic modeling of the sputtering of silicon by electrosprayed nanodroplets," *Journal of Applied Physics*, vol. 116, no. 5, p. 054303, 2014.

[53] R. Borrajo-Pelaez, F. Saiz, and M. Gamero-Castao, "The effect of the molecular mass on the sputtering of si, sic, ge, and gaas by electrosprayed nanodroplets at impact velocities up to 17km/s," *Aerosol Science and Technology*, vol. 49, no. 4, pp. 256–266, 2015.

[54] M. Gamero-Castaño, A. Torrents, R. Borrajo-Pelaez, and J.-G. Zheng, "Amorphization of hard crystalline materials by electrosprayed nanodroplet impact," *Journal of Applied Physics*, vol. 116, no. 17, p. 174309, 2014.

[55] F. Saiz, R. Borrajo-Pelaez, and M. Gamero-Castaño, "The influence of the projectile's velocity and diameter on the amorphization of silicon by electrosprayed nanodroplets," *Journal of Applied Physics*, vol. 114, no. 3, p. 034304, 2013.

[56] R. L. Seliger and W. P. Fleming, "Focused ion beams in microfabrication," *Journal of Applied Physics*, vol. 45, no. 3, pp. 1416–1422, 1974.

[57] R. L. Seliger, J. W. Ward, V. Wang, and R. L. Kubena, "A high-intensity scanning ion probe with submicrometer spot size," *Applied Physics Letters*, vol. 34, no. 5, pp. 310–312, 1979.

[58] J. Orloff and P. Sudraud, "Design of a 100 kv, high resolution focused ion beam column with a liquid metal ion source," *Microelectronic Engineering*, vol. 3, no. 1, pp. 161 – 164, 1985.

[59] J. Orloff, L. Swanson, and M. Utlaut, *High Resolution Focused Ion Beams: FIB and its Applications*. Kluwer Academics/Plenum Publishers, New York, 2002.

[60] M. Sugiyama and G. Sigesato, "A review of focused ion beam technology and its applications in transmission electron microscopy," *Journal of Electron Microscopy*, vol. 53, no. 5, p. 527536, 2004.

[61] J. Melngailis, "Focused ion beam technology and applications," *Journal of Vacuum Science & Technology B: Microelectronics Processing and Phenomena*, vol. 5, no. 2, pp. 469–495, 1987.

[62] I. Yamada and N. Toyoda, "Summary of recent research on gas cluster ion beam process technology," *Nuclear Instruments and Methods in Physics Research Section B: Beam Interactions with Materials and Atoms*, vol. 232, no. 14, pp. 195 – 199, 2005. Inelastic Ion-Surface CollisionsProceedings of the 15th International Workshop on Inelastic Ion-Surface Collisions (IISC-15)15th International Workshop on Inelastic Ion-Surface Collisions.

[63] J. Fox, R. Saini, K. Tsui, and G. Verbeck, "Microelectromechanical system assembled ion optics: An advance to miniaturization and assembly of electron and ion optics," *Review of Scientific Instruments*, vol. 80, no. 9, p. 093302, 2009.

[64] R. Saini, Z. Jandric, K. Tsui, T. Udeshi, and D. Tuggle, "Assembled microelectromechanical-systems microcolumn from a single layer silicon process," *Journal of Vacuum Science & Technology B: Microelectronics and Nanometer Structures Processing, Measurement, and Phenomena*, vol. 22, no. 6, pp. 3168–3173, 2004.

[65] T. Tsumagari, H. Ohiwa, and T. Noda, "Design of a low-aberration lens for focused ion beams," *Journal of Vacuum Science & Technology B: Microelectronics Processing and Phenomena*, vol. 6, no. 3, pp. 949–952, 1988.

[66] H. H. Rose, "Historical aspects of aberration correction," *J Electron Microsc*, vol. 58, no. 3, pp. 77–85, 2009.

[67] J. Gierak, C. Vieu, M. Schneider, H. Launois, G. B. Assayag, and A. Septier, "Optimization of experimental operating parameters for very high resolution focused ion beam applications," *Journal of Vacuum Science & Technology B: Microelectronics and Nanometer Structures Processing, Measurement, and Phenomena*, vol. 15, no. 6, pp. 2373–2378, 1997.

[68] M. Szilagyi, *Electron and Ion Optics*. Microdevices Physics and Fabrication Technologies, Plenum Press, New York, 1988. ESBN: 978-1-4612-8247-1 Springer US 978-1-4613-0923-9.

[69] H. H. Rose, *Geometrical Charged-Particle Optics*, vol. 142 of *Springer Series in Optical Sciences*. Springer Berlin Heidelberg, 2009.

[70] J. N. H. Brunt and F. H. Read, "Aberrations in electrostatic lenses," *Journal of Physics E: Scientific Instruments*, vol. 8, no. 12, p. 1015, 1975.

[71] A. Renau and D. W. O. Heddle, "Geometric aberrations in electrostatic lenses: I. a simple and accurate computer model," *Journal of Physics E: Scientific Instruments*, vol. 19, no. 4, p. 284, 1986.

[72] A. Renau and D. W. O. Heddle, "Geometric aberrations in electrostatic lenses: Ii. aberration coefficients and their interrelations," *Journal of Physics E: Scientific Instruments*, vol. 19, no. 4, p. 288, 1986.

[73] O. Sise, D. J. Manura, and M. Dogan, "Exploring focal and aberration properties of electrostatic lenses through computer simulation," *European Journal of Physics*, vol. 29, no. 6, p. 1165, 2008.

[74] O. Sise, M. Ulu, and M. Dogan, "Aberration coefficients of multi-element cylindrical electrostatic lens systems for charged particle beam applications," *Nuclear Instruments and Methods in Physics Research Section A: Accelerators, Spectrometers, Detectors and Associated Equipment*, vol. 573, no. 3, pp. 329 – 339, 2007.

[75] D. Heddle, *Electrostatic Lens Systems*. IOP Publishing Ltd, 2000.

[76] e. a. V. K. ZWORYKIN, *Electron Optics and the Electron Microscope*. John, 1945.

[77] J. Kelly, "Recent advances in electron beam addressed memories," vol. 43 of *Advances in Electronics and Electron Physics*, pp. 43 – 138, Academic Press, 1977.

[78] M. Szilagyi and H. Cho, "Synthesis of electrostatic focusing and deflection systems," *Journal of Vacuum Science & Technology B: Microelectronics and Nanometer Structures Processing, Measurement, and Phenomena*, vol. 15, no. 6, pp. 1971–1982, 1997.

[79] E. V. Asadollahei and M. Gamero-Castaño, "Plasma activated bonding for an enhanced alignment electrostatic lens," *International Symposium on Microelectronics*, vol. 2016, no. 1, pp. 000075–000078, 2016.

[80] U. Gösele and Q.-Y. Tong, "Semiconductor wafer bonding," *Annu. Rev. Mater. Sci.*, vol. 28, pp. 215–241, 1998.

[81] F. Niklaus, G. Stemme, J. Q. Lu, and R. J. Gutmann, "Adhesive wafer bonding," *Journal of Applied Physics*, vol. 99, no. 3, 2006.

[82] "www.wikipedia.org,"

[83] M. Wiemer, D. Wuensch, J. Braeuer, and T. Gessner, *Plasma-Activated Bonding*, pp. 101–118. 2012.

[84] C. Iliescu, J. Jing, F. E. Tay, J. Miao, and T. Sun, "Characterization of masking layers for deep wet etching of glass in an improved hf/hcl solution," *Surface and Coatings Technology*, vol. 198, no. 13, pp. 314 – 318, 2005.

[85] M. Gamero-Castaño, "Characterization of the electrosprays of 1-ethyl-3-methylimidazolium bis(trifluoromethylsulfonyl) imide in vacuum," *Physics of Fluids*, vol. 20, no. 3, p. 032103, 2008.